Master's thesis

NTNU
Norwegian University of Science and Technology
Faculty of Information Technology and Electrical Engineering
Department of Engineering Cybernetics

Vebjørn Wøllo

Voltage Support in Distribution Grids by Model Predictive Control of the Grid Interface Converter for a Battery Energy Storage System

Master's thesis in Cybernetics and Robotics
Supervisor: Jon Are Wold Suul
Co-supervisor: Jonatan Ralf Axel Klemets
June 2023

NTNU
Norwegian University of
Science and Technology

Vebjørn Wøllo

Voltage Support in Distribution Grids by Model Predictive Control of the Grid Interface Converter for a Battery Energy Storage System

Master's thesis in Cybernetics and Robotics
Supervisor: Jon Are Wold Suul
Co-supervisor: Jonatan Ralf Axel Klemets
June 2023

Norwegian University of Science and Technology
Faculty of Information Technology and Electrical Engineering
Department of Engineering Cybernetics

NTNU
Norwegian University of
Science and Technology

Preface

This thesis marks the culmination of my master's degree in Cybernetics and Robotics at the Norwegian University of Science and Technology (NTNU). It is the result of the course *TTK4900 - Engineering Cybernetics, Master's Thesis*, completed during the spring semester of 2023 at the Department of Engineering Cybernetics.

I would like to express my sincere gratitude to Professor Jon Are Wold Suul for his invaluable guidance. His expertise and insightful discussions have significantly broadened my understanding of the field. I am equally grateful to Jonatan Ralf Axel Klemets at SINTEF Energy for his valuable guidance and insights, both during the master's thesis and my research stint at SINTEF Energy in the summer of 2022.

Abstract

The electrification and increased penetration of distributed energy resources in today's society have created an increased demand for the electrical grid. This demand can result in challenges related to grid stability, power quality and continuity of supply. Traditionally, challenges related to increased grid demands have been alleviated through costly and time-consuming methods like grid reinforcements. With the advancement in battery technology, battery energy storage systems have become a viable alternative to grid reinforcements. Battery systems can be installed in locations where the power quality is compromised, thereby providing necessary support. Their flexibility makes them ideal for a wide range of voltage support applications.

This thesis focuses on the supervisory control of a battery system. The power flow between the grid and the battery is controlled by a grid-connected 2-level voltage source converter. A grid-connected voltage source converter is modelled using state-space representation. The voltage source topology used is decoupled current control to independently control the active and reactive power flow between the voltage source converter and the distribution grid.

A model predictive control methodology is proposed as the control strategy for the voltage source converter. Model predictive control has the advantage that it can calculate the optimal active and reactive power injection to the grid, given the constraints on the system. The proposed objectives include voltage tracking, energy optimization and combined voltage tracking with energy optimization. For all objectives, a fast controller with a short time step and a slower controller with a long time step is also proposed.

Simulations of the voltage source converter with the proposed objectives are conducted in a low voltage distribution test grid with load demands to introduce voltage disturbances. The test grid consists of a series of line impedances with connected loads that are supplied from a 22 kV/400 V transformer connected to a 22 kV voltage source acting as the high voltage distribution grid.

The simulations show that model predictive control can successfully be implemented to calculate optimal power injection for voltage support. Among the proposed control methods, the combined objective of voltage tracking with energy optimization demonstrates the best performance. The faster controller can quickly respond to voltage disturbances. It does not have the optimal transient response due to linearization away from an equilibrium point. The slower controller does not have a fast response time and is not able to reject disturbances during the initial voltage dip. However, it shows promising steady-state results. The findings underscore the potential of implementing model predictive control in battery energy storage systems for grid stability and voltage support.

Sammendrag

Elektrifiseringen av dagens samfunn og den økte mengden av distribuert energiproduksjon har ført til økt press på strømnettet. Dette presset kan resultere i utfordringer knyttet til nettstabilitet, spenningskvalitet og leveringskvalitet. Historisk så har disse utfordringene blitt løst ved hjelp av dyre og tidkrevende løsninger som nettforsterkninger. Utviklingen av batteriteknologi har gjort at batterisystemer har blitt introdusert som et mulig alternativ til nettforsterkning. Batterisystemer kan bli installert på plasser der spenningskvalitetet er svekket for å bidra med nødvendig støtte. Fleksibiliteteten til batterisystemer gjør dem ideel for et bredt spekter av bruksområder for spenningsstøtte.

Denne masteroppgaven fokuserer på den overordnede styringen for batterisystemet. Effektflyten mellom strømnettet og batteripakken er kontrollert med en 2-nivå spenningskonverter. En nettilkoblet spenningskonverter er modellert på tilstandsromsform. Topologien til spenningskonverteren bruker dekoblet strømkontroll for uavhengig styring av aktiv og reaktiv effekt mellom spenningskonverteren og distribusjonsnettet.

En modellprediktiv kontrollmetode er foreslått som kontrollsystem for spenningskonverteren. Modellprediktiv kontroll har fordelen at den kan kalkulere optimal mengde aktiv og reaktiv effektflyt tilført strømnettet, gitt begrensningene i systemet. De foreslåtte objektene inkludere spenningskontroll, energioptimalisering og kombinert spenningskontroll med energioptimalisering. For alle objektene så har en rask kontroller med kort samplingsintervall og en treg kontroller med langt samplingsintervall blitt foreslått.

Simuleringen av spenningskonverteren med de foreslåtte objektene er gjennomført i et testnett for det lavspente distribusjonsnettet. Laster er introdusert for å tilføre spenningsforstyrrelser i nettet. Testnettet består av en serie av linjeimpedanser med tilkoblede lastnoder som er tilført spenning fra en 22 kV/400 V transformator tilkoblet en 22 kV spenningsilder som opptrer som et høyspent distribusjonsnett.

Simuleringene viser at modellprediktiv kontroll kan bli iverksatt og optimalt regne ut tilført kraftflyt for spenningsstøtte. Kombinert spenningskontroll med energioptimalisering viser den beste ytelsen blant de foreslåtte kontrollmetodene. Den raske kontrolleren klarer å reagere raskt på spenningsforstyrrelser, men har ikke en gunstig transient respons på grunn av linearisering vekk fra et likevektspunkt. Den trege kontrolleren reagerer ikke raskt nok på spenningsforstyrrelser under den initielle spenningsdippen, men viser gode stabilitetsegenskaper. Resultatene viser potensialet til modellprediktiv kontroll av batterisystemer for nettstabilitet og spenningsstøtte.

Table of Contents

List of Tables

List of Figures

Abbreviations

2L-VSC	Two-level Voltage Source Converter
ac	Alternating Current
BaSS	"*Batteri som spenningsstøtte*" - Electrochemical Battery as Voltage Support in the Distribution Grid
BESS	Battery Energy Storage System
CIG	Converter Interfaced Generation
CIGRE	International Council on Large Electric Systems
CSC	Current Source Converter
dc	Direct Current
DER	Distributed Energy Resources
DoD	Depth of Discharge
ESS	Energy Storage System
EV	Electric Vehicle
FoL	"*Forskrift om leveringskvalitet i kraftsystemet*" - Regulation on Supply Quality in the Power System
IEEE	Institute of Electrical and Electronics Engineers
IntegER	"*Integrasjon av energilager i distribusjonsnettet*" - Integration of Energy Storage in the Distribution Grid
LC	Inductance and Capacitor
MIMO	Multiple-input, Multiple-output
MMC	Modular Multilevel Converter
MPC	Model Predictive Control
NPC	Three-level Neutral Point Clamped Converter
NTI	Nonlinear Time-invariant
NVE	Norges Vassdrags- og Energidirektorat - The Norwegian Water Resources and Energy Directorate
PCS	Power Conversion System
PI	Proportional–integral
PLL	Phase Locked Loop

POI	Point of Interconnection
pu	Per-unit
PV	Photovoltaic
QP	Quadratic Program
RES	Renewable Energy Source
rms	Root Mean Square
SCR	Short Circuit Ratio
SCS	Supervisory Control System
SoC	State of Charge
SoH	State of Health
STATCOM	Static Synchronous Compensator
VA	Volt-ampere
VSC	Voltage Source Converter
X/R ratio	Reactance–resistance Ratio

Nomenclature

Model Parameters

l_f	Inductance for LC-filter
$\omega_{lp,pll}$	Low-pass filter cutoff frequency for PLL
k_{ad}	Gain for active damping
ω_{ad}	Low-pass filter cutoff frequency for active damping
ω_b	Base for grid frequency
$\omega_{lp,m}$	Low-pass filter cutoff frequency for output measurements
r_f	Resistance for LC-filter
c_f	Capacitance for LC-filter
l_g	Inductance of grid impedance
r_g	Resistance of grid impedance
$k_{p,c}$	Proportional gain for current-controllers
$k_{i,c}$	Integral gain for current-controllers
$k_{p,pll}$	Proportional gain for PLL-controller
$k_{i,pll}$	Integral gain for PLL-controller

Input variables

$i^*_{cv,d}$	Reference for converter current, d-axis
$i^*_{cv,q}$	Reference for converter current, q-axis
$\hat{v}_g$	Disturbance, grid voltage amplitude
ω_g	Disturbance, grid frequency

State variables

$v_{o,d}$	Voltage for grid-side of LC-filter, d-axis
φ_q	Low-pass filter state for active damping, q-axis
$v_{pll,d}$	Low-pass filter state for PLL-controller, d-axis
$v_{pll,q}$	Low-pass filter state for PLL-controller, q-axis
ϵ_{pll}	Integrator state for PLL-controller
$\delta\theta_{pll}$	Phase angle between PLL-controller and grid
$p_{o,f}$	Low-pass filter state for active power output
$q_{o,f}$	Low-pass filter state for reactive power output
$\hat{v}_{o,f}$	Low-pass filter state for voltage amplitude
$\hat{i}_{cv,f}$	Low-pass filter state for current amplitude
$v_{o,q}$	Voltage for grid-side of LC-filter, q-axis
$i_{cv,d}$	Current for converter-side of LC-filter, d-axis
$i_{cv,q}$	Current for converter-side of LC-filter, q-axis
γ_d	Integrator state for current-controllers, d-axis
γ_q	Integrator state for current-controllers, q-axis
$i_{o,d}$	Current for grid-side of LC-filter, d-axis
$i_{o,q}$	Current for grid-side of LC-filter, q-axis
φ_d	Low-pass filter state for active damping, d-axis

1

Introduction

This chapter introduces the background and motivation of the master thesis. It presents the challenges related to electrification in the grid and possible solutions using battery energy storage systems (BESSs). A short introduction of relevant projects with BESSs are presented, and the case description for the thesis is presented. The outline and scope of the thesis are presented at the end.

1.1 Background

There is a worldwide trend of transitioning away from traditional energy sources like fossil fuels towards renewable energy sources (RESs). These include wind and photovoltaic (PV) energy sources. This trend is driven by the goal of decreasing the reliance on environmentally damaging fossil fuels and increasing the share of renewable energy production. This shift has gained momentum due to the economic viability of renewables, which makes them more competitive against traditional energy sources. This increased focus on renewables can be seen in the ambitious goal the European Union have set for themselves. They aim for renewable energy to constitute 32% of the gross final energy consumption by 2030, significantly increasing it from the 22.2% achieved in 2021[1]. However, while RESs offer many advantages, they also present unique challenges that can make them difficult to implement. Due to the inherent intermittent nature of wind and PV power, energy production fluctuates throughout the day based on the weather conditions and time. This characteristic creates challenges related to maintaining a steady power supply and balancing critical parameters such as voltage, frequency and power in the electrical grid. In addition to this, RESs can typically be situated closer to the consumer in the distribution grid than traditional energy sources. This together with local production from distributed energy resources (DER) such as household PV or new applications such as Vehicle-to-grid[2] are demanding for the grid. Energy production closer to the consumer creates larger variations in the voltage levels and is more demanding for the grid than traditional energy sources.

The power quality in the grid is influenced by several factors. Two of these are the energy generation location and the increased electrification of various sectors connected to the distribution grid. One particular sector where electrification has seen rapid growth is the transportation sector, where 79% of new cars sold in Norway were electric vehicles (EVs) in 2022[3]. The rapid growth of EVs creates high power demand from the grid during charging periods. This increased load causes strain on the electrical grid, potentially leading to overloads if the grid is not adequately designed to meet the new energy demands[4].

1.1.1 Motivation

Historically, the most common methods of alleviating an increasing grid demand have been to employ passive techniques like grid reinforcement and grid expansion. This can be done in sections of the grid that are underdimensioned. These methods typically involve replacing overloaded distribution transformers, upgrading existing cables or laying additional cables to improve the total cross-section of the cable. By increasing the cross-section, the total impedance of the grid is decreased, reducing the voltage drop in the power lines[5].

Methods based on Static synchronous Compensators (STATCOMs) have also been used extensively for voltage support in the electrical grid. These are fast-acting devices that can regulate the voltage by injecting or absorbing reactive current in the grid[6]. The technology is based on either a current source converter (CSC) or a voltage source converter (VSC), where the latter is most used[7]. By integrating a energy storage system (ESS) into a STATCOM, the system can also provide active power. This system is generally referred to as E-STATCOM. It has shown promising results in smoothing out voltage fluctuations due to variations in energy production PV plants[8].

With the advancement in battery technology, active methods involving grid connected BESSs are becoming more relevant[9, 10]. A BESS can be utilized to alleviate many grid challenges, with different control strategies implemented to achieve this. The challenge is implementing a control strategy for the converter connected to the battery to optimally achieve the objective.

Published research into BESS has grown substantially in the last decade, with power, frequency and voltage support being the main research topics[9]. This growth in published literature and options in converter topologies employed to control the BESS have caused a lack of standardized solutions[11]. Larger literature reviews have been conducted to try to summarize applications, integration strategies and converter topologies[9, 10, 11].

1.1.2 Relevant BESS Projects

Most implementations of BESS in the distribution grid have focused on the integration of BESS with intermittent renewable energy production[12][13]. The goal of these are to balance out the power injected into the grid from the energy source, facilitating a more balanced energy supply. There has been less focus on using batteries solely for mitigating the power quality challenges associated with the broader electrification of the grid. Two

relevant Norwegian projects researching and testing the economic and technical viability of using a BESS as an alternative to grid reinforcements are being researched. The first, "*Integrasjon av energilager i distribusjonsnettet*" - Integration of energy storage in the distribution grid (IntegER) has already been conducted[14]. The second, "*Batteri som spenningsstøtte*" - Electrochemical battery as voltage support in the distribution grid (BaSS) is an ongoing research project by SINTEF Energy[15].

IntegER

The IntegER project conducted by Tensio TN in Sparbu was a pilot project financed by ENERGIX under The Research Council of Norway[14]. It studied a specific case of a consumer connected to a weak grid, characterised by a low short circuit ratios (SCRs). The consumer had challenging load changes and intermittent solar energy production. The combination of these created fluctuating voltage levels and violations of the regulations set by "*Forskrift om leveringskvalitet i kraftsystemet*" - Regulation on supply quality in the power system (FoL). In the project, a BESS was installed close to the consumer as an alternative to grid reinforcement. IntegER conducted tests using the BESS for both phase balancing and peak shaving to improve the power quality. Figure 1.1[14] illustrates how the end consumer was connected to the BESS. The energy capacity and power of the battery were 18 kWh and 15 kW respectively. Based on the results, IntegER showed that the BESS was effective in using phase balancing to mitigate asymmetric grid challenges. It achieved limited results when used for peak shaving. This was due to the battery discharging during high load periods, and consequently not being able to supply power to the grid. There was also a socioeconomic analysis which concluded that a battery system can be an economically viable solution if it results in allowing grid upgrades to be delayed[14].

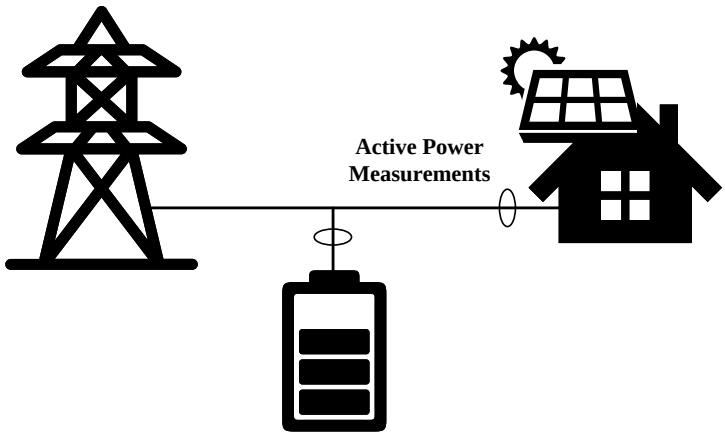

Figure 1.1: One-line diagram of IntegER setup with the consumer. Adapted from[14]

BaSS

BaSS is an ongoing innovation project conducted at SINTEF Energy from 2021 to 2024[15]. It has several project partners and is financed by ENERGIX. The project's objective is to facilitate using battery systems as an alternative to conventional grid reinforcements for voltage problems in the distribution grid. It aims to do this by finding where employing BESSs is the most socio-economical solution and determining what technical solutions must be implemented for it to be viable. BaSS is organized into four main work packages, each exploring different aspects of the implementation of such battery systems[15][16]:

- **Battery as a grid service:** Understanding the conditions needed for a battery system to be used as voltage support. Where will it provide substantial value, and where its use cases will it have limited value.
- **Control strategies:** Development and verification of control algorithms that can be implemented for voltage support. What type of communication and measurements are needed to effectively control the system.
- **Testing and simulation:** The proposed control algorithms will be tested and verified in a Smartgrid-lab[17] for verification. Allowing the algorithms to be tested under controlled situations.
- **Methodology of assessment:** Create a systematic methodology for evaluating a battery system against traditional grid reinforcement. Such that the system can be implemented efficiently where viable.

1.2 Case Description

A grid-connected BESS is connected to the distribution grid at the point of interconnection (POI) as shown in figure 1.2. The function of the BESS is to act as voltage support for the distribution grid due to a change in load demand. This is done by the power conversion system (PCS) which controls the power injection from the BESS into the grid. The PCS of the BESS consist of a VSC connecting the alternating current (ac)-side of the grid to the direct current (dc)-side of a battery pack. All system and grid parameters are listed in appendix A.4. The high voltage ac distribution grid is a 22 kV voltage source with varying SCR depending on grid strength. The transformer transforms the voltage down to 400 V in the low-voltage distribution grid. Transmission lines and load demands in the grid create voltage drops away from the transformer. The 22 kW VSC is connected at the end of the transmission line, with a battery pack as energy storage.

1.2.1 Scope of Work

The scope of this thesis can be split into four main objectives

- Identify voltage quality challenges: Many different power quality challenges can be found in the grid. The scope of this thesis is long-term and short-term voltage variations in the grid due to sudden load changes.

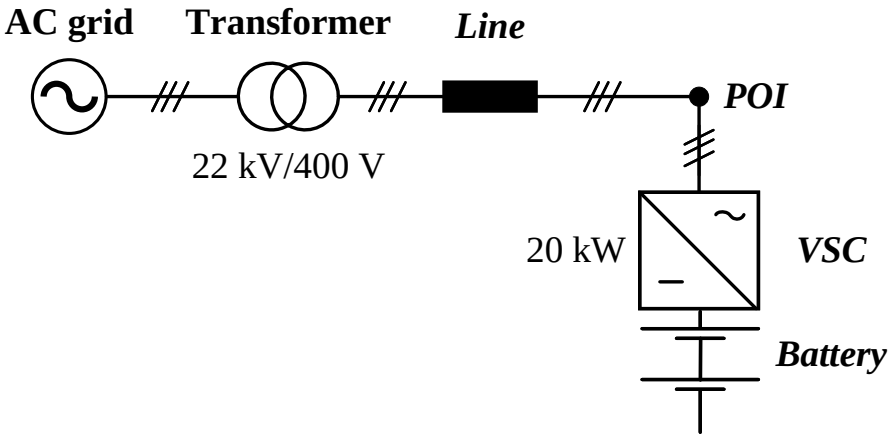

Figure 1.2: System setup and ratings.

- Design and model the VSC in the BESS: This part involves modelling a grid-connected VSC connected to a battery source. The model is represented in a state space representation. This model is then used to control the VSC by the control system.
- Control system and simulation: Implementing a control system to alleviate the power quality challenges found in objective 1. Simulate the grid-connected BESS to investigate how different control strategies and grid parameters affect the performance of the system.
- Investigate the grid parameters: Investigate the influence grid parameters have on the optimal active and reactive power injection within the VSC's current and power limitations. Investigate how penalty weights on active and reactive power injection in the controller affect the performance.

1.2.2 Thesis Outline

The thesis is divided into 7 chapters.

- Chapter 1: Introduction
- Chapter 2: Background Theory
- Chapter 3: Method and Modelling
- Chapter 4: Verification of Model
- Chapter 5: Control Strategy
- Chapter 6: Simulation and Results

- Chapter 7: Discussion
- Chapter 8: Conclusion and Future Work

Chapter 1 presents an introduction to the thesis, as well as an explanation of challenges associated with grid-connected RES. Common methods of mitigating these challenges are presented. Chapter 2 presents background on the Norwegian electrical grid and the regulations associated with it. The characteristics of grid strength are given and its impact on voltage stability. An explanation of an ESS is presented, and the different technologies that are used. The BESS is explained, what types of control methods it utilizes and the converter technology connected to it. Chapter 3 introduces the method used in modelling the VSC. An explanation of the electrical three-phase system used is found here. The modelling of the VSC is explained, with the necessary differential equations. The method used for linearizing the model is explained and the necessary calculations for it. In chapter 4 the nonlinear model's accuracy is verified against the Simulink model. As well as the linear model's accuracy against the nonlinear model. Chapter 5 proposes a control strategy utilizing an model predictive control (MPC). The objective of the controller is formulated, and constraints of the system presented. Chapter 6 presents three different use cases for the BESS, focusing on voltage support. The results using the proposed controller are presented and briefly explained. In chapter 7, the results in chapter 6 are discussed based on the grid aspects defined in chapter 2 and the proposed control strategy from chapter 5. In the last chapter, chapter 8 the conclusion to the thesis is given, with suggestions for future work that can be researched based on the findings. The chapters are briefly summarized in the introduction of each chapter. This gives the reader a quick overview of the content presented.

1.2.3 Implementation and Tools

- MATLAB: Scripts to implement differential equations and linearization of nonlinear equations. Scripts to implement the MPC. Scripts for grid and controller parameters. Figures of the results were plotted in MATLAB.
- Simulink: Implementation of the nonlinear VSC and grid model. Simulations of MPC using the linear models.
- Microsoft Visio: Illustrations and block diagrams.

2

Background Theory

This chapter presents background theory for electrical grids, energy storage systems (ESSs) and voltage source converters (VSCs). The Norwegian electrical grid is presented, and how grid reinforcements are typically performed. The grid parameters', short circuit ratio (SCR) and reactance–resistance ratio (X/R ratio) are defined. energy storage systems (ESSs) are presented, with a focus on battery energy storage systems (BESSs). Their interface and applications in the electrical grid are explained. Lastly, the converter technology connected to the batteries is explained.

2.1 The Norwegian Electricity Grid

The electricity grid in Norway is a critical infrastructure that ensures a reliable energy supply to households and industries throughout the country. Norway is in a special situation, with the largest ratio of renewable energy production in Europe[18]. 98 % of Norwegian energy production in 2022 was produced by hydro- or wind power[19]. To ensure reliability in power delivery, the Norwegian electrical grid has been connected to the European electrical grid since the 1950s. This ensures that during periods of little wind or rain, Norway can import the necessary energy from the European market. Reversely, during periods of energy surplus, Norway has the opportunity to export energy to the European market[20]. This allows for a more reliable energy supply that is less dependent on local weather conditions and power consumption. The Norwegian electrical grid is separated into different voltage levels with different operational responsibilities. These voltage levels are divided into three grid types that connect the entire grid together. The transmission grid, the regional grid and the distribution grid. Figure 2.1 illustrates them and how they connect to each other.

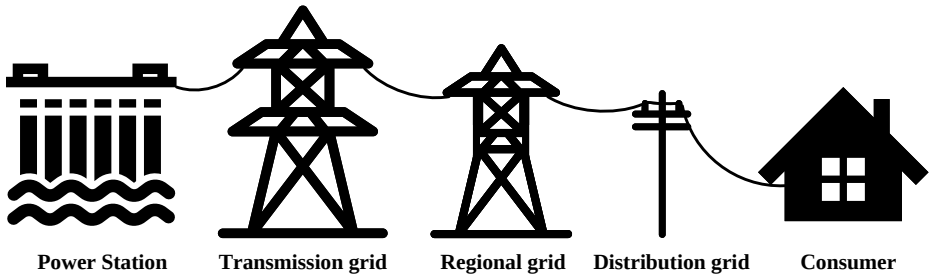

Figure 2.1: Norwegian electricity grid.

2.1.1 The Transmission Grid

The transmission grid is the central grid that links energy producers and consumers together in a nationwide system. The transmission grid is also the grid that connects Norway to the European system. Some energy-intensive consumers, like the petroleum industry, can be directly connected to the transmission grid. The transmission grid carries the highest voltage levels in the electrical grid, operating from 300 kV to 420 kV. It also operates at 132 kV in some parts of the country. The Transmission grid spans approximately 11000 km, and connects the different regions of Norway together[21]. Statnett is the sole transmission system operator in Norway, with ownership of around 94% of the transmission grid. The remaining is owned by various regional grid companies, which are rented and operated by Statnett.

2.1.2 The Regional Grid

The regional grid acts as the link between the transmission grid and distribution grids. It can also include larger production facilities and larger consumers like energy-intensive industries. The regional grid typically operates from 33 to 132 kV and spans 19000 km[21]. Most of the regional grid is owned by municipalities and county municipalities, with some private ownership.

2.1.3 The Distribution Grid

The distribution grid is the grid that most consumers are connected to. Normal households and small-scale industries are connected to the distribution grid. It carries the lowest voltage in the electrical grid, with voltages up to 22 kV. The distribution grid is divided into a high- and low-voltage grid, where the high-voltage segment starts at 1 kV. The low voltage distribution is connected to most consumers with a voltage typically operating at 400V or 230V. The total length of the distribution grid is about 100000 km [21]. Like regional grids, the distribution grid is mainly owned by municipalities and county municipalities, with some private ownership.

2.1.4 Grid Reinforcements

The methodology of grid upgrades and expansion is described in detail in *Planleggingsbok for kraftnett* (*Planbok*) [22], a comprehensive document made by SINTEF Energy and REN. The document details the economic and technical aspects of grid upgrades. A short summation of the necessary steps of grid upgrades are explained here[23]:

According to *Planbok*, there are six steps of analysis for the typical planning process in the distribution grid. Figure 2.2 illustrate these steps[23]. The first step consists of establishing the goals and prerequisites for the analysis. The second step gathers a prognosis of load demands and production. In the third step, different alternatives to obtain the goals set in step one are laid out. Then a technical analysis of these alternatives is done in step four, and whether they are feasible or if any constraints are broken. If the alternative is found infeasible, it is modified and analysed again. In the fifth step, an economic analysis of the chosen alternative is conducted. If the economic analysis is unacceptable, a new alternative is proposed and reevaluated. If the economic analysis is acceptable, an assessment of every aspect is done in step six. If all steps of the proposed alternative meet the criteria set, it is accepted and documented.

2.2 Quality of supply

Quality of supply is the term generally used to describe the quality of electricity that is being supplied to the consumer. The operation and efficacy of electrical equipment are influenced by the quality of the voltage and current that is supplied. Low-quality voltage and current can impact different equipment differently, ranging from negligible effects, to a complete failure of operation. This section reviews issues related to the quality of supply, as defined by Norges vassdrags- og energidirektorat - The Norwegian Water Resources and Energy Directorate (NVE), with a further focus on the issues that are relevant to this thesis. NVE defines quality of supply as these three components[24]

- Customer service
- Continuity of supply
- Power quality

Customer Service

Within the scope of quality of supply, customer service refers to how grid companies deal with consumers and relay information to them. While customer service is an important aspect of the quality of supply, it is not within the scope of this thesis and will not be reviewed further.

Continuity of Supply

Continuity, or reliability, of supply describes the power system's capability of supplying electrical energy to the consumer. Any interruption in the supply will at minimum cause inconvenience for the consumer, and can also lead to life-threatening situations or technical

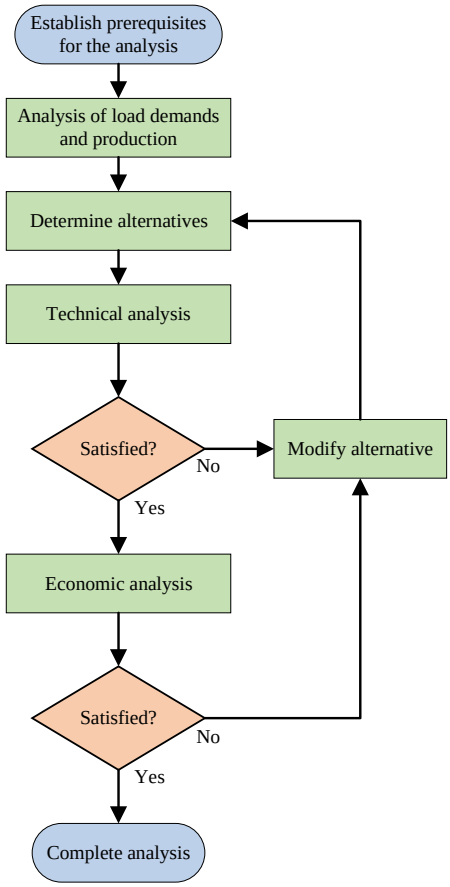

Figure 2.2: Systematic steps during grid reinforcements according to *planbok*. Adapted from[23].

and economic problems for industries dependent on a reliable supply of energy. Ensuring high reliability of supply can be achieved by having different types of energy generating producers, utilizing interconnected grids that can re-route energy around faulty lines, and using high-quality installed components[25]. The continuity of supply is not within the scope of this thesis and is not reviewed further.

Power Quality

Power quality pertains to the quality of the supplied electricity whenever there are no interruptions in the electrical supply. Low-quality power can cause many of the same problems as no power. Electrical equipment may not work as intended, and whole systems may shut down if the quality is low enough[22]. The definition of power quality is not universally agreed upon, and different definitions are found in papers, articles and textbooks. For the purpose of this thesis, power quality is defined as the quality of the voltage and current. This encompasses the measurements, analysis and improvement of the bus voltage to maintain a sinusoidal waveform at the rated voltage and frequency, for both steady-state and momentary values[26]. The concept of current quality will not be reviewed in this thesis, and terms voltage quality and power quality will be used interchangeably. In section 2.2.1 the laws and regulations required for system operators that are relevant to this thesis are described. Power quality regulations that are not relevant to this thesis are listed, but not reviewed further.

2.2.1 Norwegian Laws and Regulations

NVE has developed a set of regulations that govern the quality of electricity supply within the Norwegian power system. These regulations are found in FoL[27]. FoL define various issues related to the quality of supply. Some of the issues have specific requirements, while others do not have concrete requirements. Even if no strict requirement is set, NVE have the mandate to set requirements if the problem causes issues for the consumer or grid companies[24]. Table 2.1 lists the quality of supply issues defined by FoL, if there is a specific requirement set, and whether that specific issue is within the scope of this thesis.

Out of the ten problems defined by FoL, nine of them are power quality related and can be alleviated by installing a BESS. Only two of them fall within the scope of this thesis. These are long-term voltage variations and short-term voltage variations, which are explained below.

Long-term Voltage Variations

Long-term voltage variations are defined by FoL as variations in the stationary voltage root mean square (rms) value, measured over a given time period. The requirement set by FoL is that the stationary value should not deviate more than $\pm 10\%$ of the nominal voltage. This is measured over a one-minute time period at the POI in the low-voltage grid[27]. Significant deviations from the nominal voltage can potentially cause faults, disconnection or failure in electrical equipment. This can occur from both long-term overvoltage and undervoltage. For some equipment, these voltage variations can also severely reduce the lifespan of the electrical equipment.[22].

Category	FoL requirement set	Within scope
Interruptions	No requirement	Not in scope
Voltage frequency	Requirement set	Not in scope
Long-term voltage variations	Requirement set	In scope
Short-term voltage variations	Requirement set	In scope
Flicker intensity	Requirement set	Not in scope
Voltage asymmetry	Requirement set	Not in scope
Overharmonic voltages	Requirement set	Not in scope
Interharmonic voltages	No requirement	Not in scope
Superimposed voltage signal	No requirement	Not in scope
Transient overvoltages	No requirement	Not in scope

Table 2.1: Phenomena defined by FoL

A common scenario that can lead to violations of long-term voltage variations occur in low-voltage radial grids.To ensure that all consumers connected to the grid receive voltages within the boundaries set by FoL, the consumers nearest to the distribution transformer are supplied with a higher voltage than those further away. If the transformer is adjusted incorrectly, the consumers nearest to the transformer can experience excessively high voltages. With the integration of solar-powered energy producers, high voltages can also occur during peak production hours. Both of these situations are especially relevant during periods of low load demands in the grid, such as in the summer. The opposite problem can occur for consumers far away from the transformer during periods of high load demand, such as in the winter on a poorly dimensioned grid[24]. Typical methods of resolving long-term voltage variations have previously been grid reinforcement, correctly tapping transformers and voltage boosters. Recently systems using a BESS have been examined[14] and is the method reviewed in this thesis.

Short-term Voltage Variations

Short-term voltage variations can be categorized into three groups: short-term overvoltages (also known as voltage swells), short-term undervoltages (voltage dips), and voltage surges. All of them have the same requirements, but are defined slightly different. The requirements set by FoL are listed in table 2.2. $\Delta V_{stationary}$ and ΔV_{max} are defined in equations (2.1) and (2.2) and V_N is the nominal voltage of the grid. The requirements set a maximum number of allowed occurrences within a 24-hour time period.

Short-term overvoltage, short-term undervoltage and voltage surges	Maximum number of allowed violations within 24 hour period
	$0.23 \text{ kV} \leq V_N \leq 35 \text{ kV}$
$\Delta V_{stationary} \geq 3\%$	24
$\Delta V_{max \geq 5\%}$	24

Table 2.2: Maximum allowed short-term voltage violations within a 24-hour time period.

Short-term Overvoltages

Short-term overvoltages illustrated in figure 2.3 are defined as a rapid increase in the voltage rms value to higher than 110% of the nominal voltage with a duration of 10 milliseconds to 60 seconds. For electrical installations or equipment that is supplied by more than one supply voltage, voltage swell is recognized if at least one of the supply voltages exceeds 110%.

Voltage swells typically occur during the disconnection of large loads or sections of the grid. Faulty tapped transformers that are disconnected from the grid can also cause swells. Swells can in some cases cause faults and disconnection of electrical equipment. However, in laboratory experiments conducted by SINTEF Energy, electrical equipment has been demonstrated to effectively handle voltage swells[22]. A common method for counteracting swells is quicker automatic tapping of transformers. This does not stop voltage swells, but can help reduce its duration.

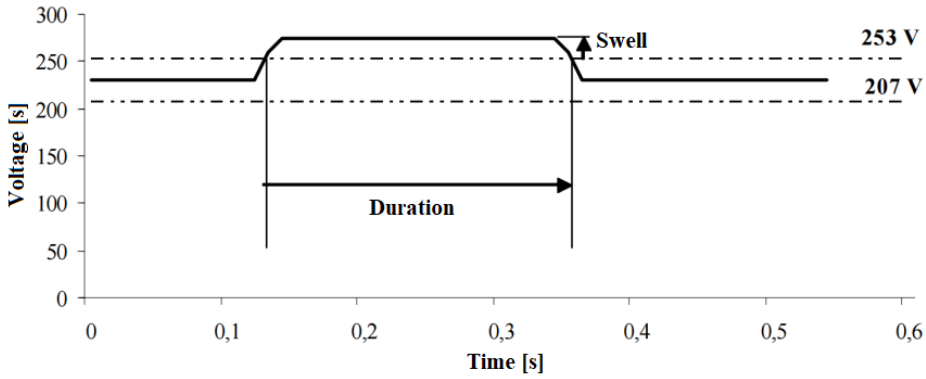

Figure 2.3: Short-term overvoltage. Adapted from[24]

Short-term Undervoltages

Short-term undervoltages illustrated in figure 2.4 are the opposite of overvoltages. They are defined as a rapid drop in the voltage rms value to lower than 90%, but higher than 5% of nominal voltage with a duration of 10 milliseconds to 60 seconds. Similar to volt-

age swells, if there are multiple voltage supplies, and at least one dips below 90%, it is recognized as a voltage dip.

Voltage dips can occur during short-circuits in the grid, re-connection after faults and a sudden increase in the load demands Similar to voltage swells, voltage dips can cause faults and disconnection of electrical equipment. However, voltage dips typically involve larger voltage changes than for swells, and are over 10 times more frequent than voltage swells. This makes it along with interruptions of the supply the largest contributor to economic loss for consumers in Norway[22]. Some common methods for counteracting dips are clearing grid lines for trees to avoid faults, general maintenance and better practices during the re-connection of grids after faults.

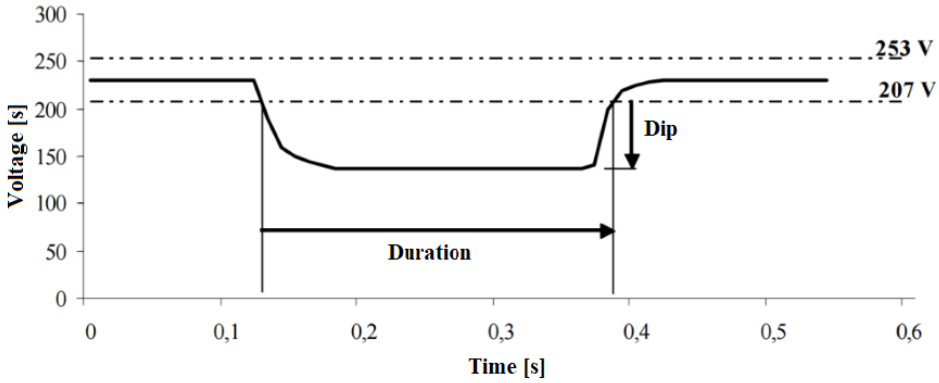

Figure 2.4: Short-term undervoltage. Adapted from[24]

Voltage Surges

Voltage surges illustrated in figure 2.5 are defined as rapid changes in the voltage rms value within 10% of the nominal voltage that occurs faster than 0.5% of nominal voltage per second. Voltage surges are expressed by its stationary and maximum voltage change as defined by FoL as

$$\%V_{stationary} = \frac{\Delta V_{stationary}}{V_N} \cdot 100\% \tag{2.1}$$

$$\%V_{max} = \frac{\Delta V_{max}}{V_N} \cdot 100\% \tag{2.2}$$

where $\Delta V_{stationary}$ is the stationary voltage change due to a change in a voltage characteristic and ΔV_{max} is the maximum voltage differential during a change in the voltage characteristic. A change in the voltage characteristic means the change in the voltage rms value evaluated every half-period. The voltage is considered stable when the rms value is

within 0.5% of the nominal voltage[27]. In comparison with voltage swells and dips, voltage surges are generally less destructive to electrical equipment. They typically only lead to flickering lights, and rarely lead to faults or disconnections. Despite this, it is still one of the most significant causes of consumer complaints in Norway due to the annoyance flickering lights can cause[28]. Some common methods for counteracting voltage surges are improved practices when connecting large loads or using soft starters for motors. Increasing the SCR through grid reinforcements, discussed in section 2.3, helps reduce the impact of connecting large loads. For the consumer, changing light to less sensitive types can also lessen the impact of voltage surges.

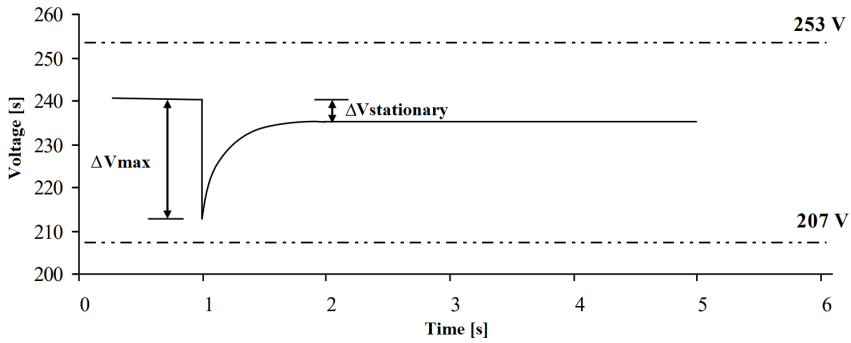

Figure 2.5: Voltage surge. Adapted from[24]

2.3 Grid Strength

Electrical grid strength refers to a system's sensitivity to changes in power flow or current injection from inverter-based resources. A system is considered "strong" if the voltage and angle are relatively insensitive to a change in load, meaning that $\frac{dV}{dP}$ and $\frac{dV}{dQ}$ are small. In a "weak" grid this sensitivity is higher, meaning that $\frac{dV}{dP}$ and $\frac{dV}{dQ}$ are significant.[29].

The strength of an electrical ac system is determined by its impedance and the mechanical inertia of the connected generators. A grid can be classified as weak if either the system impedance is high, or the mechanical inertia is low[30].

Due to the nature of power electronics, the mechanical inertia of a converter will be low. Therefore, the grid characteristics are mainly dependent on the grid impedance, which consists of the impedances in the generators, transformers, transmission lines and loads[31]. It is important to note that the grid's strength is not the same throughout the grid because each location will have different values of impedances and loads. In this thesis, the location referred to will be defined as the POI of the BESS.

The voltage sensitivity of a system is usually classified according to the SCR at the POI. Because weak grids are considered high-impedance grids with volatile voltage stability, the SCR and X/R ratio are central aspects when classifying grid strength[32]. SCR and

X/R ratio are defined below.

2.3.1 Short Circuit Ratio

SCR is the ratio between the short circuit power from the grid to the power capacity of the rating of the converter-based resource connected at the POI[29]. It is defined as

$$SCR = \frac{S_{sc}}{P_{dc}} \tag{2.3}$$

where P_{dc} is the nominal power of the converter and S_{sc} is the short circuit apparent power of the grid at the POI. S_{sc} is defined as

$$S_{sc} = \frac{V_g^2}{Z_{th}} \tag{2.4}$$

where V_g^2 is the voltage at the POI and Z_{th} is the magnitude of the Thevenin equivalent impedance of the grid[30] at the POI. In a per-unit (pu) system, explained in section 3.2, the nominal voltage v_g and nominal converter power p_{dc} are given as 1. This gives the SCR as

$$SCR = \frac{s_{sc}}{p_c} = \frac{v_g^2}{z_{th} p_c} = z_{th}^{-1} \tag{2.5}$$

It is important to note that SCR is an appropriate metric to use when considering systems with a single inverter-based connection. It does not account for grids with multiple power electronic connections close to the POI[29]. There exists other SCR-based metrics that account for this. In Kundur [30] the metric effective short circuit ratio (ESCR) is used. Other metrics used are weighted short circuit ratio (WSCR) or composite short circuit ratio (CSCR)[29]. These are not within the scope of the thesis and will not be reviewed further.

Large differences exist in the SCR given for the classifications of strong and weak grids. Vilmann et al. [32] have summarized literature defining different SCR levels for grid strength. Table 2.3 shows this summary with original sources.

As the SCR only considers the magnitude of, and not the X/R ratio, it does not alone accurately describe the strength of an electrical grid[32]. It is important also to define the X/R ratio of the grid.

2.3.2 X/R Ratio

X/R ratio is the ratio of reactance and resistance of an impedance. The grid X/R ratio is a local parameter describing the X/R ratio at the POI. The grid impedance is defined as

$$Z_g = \frac{V_g^2}{SCR \cdot P_c} \tag{2.6}$$

Source	Very Weak	Weak	Strong
[33]	N.A.	<10	>20
[34]	<3	3< SCR <5	N.A.
[35]	<2	2< SCR <3	>3
[36]	N.A.	<6-10	>20-25
[37]	1	N.A.	N.A.
[38]	N.A.	6	N.A.

Table 2.3: Grid strength classification of SCR levels[32].

where Z_g is equivalent to Z_{th}, as in equation (2.3). The impedance angle θ is defined by the X/R ratio by $\theta = \arctan(X/R)$. The impedance is then given by

$$\begin{aligned} Z_g &= R_g + jX_g \\ R_g &= Z_g \cos\theta \\ X_g &= Z_g \sin\theta \end{aligned} \tag{2.7}$$

where R_g is the grid resistance and X_g is the grid reactance. X/R ratio plays a subtle role in damping in the grid. An X/R ratio of less than 3 is an indication of a weak grid, while values between 1 and 5 indicate low X/R ratio values[32]. It is important to note that a low X/R ratio alone does not result in a weak grid. Both the SCR and X/R ratio should be low[39]. The effect of the X/R ratio on the grid and control method is explained further in section 2.5.2

2.4 Power System Stability

Institute of Electrical and Electronics Engineers (IEEE) and International Council on Large Electric Systems (CIGRE) use the formal definition for power system stability[40]:

> *Power system stability is the ability of an electric power system, for a given initial operating condition, to regain a state of operating equilibrium after being subjected to a physical disturbance, with most system variables bounded so that practically the entire system remains intact.*

Maintaining synchronous operation has traditionally been the main stability problem of a power system. With synchronous machines representing the vast majority of electrical power generation, it has been a necessary condition for stability that these machines stay synchronous. There are however other power system stability aspects that are important, as instability can be experienced without a loss of synchronism. If the voltage across a load collapses, maintaining synchronism is not an issue, but stability and control of voltage are. A system must be able to stabilize itself after disturbances. Small disturbances such as continuous load changes, while still being able to supply the maximum amount of load

possible. The system must also be able to handle severe disturbances such as short circuits of transmission lines, loss of generators or disconnections of whole systems[30].

New technologies and more stressed conditions for power systems have made it necessary for consistent terminology when describing power system stability. With the increased penetration of converter interfaced generations (CIGs) in the grid, new categories of stability have also been added in recent years[41]. Currently there are five categories of power system stability defined by IEEE and CIGRE[40, 41]. These are illustrated in figure 2.6[41] and the list below.

- **Resonance stability:** This refers to the system's ability to dissipate energy during an oscillatory energy exchange adequately. Insufficient energy dissipation can cause the oscillations to grow and manifest in a magnification of the voltage, current and torque magnitudes. Resonance instability occurs when these magnitudes exceed a set threshold.
- **Converter-driven stability:** These are system instabilities associated with power electronic converters. The dynamic behaviour of CIGs is inherently different from synchronous machines, because their behaviour is largely dependent on the implemented control algorithm. The control system typically operates across timescales, which can cause instabilities in a wide range of frequencies. Fast- and slow-converter driven stability issues are often differentiated depending on the frequency of the instability.
- **Rotor angle stability:** This refers to the ability of synchronous machines (like motors and generators) to maintain synchronism during normal operating conditions and after being subjected to a disturbance. If one machine runs slightly faster than the grid, the grid will transfer part of the load to the faster machine and slow it down. During steady-state operation, small disturbances in a machine can self-correct after the disturbance is gone.
- **Voltage stability:** This refers to the ability of a power system to maintain a steady voltage for all buses, both during normal operating conditions and after being subjected to a disturbance. Voltage stability in a power system depends on the ability to maintain equilibrium between load demand and supplied load. Deviations too far away from equilibrium can cause *voltage collapse* in the power system, a situation where the system reaches abnormally low voltages or a complete blackout. Voltage stability is further discussed in section 2.2.
- **Frequency stability:** This refers to the ability of a power system to maintain a steady frequency during normal operation and after a severe disturbance leading to a significant imbalance between generation and load. A power system operates at a steady frequency, and an imbalance in load demand and supplied load will increase or decrease the frequency of the grid. Frequency stability is most commonly a problem during conditions when larger systems have been segmented into smaller islanded systems after a fault. Smaller islanded systems are inherently more prone to frequency instability.

It is important that power system instability does not necessarily occur separately from

each other according to the classification. One form of instability can lead to another one, in a cascading event. These classifications are meant to understand the underlying conditions that create system instability, and how to appropriately design methods that alleviate them[40].

In this thesis, the main classification that is within scope is that of voltage stability. In section 2.2 the requirements set for the voltage levels are given. Voltage levels outside the requirements set do not necessarily result in voltage instability- It is however necessary to maintain voltage stability at all times to avoid system faults. The challenge is to balance the load exchange between the BESS and the grid while maintaining stability. This is a challenge due to the nonlinear characteristics of the power system, where operating parameters and loads constantly change. The stability of the system is a property of the initial conditions as well as the characteristics of the disturbance[40].

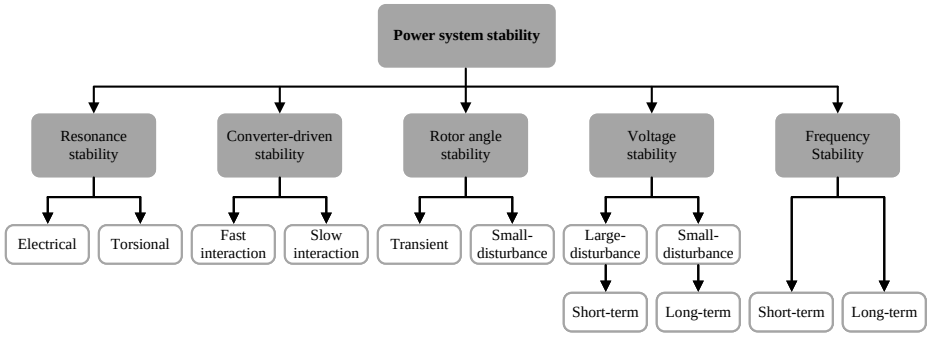

Figure 2.6: Power system stability classification. Adapted from[41].

2.5 Energy Storage System

An ESS is a method of storing energy to be used at a later time. Energy production can vary throughout the day and year. By implementing an ESS, the energy can be stored during peak production periods and discharged during low energy production periods.

The increased shift in recent years to renewable energy sources like PV and wind farms help energy producers meet the demand for more sustainable energy production. The intermittent nature of these energy sources can lead to grid instability. To alleviate these instabilities, an ESS can be implemented to counteract fluctuating energy production. Other instabilities caused by weak electrical grids or the widespread increase of EV that have a large intermittent power consumption can also be alleviated by an ESS. This makes it an essential part of the development of more sustainable energy technologies.

Different ESS technologies exist with different use cases and advantages. These can be categorized as mechanical, electrochemical, electrical, chemical or thermal. Figure 2.7 illustrates the classifications and some of the storage technologies for each. Some of the most used technologies are:

- Pumped storage hydropower (PSH)
- Compressed air energy storage system (CAES)
- Battery energy storage system (BESS)
- Flywheel energy storage system (FESS)
- Superconducting magnetic energy storage system (SMES)
- Super capacitor energy storage system (SCESS)

The application of each system and its characteristics largely depend on the energy density and total power of the system. In table 2.4 a comparison of the different storage technologies is listed[42]. As the table shows, a BESS can be installed with a high energy density and large peak power, while at the same time having a short response time. This makes it a viable solution for a wide range of different energy storage applications.

Technology	Power	Energy density	Response time	Efficiency
PSH	100MW - 2GW	400MWh - 20GWh	12 min	70-80%
CAES	110MW - 290 MW	1.16GWh - 3GWh	12 min	90%
BESS	100W - 100 MW	1kWh - 200MWh	Seconds	60-80%
FESS	5kW - 90MW	5kWh - 200kWh	12 min	80-95%
SMES	170kW - 100MW	110Wh - 27kWh	Milliseconds	95%
SCESS	$\leq$ 1MW	1Wh - 1kWh	Milliseconds	$<$ 95%

Table 2.4: Energy storage technologies and their characteristics[43]

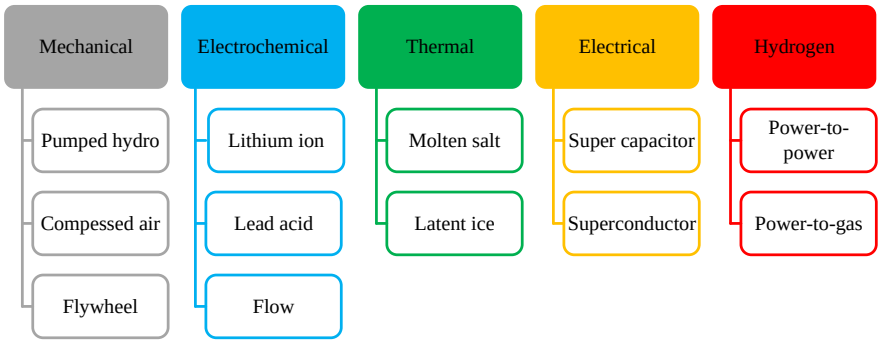

Figure 2.7: Energy storage system technologies and their classifications.

2.5.1 Battery Energy Storage System

Batteries represent one of the most common ESS-technologies, and their application is growing with the improvements made in battery technologies. As illustrated in figure 2.7,

batteries are an electrochemical storage technology. It stores electricity in chemicals and can release it on demand. Numerous different battery technologies exist, with different intended applications and characteristics[44]. All these batteries have definitions that express the batteries' characteristics and current operating conditions. In appendix B.1, descriptions of relevant battery terms mentioned in this thesis are presented.

Components

A BESS consists of several components that work together to create the final system. An illustration of the interaction within the components is shown in figure 2.8. The four main components are[4]:

- **Battery pack:** This is composed of several battery cells that are combined in modules to create a larger battery pack. The size of the battery pack largely determines the energy capacity of the BESS and must be appropriately scaled for the intended application.
- **Battery management system (BMS):** This ensures safe and optimal working conditions for the battery pack by monitoring the status of the battery cells. It regulates the temperature, current flow and voltage levels. These measurements are used to balance battery cells to achieve a balanced state of charge (SoC) for battery cells in series.
- **Supervisory control system (SCS):** This is the top level of the control system. It monitors and controls the BESS to ensure the system's intended application is achieved. The SCS determines the energy flow between the BESS and the electrical grid. Depending on the intended use and complexity of the control algorithm used, different measurements of the grid are necessary for its operation.
- **Power conversion system (PCS):** A four-quadrant ac/dc converter that connects the battery pack to the electrical grid. The response time and power capacity determine the size and technology used. Typically an outer loop controller, like the SCS determines the energy flow between the PCS and the grid, while an inner loop controller is in charge of controlling the PCS to achieve this.

Lithium-ion Battery

Among the various battery technologies, lithium-ion batteries are the most common technology used for large applications such as EVs, maritime vessels and BESSs. Lithium-ion batteries' popularity comes from their high energy density, power capacity, efficiency and long lifetime. Over the past decade, the cost of lithium-ion battery packs has steadily decreased. Despite a slight cost increase in 2022 due to component prices and inflation, BloombergNEF projects the prices to start decreasing again by 2024[46].

While several types of lithium-ion batteries with different advantages and disadvantages exist today, this section focuses on their shared characteristics, and does not look into the specific characteristics of each technology. A lithium-ion battery is typically considered past its lifetime when the state of health (SoH) has reached 80%. The normal lifetime of the

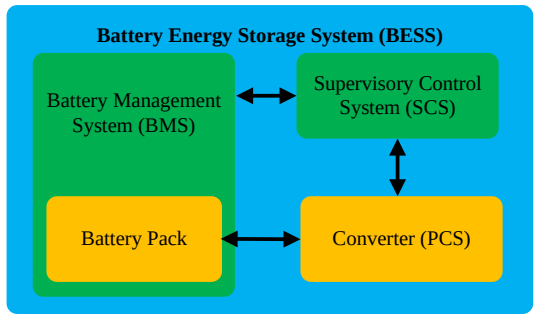

Figure 2.8: Battery energy storage system components and their interaction with each other. Adapted from [45]

battery varies between 5-15 years and 1000-10000 cycles depending on its application[47]. The two main categories for the degradation of batteries are calendar degrading and cyclic degrading:

- **Calendar degrading:** This degradation occurs as the battery ages, even when not in use. Factors such as time, temperature and SoC influence the calendar degradation. By adhering to the manufacturer's specified limits for temperature and SoC, the degradation can be mitigated.
- **Cyclic degrading:** This degradation occurs from using the battery, more specifically when charging and discharging the battery. It is affected by temperature, battery level, depth of discharge (DoD) and the C-rate[48]. Fast charging and deep discharges expedite the cyclic degrading more than slow charging and discharges within the manufacturer's limits.

During the lifetime of the battery, the available energy capacity and power capacity are impacted and get lower throughout the lifetime. Therefore it is important to consider this when calculating the size of the battery for the duration of the intended application[4].

2.5.2 Battery Energy Storage System in the Distribution Grid

A BESS has multiple applications in the distribution grid and can be placed at different locations depending on the applications. Some of the typical applications for a BESS can be[4]:

- Peak shaving: Reduce the strain on the grid due to large load changes.
- Maintain power quality: Keep the voltage within the regulations set by FoL.
- Voltage regulation: Provide support for integrating solar or wind energy that creates fluctuations in the grid due to intermittent energy production.
- Increase short circuit protection: Mitigate low fault currents to ensure the tripping of circuit breakers.

- Black start after fault: Start up a power station or electric grid after a blackout.
- Energy Reserve: Reserve energy supply during blackouts.

Depending on the application and the characteristics of the grid, the sizing of the BESS, including the converter will vary. Further below, the sizing of the battery pack is discussed relating to the grid characteristics explained in section 2.3.2. The battery does not need to be large if only reactive power is needed. If the BESS does not need to supply active power, the battery can be quite small, while the converter must be dimensioned by the total power flowing to the grid. It is also possible to combine many of the use cases to be done by a single BESS to benefit multiple scenarios as well as be more economically viable.

Below, an explanation of peak shaving and power quality mitigation is presented, as these are the most relevant use cases for a BESS in this thesis.

Peak Shaving

Peak shaving is a method of mitigating strain on the grid due to short-term load changes. It works by setting a maximum limit on the allowed power drain on the grid. When the needed load exceeds this limit the BESS will discharge energy to the grid. During low-load periods the BESS will charge up. figure 2.9 illustrates how peak shaving works by charging the batteries during the blue low-load period and discharging the battery during the yellow high-load period. The red line is the load demand that the grid sees. In the IntegER project in section 1.1.2, when the control algorithm was set to peak shaving, their results showed that the battery system was able to mitigate the largest load spikes by 20%. However, it couldn't consistently maintain the desired load limit due to battery discharge. They concluded that a battery that is only used for peak shaving was not recommended compared to grid reinforcements[14].

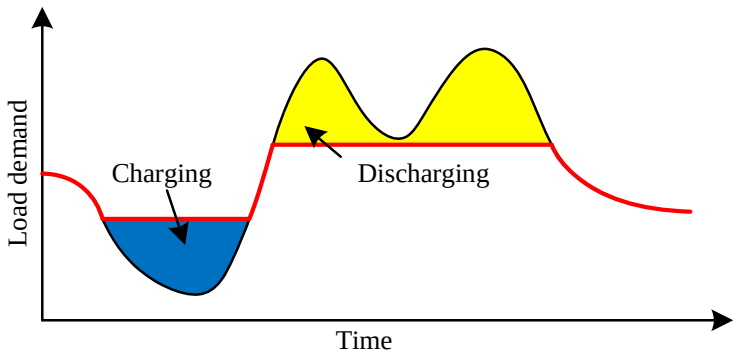

Figure 2.9: Peak shaving

Maintaining Power Quality

In section 2.2 the concept of power quality was explained. A BESS can be used to mitigate these issues. The method used is similar to the peak shaving method. Unlike peak shaving,

the optimal method of using the BESS is not to set a maximum or minimum limit for when the system should inject or absorb energy into the grid. Depending on the characteristics of the grid explained in section 2.3, it may be necessary to inject or absorb active or reactive power to and from the grid. Figure 2.10[16] shows how the BESS is connected to the grid through the line impedance.

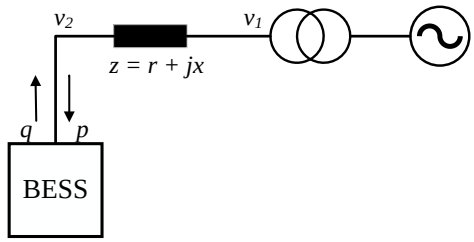

Figure 2.10: One-line diagram of BESS effect on grid voltage

v_1 is the voltage source of the electrical grid and can be assumed constant, while v_2 is the connection point to the BESS. Assuming that the electrical grid is symmetric, the voltage drop over the line can be simplified to[49]

$$\Delta v = v_1 - v_2 \approx \frac{r_{ln}p + x_{ln}q}{v_2} \tag{2.8}$$

Where r_{ln} and x_{ln} are the line resistance and line reactance. It can be seen that a load change will always cause a voltage drop. Depending on the X/R ratio of the grid, active and reactive power will affect the voltage amplitude differently. For longer lines with higher line impedance $z_{ln} = r_{ln} + jx_{ln}$, the voltage drop at the end of the line will be higher for the same amount of load. This means that a BESS can have a higher impact for longer lines where the voltage drop is high because a similar power injection will have a higher impact on the voltage than for a network with shorter lines.

The optimal control algorithm to use will depend on the power quality problem the BESS is being designed for. For long-term voltage variations, the control system does not need to be fast acting, and it can have longer time steps. For short-term voltage variations, it is necessary to use a faster control system that can respond in time.

Grid Interface

Figure 2.11 shows how a BESS can typically be connected to the electrical grid. Individual converters can be connected to each battery pack, as in figure 2.11a, while figure 2.11b shows a setup where the battery packs are connected in parallel to a common dc bus[47]. Multiple battery packs can be connected together to increase the energy capacity of the BESS without having to install a larger VSCs connected to it.

Research into the optimal location of the BESS has been conducted. For phase balancing with a three-phase BESS, it was found that by placing it higher up on the feeder, closer to the substation, while still close enough to the weakest node it had the most positive

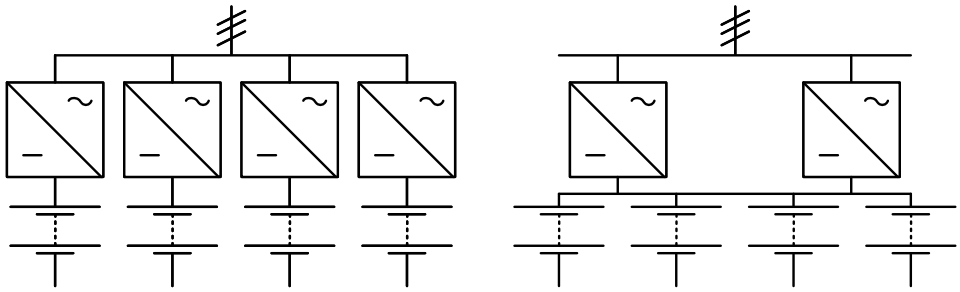

(a) Individual converters **(b)** Common dc-bus

Figure 2.11: Grid interface of the converter. Adapted from[47].

impact[50]. For grids with high distributed generation, different algorithms that provide the optimal location to minimize transmission losses and voltage deviations have been researched[51]. Depending on the application of the BESS and the characteristics of the grid, the optimal location of the BESS can vary. It is therefore necessary to investigate the intended application and system before deciding on a location.

Power Control

A grid-connected VSC with energy storage such as a battery pack can have three different operation strategies. These three are

- **Reactive power control:** A grid-connected VSC without any energy storage attached. This control type is able to inject reactive power into the grid.
- **Active power control:** A grid-connected VSC with energy storage attached. This can be used for applications where active power is needed, such as peak shaving or voltage regulations due to RESs.
- **Combined power control:** A grid-connected VSC with energy storage attached. Advanced control algorithms are needed to calculate the optimal active and reactive power injected into the grid for voltage support. This allows for more applications of the BESS where both active and reactive power is needed.

Ac transmission systems with a high X/R are dominated by reactance. For these systems, the active power transmission is closely associated with the reactive power supply or consumption[52]. Voltage support in grids with a high X/R ratio can be achieved through reactive power control as the line resistance is ignored. Common technologies used for reactive power challenges are capacitor banks, static VAR compensator (SVC), or STATCOM[53]. These can provide fast-acting dynamic reactive power for voltage stability[54]. These technologies are generally more economical, as they do not rely on large energy storage capacity.

In section 3.1.3 it is explained how the VSC can independently control the active and

reactive power injected into the grid. By operating in reactive power control mode, the size of the energy storage can be minimized. This results in a more economic BESS as the cost of the energy storage is higher than the power electronics in many BESS systems[50].

Active power control can be utilized in grids with a low X/R ratio. For these grids, the assumption that line resistances are negligible does not hold, and the existing reactive power control methods have less accuracy[53]. Due to the resistive nature of distribution grids, voltage regulation through active power control is much more effective[55]. The disadvantage of active power control is the need for a larger energy storage capacity. This increases the cost of the BESS and makes it less viable against traditional grid improvements.

Combined power control takes advantage of the independent control of active and reactive power in the VSC. This makes it possible to create a control strategy that can inject both reactive and active power into the grid. For grids with a low X/R ratio, this method of control can provide better voltage control than pure reactive power control[56]. A BESS controlled by combined power control can use reactive power to operate with a smaller energy storage capacity. At the same time, it can use active power for grids with higher resistance. By knowing or estimating the grid characteristics, it is possible to calculate the optimal combination of injected power. In section 5.1 the chosen control strategy is discussed.

In chapter 6, the results of simulation using all three control methods are shown, with further discussion about the results in chapter 7.

2.6 Converter technology

Converting between ac and dc by power electronics was dominated by naturally commutating CSCs up until the 1970s. Their main application was rectification to be used for dc motors and industrial processes. With the invention of controllable power semiconductors with turn-off capability, the VSC became more prevalent because of its increased controllability and improved harmonic performance[57]. The two-level voltage source converter (2L-VSC) is by far the most commonly used VSC for applications up to around 1800V. It is used for home applications, industrial drives and drive systems in EVs. It is also found in grid applications for connecting RESs to the electrical grid. For high-voltage applications, multilevel conversion topologies like the three-level neutral point clamped converter (NPC) and the modular multilevel converter (MMC) are more cost-effective and have improvements in the harmonic properties[57]. CSC, NPC and MMC will not be reviewed further, as they are not within the scope of this thesis.

2.6.1 The Two-level Voltage Source Converter

Figure 2.12 shows the schematic diagram of the three-phase 2L-VSC. The converter consists of three identical half-bridge converters with series-connected semiconductors (S_1 to S_3'). These are commonly a unidirectional controllable switch like an insulated-gate bipolar transistor (IGBT) and an anti-parallel diode. The ac-side of each half-bridge converter is interfaced with one phase of the three-phase ac-system (a, b, and c). This setup

allows for bidirectional power flow in a four-quadrant operation between the dc-side and the three-phase ac-side[58]. Four-quadrant operation means that the converter can independently control the active and reactive power to the grid, in either direction. To maintain the dc-side voltage approximately constant for a fraction of a fundamental cycle, regardless of the ac-side currents, two dc-capacitors (C) are connected in series. This forms the dc terminals of the converter[57]. On the ac-side, an inductance and capacitor (LC) filter (C' and L) is connected to reduce the switching ripple current and voltages at the ac-side during the short timeframe between commutations of a phase leg[59].

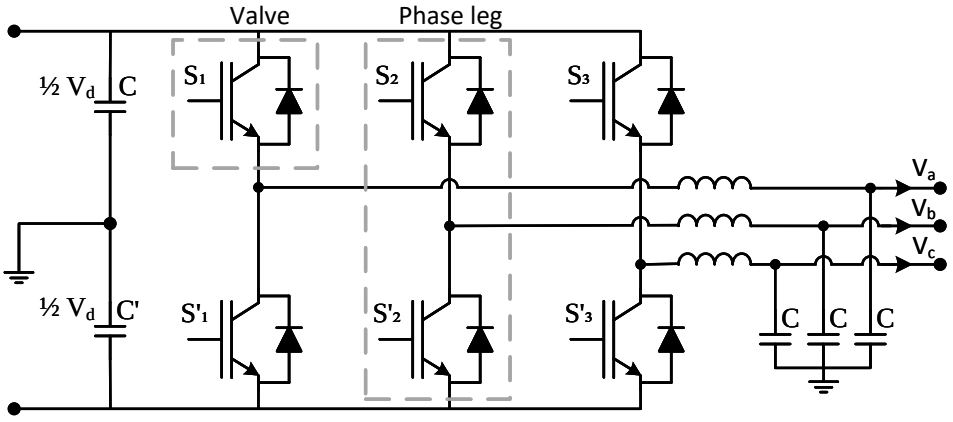

Figure 2.12: Three phase two-level voltage source converter.

Figure 2.13 explains the different steps of a commutation cycle in a 2L-VSC[57]. It is assumed that the ac-side current is flowing out of the terminal as indicated by the arrows. During the switching cycles, voltage on the ac-side will switch between two levels (hereby the name 2L-VSC) of $\frac{1}{2}V_{dc}$ and $-\frac{1}{2}V_{dc}$. The switches operate at a significantly higher frequency than the fundamental frequency of the ac-side. By controlling the timing of each switch, a desired ac-voltage can be achieved[57].

The VSC model designed and implemented in this thesis is the 2L-VSC. A grid-connected BESS in the low voltage distribution grid makes the 2L-VSC a good solution for this application. In chapter 3 the modelling of the VSC and the inner loop controller is presented.

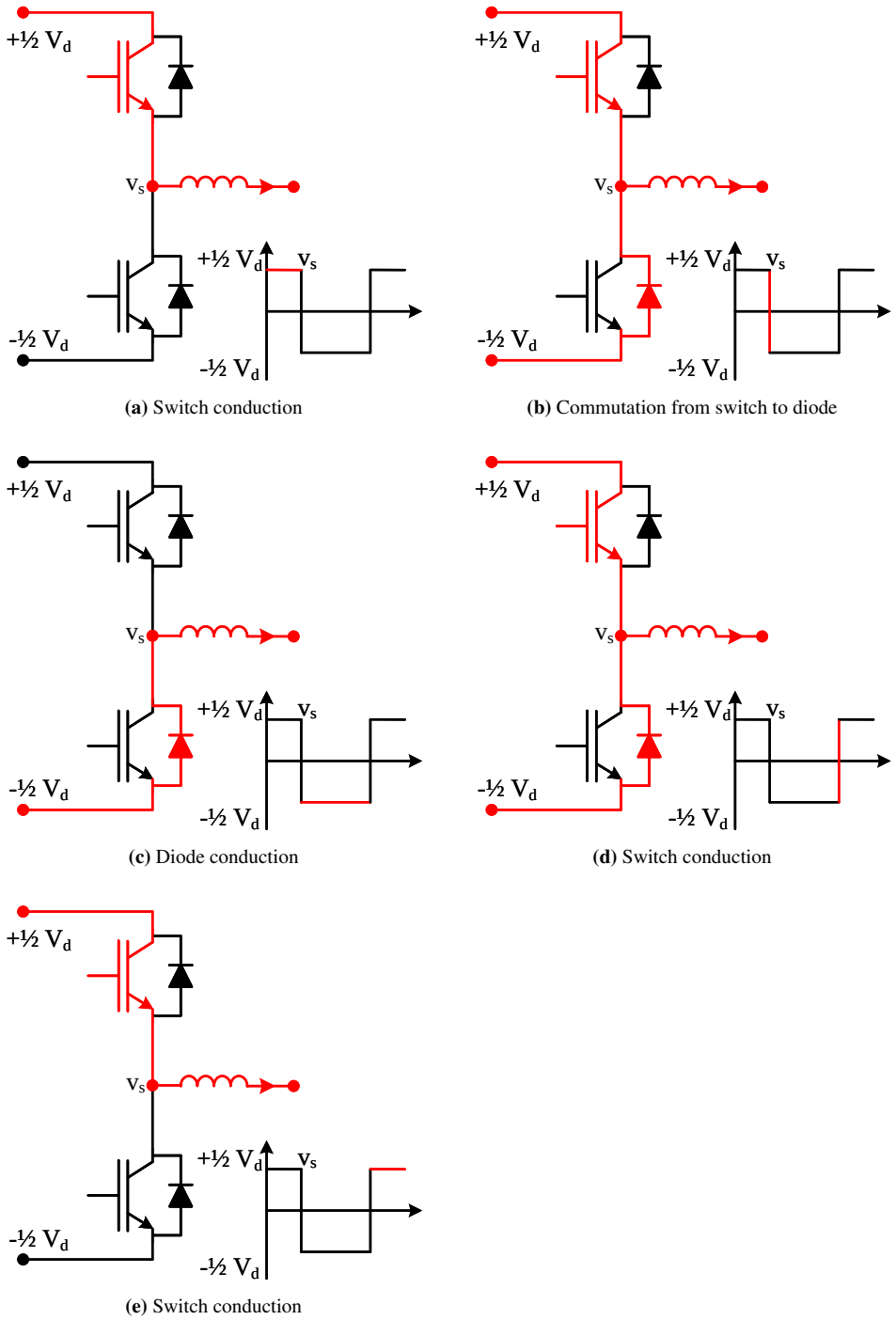

(a) Switch conduction

(b) Commutation from switch to diode

(c) Diode conduction

(d) Switch conduction

(e) Switch conduction

Figure 2.13: Switching operation for one phase leg of a 2L-VSC. Adapted from [57].

3

Modelling

This chapter introduces the modelling in the thesis. The ac three-phase system is introduced, and the transformations into a two-phase representation in a per-unit system. State space modelling is presented for nonlinear and linear modelling. The modelled voltage source converter (VSC) is presented and the Simulink model used for simulations of the grid and VSC is presented.

3.1 Three-Phase Systems

A three-phase ac-network, defined as a three-phase system in this thesis, is a set of three oscillating phase quantities with the same angular frequency. For a general three-phase system, the phases a, b and c ideally lag $120°(2\pi/3\text{rad})$ and $240°(4\pi/3\text{rad})$ behind phase a. A fundamental-frequency three-phase system can be defined as [57]

$$\begin{aligned} v_a &= \hat{V}_a cos(\omega t + \varphi_a) \\ v_b &= \hat{V}_b cos(\omega t - 2\pi/3 + \varphi_b) \\ v_c &= \hat{V}_c cos(\omega t - 4\pi/3 + \varphi_c) \end{aligned} \tag{3.1}$$

where $v_{a,b,c}$ are the phase voltages, $\hat{V}_{a,b,c}$ are the peak phase voltage, $\varphi_{a,b,c}$ are the phase angles and ω is the angular frequency of the grid.

3.1.1 Balanced Three-phase System

For a balanced three-phase system, the phase shift between phases is exactly $120°$ ($\varphi_{a,b,c} = 0$) and the peak values are identical. This gives two important properties:

- The sum of instantaneous voltages is zero ($v_a + v_b + v_c = 0$).

- The sum of the squared instantaneous voltages is constant ($v_a^2 + v_b^2 + v_c^2$ =constant).

The first property implies that only three-phase connections are necessary, as a neutral current path is not needed. The second property implies that the instantaneous power is kept constant[57]. For an imbalanced system, the phase shift between phases is not exactly $120°$, and the peak values are not necessarily equal. Imbalanced systems are not within the scope of this thesis and will not be reviewed further.

3.1.2 Two-Phase Representation

For a balanced three-phase system (and an imbalanced system, where zero-sequence components are disregarded), it is possible to reduce the three-phase system to an equivalent two-phase system. This transformation is called *Clarke transformation* and is defined as

$$\boldsymbol{v}^s = v_\alpha + jv_\beta = \frac{2}{3}K(v_a + e^{j2\pi/3}v_b + e^{j4\pi/3}v_c) \tag{3.2}$$

where K is a scaling constant explained below and $\boldsymbol{v}^s = v_\alpha + jv_\beta$ is a space vector with the quantities α and β. These are $90°$ phase-shifted from each other and can be projected on a complex plane for convenience. This reference frame is called a *stationary reference frame* or the $\alpha\beta$-frame[57]. It is also possible to write the transformation and the inverse transformation to go back to a three-phase system in matrix form. The transformation matrices are shown in appendix A.5.

Transforming the three-phase system to a two-phase representation in the form of equation (3.2) reduces the number of required control loops from three to two. However, since the Clarke transformation is a stationary reference frame, the reference, feedback and feedforward signals are still in sinusoidal form and it is not straightforward to achieve acceptable performance and steady-state errors for the system. A solution to this problem, and the one utilized in this thesis is to transform the $\alpha\beta$ frame to a *synchronously rotating reference frame*, the dq-frame [58]. This transformation is called *Park transformation* and it enables a three-phase system to be represented as a two-phase system where the signals assume dc-waveforms under steady-state conditions. The control systems needed to control this are less complex, and zero steady-state error can be achieved by adding an integrator to the controller. Another advantage is that the dq-frame is more suitable for analysis and control design, explained further in section 3.1.3. The Park-transformation is defined as

$$\boldsymbol{v} = v_d + jv_q = e^{-j\omega t}\boldsymbol{v}^s = e^{-j\omega t}(v_\alpha + jv_\beta) \tag{3.3}$$

where $\boldsymbol{v} = v_d + jv_q$ is a space vector on the complex plane with the quantities d and q phase shifted $90°$ from each other. This transformation and its inverse can be rewritten in matrix form, shown in appendix A.5.

As the $\alpha\beta$-frame is not used directly in this thesis, it is possible to transform a three-phase system directly to the dq-frame using the $dq0$-transformation matrix in equation (3.4). By combining the Clarke and Park transformation, the transformation is on the matrix form defined as

$$\begin{bmatrix} x_d \\ x_q \\ x_0 \end{bmatrix} = K \begin{bmatrix} \frac{2}{3}\cos(\omega t) & \frac{2}{3}\cos(\omega t - \frac{2\pi}{3}) & \frac{2}{3}\cos(\omega t + \frac{2\pi}{3}) \\ -\frac{2}{3}\sin(\omega t) & -\frac{2}{3}\sin(\omega t - \frac{2\pi}{3}) & -\frac{2}{3}\sin(\omega t + \frac{2\pi}{3}) \\ \frac{1}{3} & \frac{1}{3} & \frac{1}{3} \end{bmatrix} \begin{bmatrix} x^a \\ x^b \\ x^c \end{bmatrix} \tag{3.4}$$

where x_0 is the zero-sequence component. This component is not necessary for a balanced system, and therefore greyed out in the matrix. Only the two upper rows are necessary to transform the system into the dq-frame. The zero-sequence component will not be used further in this thesis.

Scaling Constant

The scaling constant K used in the Clarke transformation is used to scale the transformation for different purposes, and can be chosen arbitrarily. There are three common scaling constants used[57].

- Peak-value scaling: $K = 1$
- rms-value scaling: $K = 1/\sqrt{2}$
- Power-invariant scaling: $K = \sqrt{3/2}$

In this thesis, the peak-value invariant scaling constant is used, such that the amplitude of the phase variable is scaled with the amplitude of the space vector in the dq-frame.

3.1.3 Instantaneous Power

The three-phase complex power in the dq-frame is given as

$$S = P + jQ = \frac{3}{2K^2}\boldsymbol{v}\boldsymbol{i}^* \tag{3.5}$$

where $\boldsymbol{i}$ is the space vector in the dq-frame of the three-phase current. By aligning the dq-frame on the real axis, such that the voltage vector is real-valued

$$\boldsymbol{v} = v_d + jv_q = v_d. \tag{3.6}$$

By adding equation (3.6) to equation (3.5), the complex power for a d-axis oriented reference frame becomes

$$P + jQ = \frac{3}{2K^2}v_d\boldsymbol{i}^* = \frac{3}{2K^2}v_d(i_d - ji_q) \tag{3.7}$$

where it can be seen that the active power is proportional to i_d and the reactive power is proportional to $-i_q$. The currents i_d and i_q become active-power producing and reactive-power consuming components[57]. Appendix A.6 shows how the complex power can be calculated in the dq-frame[16]. By aligning the voltage vector as in equation (3.6), the active and reactive power, p and q respectively in the dq-frame becomes

$$p = v^d i^d \tag{3.8}$$

$$q = -v^d i^q. \tag{3.9}$$

By enabling vector output-current control in the dq-frame, the active and reactive power can be independently controlled through the inner loop controller current controllers of the VSC. Detailed model and explanation can be found in the specialization project[16].

3.2 Per Unit System

The calculations and modelling in this thesis are done using a pu system to normalize system variables. Power systems operate on different voltage and power levels. A pu system simplifies the calculations and analysis by normalizing the quantities to a fraction of their corresponding base values. A pu value is defined as

$$\text{per-unit value} = \frac{\text{actual value}}{\text{base value}} \tag{3.10}$$

where the base value is chosen depending on the size of the power system[60]. There are different ways of defining a pu system, dependent on the use case. The system used in this thesis is based on [58] where the pu system is split into ac-side quantities and dc-side quantities. Table 3.1 shows the chosen base values for this thesis, where it can be seen that for the ac-side, the base power is chosen as the rated volt-ampere (VA) S_n of the VSC and the base voltage is chosen as the peak value of the phase voltage V_{ph}. The rated values of the VSC are shown in table A.4.1. The dc-side values are based on the ac-side. The base power is equal for both sides, while the dc-side voltage is chosen as twice the ac-side voltage, this is done to obtain an ac-side voltage of 1.0 pu from a dc-side voltage of 1.0 pu.

3.3 Nonlinear model

3.3.1 State-Space Representation

The nonlinear model used in this thesis is represented using a state-space model of the dynamic system. Assuming that the derivatives of the state variables are not explicitly functions of time, the nonlinear model can be written as a nonlinear time-invariant (NTI), or an *autonomous* system. On matrix form, this is a set of n first-order differential equations

$$\begin{aligned}
\dot{\boldsymbol{x}} &= \boldsymbol{f}(\boldsymbol{x}, \boldsymbol{u}) \\
\boldsymbol{y} &= \boldsymbol{g}(\boldsymbol{x}, \boldsymbol{u}) \\
\boldsymbol{x} &= \begin{bmatrix} x_1 & x_2 & \dots & x_n \end{bmatrix}^\intercal \\
\boldsymbol{u} &= \begin{bmatrix} u_1 & u_2 & \dots & u_r \end{bmatrix}^\intercal \\
\boldsymbol{y} &= \begin{bmatrix} y_1 & y_2 & \dots & y_k \end{bmatrix}^\intercal
\end{aligned} \tag{3.11}$$

Quantity	Symbol and expression	Note
Apparent power	$S_b = S_n$	Nominal VA of VSC
Voltage	$V_b = \sqrt{2}\hat{V}_{ph} = \sqrt{\frac{2}{3}}V_{l-l}$	Nominal phase voltage amplitude of VSC
Current	$I_b = \frac{2S_b}{3V_b}$	Nominal line current amplitude of VSC
Frequency	$\omega_b = \omega_g = 2\pi f_n$	Nominal grid frequency
Impedance	$Z_b = \frac{V_b}{I_b}$	Base impedance, ac-side
Capacitance	$C_b = \frac{1}{\omega_b Z_b}$	Base capacitance, ac-side
Inductance	$L_b = \frac{Z_b}{\omega_b}$	Base inductance, ac-side
Power	$P_{b,dc} = S_b$	Same as ac-side apparent power
Voltage	$V_{b,dc} = 2V_b$	Base voltage, dc-side
Current	$I_{b,dc} = \frac{P_{b,dc}}{V_{b,dc}} = \frac{3}{4}I_b$	Base current, dc-side
Impedance	$Z_{b,dc} = \frac{V_{b,dc}}{I_{b,dc}} = \frac{8}{3}Z_b$	Base impedance, dc-side
Capacitance	$C_{b,dc} = \frac{1}{\omega_b Z_{b,dc}} = \frac{3}{8}C_b$	Base capacitance, dc-side
Inductance	$L_{b,dc} = \frac{Z_{b,dc}}{\omega_b} = \frac{8}{3}L_b$	Base inductance, dc-side

Table 3.1: Base values of pu-system

where $\boldsymbol{f}$ are the first-order differential functions and $\boldsymbol{g}$ are the output functions. The state vector $\boldsymbol{x}$ refer to the state variables of the system, the input vector $\boldsymbol{u}$ refers to the input variables that influence the system and the output vector $\boldsymbol{y}$ are the output variables that observe the system [30].

The state variables of a system represent the information about a system that is necessary to determine future behaviour, independent of past behaviour. The state variables can be physical quantities, such as voltage, current or angle. They can also be abstract variables associated with the differential equations describing the dynamics of the system. The choice of state variables is not unique, but a minimal set of variables, along with the system inputs provide a complete description of the system's dynamic. Defining more than the minimum amount of state variables does not provide more information, and not all of them are linearly independent[30].

3.3.2 Nonlinear Model of Voltage Source Converter

Figure 3.1 shows the full block diagram the nonlinear model is derived from. The model was derived in the specialization project [16]. A short explanation of the different components will be introduced here. The complete model consists of:

- **Electrical system:** Grid parameters and inputs connected to the VSC.
- **Inner loop current controllers**: Two decoupled proportional–integral (PI) controllers controlling d-and q-axis currents.
- **Active damping:** High pass filter of oscillating voltage frequencies due to the LC filter.
- **phase locked loop (PLL)**: Grid synchronization to achieve independent control of active and reactive power.

Outer Loop Controller

The outer loop controllers in figure 3.1 are greyed out, as they have not been modelled in the state space representation. They control the current references in the VSC. Various methods of controlling the current references exist. Droop control is one of the methods used, and is presented here for the sake of clarity. Droop control is a method that allows for multiple inverter-based resources to be connected in parallel, and share the load depending on their power rating. A *droop* value is assigned to each inverter according to its power rating. In conventional droop control, the voltage and frequency vary linearly with the reactive and active power respectively[61]. The conventional droop control assumes that the active and reactive power are decoupled, which is true for mostly inductive grids. For high-resistive grids, this assumption is not valid. In these grids, methods involving adaptive inductance loops[62] have been proposed. Other methods called resistive droop, where the active power controls the voltage, and the reactive power controls the frequency have also been proposed[63].

In this thesis, no outer loop controllers for the current references have been modelled, as the goal of the thesis is to design and implement a MPC as the outer loop controller.

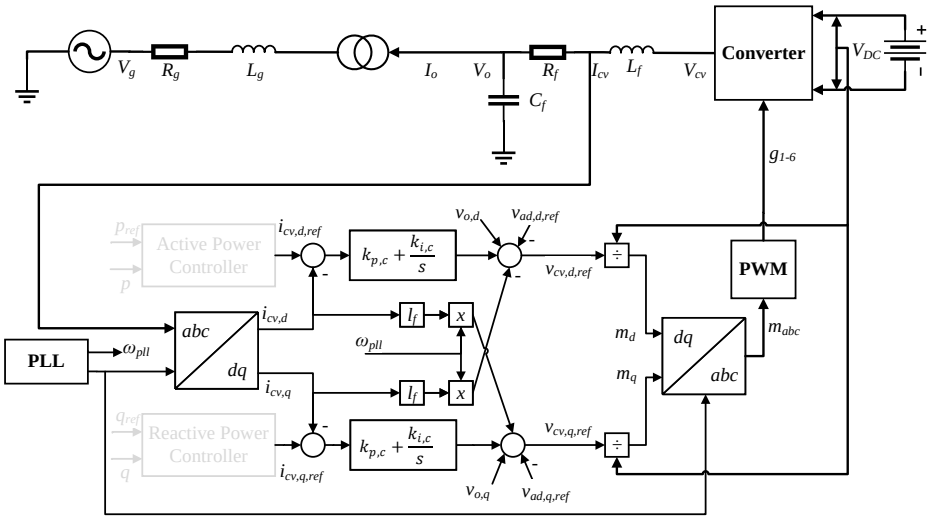

Figure 3.1: Model of VSC. Adapted from [16].

3.3.3 State Space Variables

From the VSC model in the specialization project[16], the state vector $\boldsymbol{x}$ introduced a total of 14 different state variables and the input vector $\boldsymbol{u}$ with 4 input variables. These states described the full inner controller of the VSC and consisted of the states

$$\begin{aligned}\boldsymbol{x} &= \begin{bmatrix} v_{o,d} & v_{o,q} & i_{cv,d} & i_{cv,q} & \gamma_d & \gamma_q & i_{o,d} & i_{o,q} & \varphi_d \\ & \varphi_q & v_{pll,d} & v_{pll,q} & \epsilon_{pll} & \delta\theta_{pll} \end{bmatrix}^\mathsf{T} \\ \boldsymbol{u} &= \begin{bmatrix} i^*_{cv,d} & i^*_{cv,q} & \hat{v}_g & \omega_g \end{bmatrix}^\mathsf{T}\end{aligned} \tag{3.12}$$

where the variables and subscripts are explained in the nomenclature. In addition to these states, four new state variables are introduced for measurement purposes. These four states are not linearly independent variables, and as such do not provide more information on the system's dynamics. They have been added for simpler implementation of the MPC in section 5.1. The new states are

$$\begin{bmatrix} p_{o,f} & q_{o,f} & \hat{v}_{o,f} & \hat{i}_{cv,f} \end{bmatrix}^\mathsf{T} \tag{3.13}$$

where the states are explained in the nomenclature. $p_{o,f}$ and $q_{o,f}$ are derived from the power calculations in appendix A.6. $\hat{v}_{o,f}$ and $\hat{i}_{cv,f}$ are derived from the dq-measurements of v_o and i_{cv} The equations for the measurements are

$$p_o = v_{o,d} i_{cv,d} + v_{o,q} i_{cv,q} \tag{3.14}$$
$$q_o = - v_{o,d} i_{cv,q} + v_{o,q} i_{cv,d} \tag{3.15}$$
$$\hat{v}_o = \sqrt{v_{o,d}^2 + v_{o,q}^2} \tag{3.16}$$
$$\hat{i}_{cv} = \sqrt{i_{cv,d}^2 + i_{cv,q}^2}. \tag{3.17}$$

By low-pass filtering equations (3.14)–(3.17), the nonlinear differential equations describing the four new states become

$$\frac{d}{dt} p_{o,f} = \omega_{lp,m}(p_o - p_{o,f}) \tag{3.18}$$
$$\frac{d}{dt} q_{o,f} = \omega_{lp,m}(q_o - q_{o,f}) \tag{3.19}$$
$$\frac{d}{dt} \hat{v}_{o,f} = \omega_{lp,m}(\hat{v}_o - \hat{v}_{o,f}) \tag{3.20}$$
$$\frac{d}{dt} \hat{i}_{cv,f} = \omega_{lp,m}(\hat{i}_c v - \hat{i}_{cv,f}). \tag{3.21}$$

The low pass filter constant $\omega_{lp,m} = 100000$ is kept equal for all four measurements and was chosen high to not filter the measurements. A different constant can be used if filtered measurements are needed.

The complete set of state variables, (including measurement states) and state inputs used in this thesis are

$$\begin{aligned} \boldsymbol{x} = \big[& v_{o,d} \quad v_{o,q} \quad i_{cv,d} \quad i_{cv,q} \quad \gamma_d \quad \gamma_q \quad i_{o,d} \quad i_{o,q} \quad \varphi_d \\ & \varphi_q \quad v_{pll,d} \quad v_{pll,q} \quad \epsilon_{pll} \quad \delta\theta_{pll} \quad p_{o,f} \quad q_{o,f} \quad \hat{v}_{o,f} \quad \hat{i}_{cv,f} \big]^\mathsf{T} \\ \boldsymbol{u} = \big[& i_{cv,d}^* \quad i_{cv,q}^* \quad \hat{v}_g \quad \omega_g \big]^\mathsf{T}. \end{aligned} \tag{3.22}$$

Output Variables

The output variables of the model are the state variables given in equation (3.22). As described in section 3.3.3, The additional measurements needed have been added to the state space model, the output vector $\boldsymbol{y}$ identical to the state vector $\boldsymbol{x}$. The output vector is defined as

$$\begin{aligned} \boldsymbol{y} = \boldsymbol{x} = \big[& v_{o,d} \quad v_{o,q} \quad i_{cv,d} \quad i_{cv,q} \quad \gamma_d \quad \gamma_q \quad i_{o,d} \quad i_{o,q} \quad \varphi_d \\ & \varphi_q \quad v_{pll,d} \quad v_{pll,q} \quad \epsilon_{pll} \quad \delta\theta_{pll} \quad p_{o,f} \quad q_{o,f} \quad \hat{v}_{o,f} \quad \hat{i}_{cv,f} \big]^\mathsf{T} \end{aligned} \tag{3.23}$$

.

Complete Model

The complete NTI system of the VSC, with all parameters and algebraic equations is shown in appendix A.2. A description of all model parameters is given in the nomenclature.

3.4 Small Signal Model

Small-signal stability of a power system is the ability to maintain synchronism when subjected to small disturbances. These disturbances occur due to variations in load and generation. The disturbances are considered small if the equations that describe the system can be linearized for stability analysis. In this thesis, the linear model is also used when deciding the system's input using the linear and adaptive MPC in section 5.1

For steady-state analysis of the linear model, the concept of an equilibrium point of the nonlinear model is necessary. A point $\boldsymbol{x} = \boldsymbol{x}_0$ in the state space is said to be an equilibrium point if the system starts in $\boldsymbol{x}_0$, that for all future time, the system stays in $\boldsymbol{x}_0$[64]. For the differential equation in equation (3.11), this point satisfies the equation

$$\boldsymbol{f}(\boldsymbol{x_0}, \boldsymbol{u_0}) = 0 \tag{3.24}$$

where $\boldsymbol{x_0}$ is the state vector, and $\boldsymbol{u_0}$ is the input vector at the equilibrium point. Using this point, a steady-state analysis can be done as shown in chapter 4.

The method used to linearize the system is to use the equilibrium point, or the current operating point, as explained in section 5.1.1. For some small perturbance around this point, the state vector and input vector is defined as [30]

$$\begin{aligned} \boldsymbol{x} &= \boldsymbol{x_0} + \Delta\boldsymbol{x} \\ \boldsymbol{u} &= \boldsymbol{u_0} + \Delta\boldsymbol{u} \end{aligned} \tag{3.25}$$

where Δ are small deviations around the operating point. The new states must satisfy equation (3.11), therefore the new NTI is defined as

$$\dot{\boldsymbol{x}} = \boldsymbol{f}\left[(\boldsymbol{x_0} + \Delta\boldsymbol{x}), (\boldsymbol{u_0} + \Delta\boldsymbol{u})\right]. \tag{3.26}$$

By using the first order Taylor's series expansion of equation (3.26), the linearized form of the model is expressed as[30]

$$\begin{aligned} \Delta\dot{\boldsymbol{x}} &= \boldsymbol{A}\Delta\boldsymbol{x} + \boldsymbol{B}\Delta\boldsymbol{u} \\ \Delta\dot{\boldsymbol{y}} &= \boldsymbol{C}\Delta\boldsymbol{x} + \boldsymbol{D}\Delta\boldsymbol{u} \end{aligned} \tag{3.27}$$

where the system matrices $\boldsymbol{A}$, $\boldsymbol{B}$, $\boldsymbol{C}$ and $\boldsymbol{D}$ are found from the jacobian of the nonlinear model equations equation (3.11). The system matrices around the operating point $\boldsymbol{x_0}$ and $\boldsymbol{u_0}$ are defined as

$$\begin{aligned} \boldsymbol{A} &= \frac{\partial \boldsymbol{f}(\boldsymbol{x},\boldsymbol{u})}{\partial \boldsymbol{x}}\Big|_{\substack{\boldsymbol{x}=\boldsymbol{x}_0 \\ \boldsymbol{u}=\boldsymbol{u}_0}} \quad \boldsymbol{B} = \frac{\partial \boldsymbol{f}(\boldsymbol{x},\boldsymbol{u})}{\partial \boldsymbol{u}}\Big|_{\substack{\boldsymbol{x}=\boldsymbol{x}_0 \\ \boldsymbol{u}=\boldsymbol{u}_0}} \\ \boldsymbol{C} &= \frac{\partial \boldsymbol{g}(\boldsymbol{x},\boldsymbol{u})}{\partial \boldsymbol{x}}\Big|_{\substack{\boldsymbol{x}=\boldsymbol{x}_0 \\ \boldsymbol{u}=\boldsymbol{u}_0}} \quad \boldsymbol{D} = \frac{\partial \boldsymbol{g}(\boldsymbol{x},\boldsymbol{u})}{\partial \boldsymbol{u}}\Big|_{\substack{\boldsymbol{x}=\boldsymbol{x}_0 \\ \boldsymbol{u}=\boldsymbol{u}_0}}. \end{aligned} \tag{3.28}$$

The nonlinear model in section 3.3 was linearized using the Matlab function *jacobian*. In the implementation of the controller, the system matrices are calculated in advance, and only updated using the operating point

3.4.1 Discrete Small Signal Model

For modelling and stability analysis, it is advantageous to use the continuous state space representation in equation (3.11) and equation (3.27). When implementing the system on a digital controller it is necessary to use the discrete-time representation. It uses a predefined sampling period that can be defined to run under the allowed computational time of the controller. The time-invariant small-signal discrete-time system is expressed as

$$\begin{aligned} \Delta\boldsymbol{x}[k+1] &= \boldsymbol{A}_d\Delta\boldsymbol{x}[k] + \boldsymbol{B}_d\Delta\boldsymbol{u}[k] \\ \Delta\boldsymbol{y}[k] &= \boldsymbol{C}_d\Delta\boldsymbol{x}[k] + \boldsymbol{D}_d\Delta\boldsymbol{u}[k] \end{aligned} \tag{3.29}$$

where k is the current time step and the system matrices $\boldsymbol{A}_d$, $\boldsymbol{B}_d$, $\boldsymbol{C}_d$ and $\boldsymbol{D}_d$ are derived from the continuous system matrices in equation (3.28) and appendix A.3 by discretizing them using[65]

$$\boldsymbol{A}_d = e^{\boldsymbol{A}T_s} \quad \boldsymbol{B}_d = \boldsymbol{A}^{-1}(\boldsymbol{A}_d - \boldsymbol{I})\boldsymbol{B} \quad \boldsymbol{C}_d = \boldsymbol{C} \quad \boldsymbol{D}_d = \boldsymbol{D} \tag{3.30}$$

where T_s is the sampling period of the discrete system. The subscript for separating continuous or discrete system matrices is omitted for the rest of the thesis. Whenever the continuous or discrete matrices are discussed, the systems being discussed will be understood from the context.

3.5 Simulink Model

The Simulink model is used for simulations of the real dynamics of the grid. It consists of a model of the VSC and a grid model. The MPC implemented in section 5.1 is used to simulate voltage support using a BESS in the distribution grid.

3.5.1 Voltage Source Converter Model

The inner loop current controller of the VSC used in the thesis consists of decoupled current control with feedforward and active damping of the ac-voltage. A PLL synchronises the *dq*-transformation to the grid. The Simulink model used was created at SINTEF Energy, and figure 3.1 illustrates the working principle of the model.

The VSC model has an inherent disturbance in the current injected when the grid voltage changes. In figure 3.2 The voltage with a changing load has been simulated. The current references $i_{cv,d}$ and $i_{cv,q}$ are zero, but the injected current is disturbed when the voltage changes. This characteristic is discussed more in chapter 7.

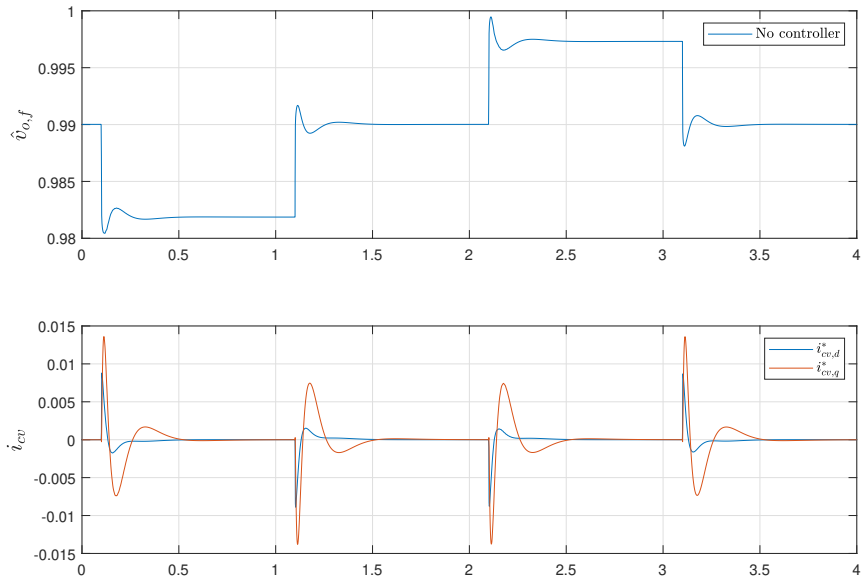

Figure 3.2: Disturbance in injected current from a change in grid voltage.

3.5.2 Grid Model

The grid model simulates a distribution grid with different load-drawing nodes. The grid model is implemented as a voltage source connected to a transformer in series with transmission lines connecting different load-drawing nodes. At the last node, a varying load and the grid-connected VSC model are connected. This gives these distinct parts of the model.

- **Voltage source:** A voltage source operating as the 22kV distribution grid. The source impedance is used in the Thevenin equivalent grid impedance.
- **Transformer:** A transformer transforming the 22kV high-voltage distribution grid down to the 400V low-voltage distribution grid. Winding impedances are modelled

to be used in the Thevenin equivalent grid impedance.

- **Load-drawing nodes:** Constant impedances simulating households and load demand.
- **Dynamic load:** A dynamic impedance at node 9 to simulate a changing load demand.
- **Transmission lines:** Series connected impedances to simulate the distance between nodes.
- **BESS:** A 20kW BESS is connected at the end-node for voltage support.

3.6 Thevenin Equivalents

For the nonlinear model of figure 3.1 to be accurate, the grid voltage v_g and grid impedance z_g must be estimated. Accurately estimating these values are important for high control stability and performance[66]. Distribution grids can have multiple energy sources, varying load changes and a complicated topology. This makes it difficult to accurately estimate the grid voltage and grid impedance that the VSC sees. One method of estimating these values is to find the equivalent Thevenin voltage and impedance of the grid. The Thevenin theorem states that a linear two-circuit terminal can be replaced by an equivalent circuit containing a voltage source v_{th} and an impedance z_{th}. v_{th} is the open-circuit voltage at the terminals and z_{th} is the equivalent impedance at the terminals when independent sources are turned off[67]. The equivalent circuit is illustrated in figure 3.3.

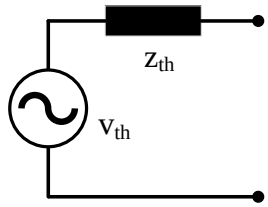

Figure 3.3: Thevenin equivalent circuit.

One way of obtaining the Thevenin equivalents at any point is to simply open circuit the terminals at the POI and measure the voltage. The measured voltage equals the Thevenin voltage. By then short-circuiting the terminals, the Thevenin impedance can be obtained measuring the short-circuit current. This method is impractical (or impossible) for continuously operating systems[68]. Therefore online methods of estimating the Thevenin equivalents must be used.

There are different methods for estimating the Thevenin equivalent for electrical grids. Methods such as least squares fitting for non-linear systems[66, 68] or through optimization methods[69, 70]. These methods are not within the scope of this thesis and therefore not reviewed further. In this thesis, the voltage and impedance of the grid model in

section 3.5.2 have been calculated as their respective Thevenin equivalents using circuit theory. The Thevenin voltage v_{th} and Thevenin impedance z_{th} are found using the parameters of the voltage source, transformer, lines and loads. In chapter 6 the Thevenin equivalents used for the simulations are calculated.

4

Verification of Model

This chapter presents the verification of the nonlinear and linear model. The nonlinear model is verified against the Simulink model, and the linear model is verified against the nonlinear model. For the linear model, different linearization points have been simulated to see how the operating point affects the accuracy of the model. The frequency response of the linear model is presented. The steady-state response for current injections is discussed for different grid parameters.

4.1 Verification of Nonlinear Model

The nonlinear model of the VSC in figure 3.1 was verified to be accurate against a simplified Simulink model in figure A.1.5 containing just Thevenin equivalents of the grid parameters. The simulation of the Simulink model was done with a sample time of 1 microsecond to ensure an accurate representation of all model dynamics. Simulating using a sample time of 1 microsecond is prohibitively time-consuming. Future simulations were therefore done with a sample time of 10 microseconds. System dynamics were still kept intact, except for very small deviations in the steady-state values.

The verification of the model was done using the grid and inner controller parameters from table 4.1. The grid impedance was given as $l_g = 0.2$ and $r_g = 0.1$.

In figures 4.1 and 4.2 it can be seen that the nonlinear model accurately represents the d-axis current dynamics of the Simulink model. There is no error in the steady-state value in the step response of the d-axis current. The simulation also shows that the inner controller of the VSC is stable and quickly reaches steady-state during a change in reference value. In figures 4.2a and 4.2b the transient response of the two models are shown. It shows that the nonlinear model also accurately represents the transient response of the d-axis current.

The d-axis voltage response was also simulated, as this not directly linked to change in the reference current. In figures 4.3 and 4.4 it can be seen that the nonlinear model accurately

Parameter	pu value	Parameter	pu value
l_f	0.08	kp_{pll}	0.0531
r_f	0.003	ki_{pll}	0.2947
c_f	0.074	$\omega_{lp,pll}$	50
l_g	0.2-.5	k_{ad}	1
r_g	0.01-0.5	ω_{ad}	50
kp_c	0.8488	ω_b	100 π
ki_c	10		

Table 4.1: Grid and model parameters for verification

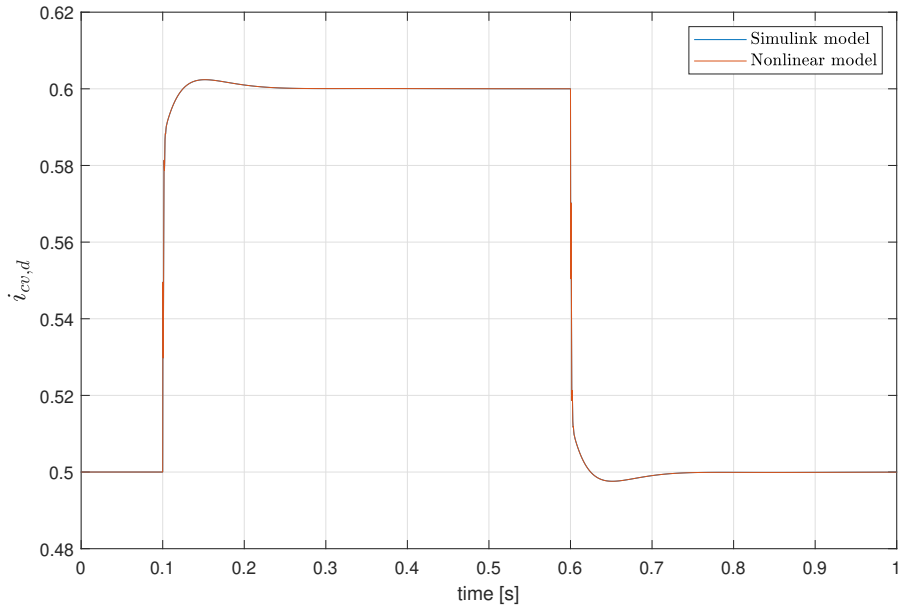

Figure 4.1: d-axis current step response of Simulink model and nonlinear model. $l_g = 0.2$ and $r_g = 0.1$.

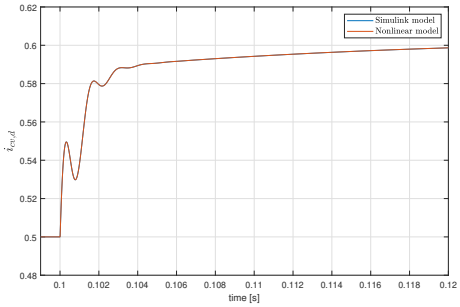

(a) Step reponse of 0.1 pu

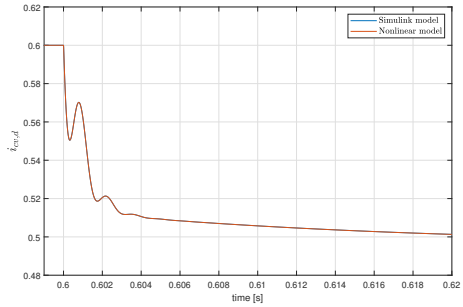

(b) Step response of -0.1 pu

Figure 4.2: d-axis current transient step response of nonlinear model and linearized model. $l_g = 0.2$ and $r_g = 0.1$.

represents the d-axis voltage dynamics of the Simulink model. There is no error in the steady-state value. In figures 4.4a and 4.4b the transient response of the two models are shown. It shows that the nonlinear model also accurately represents the transient response of the voltage dynamics.

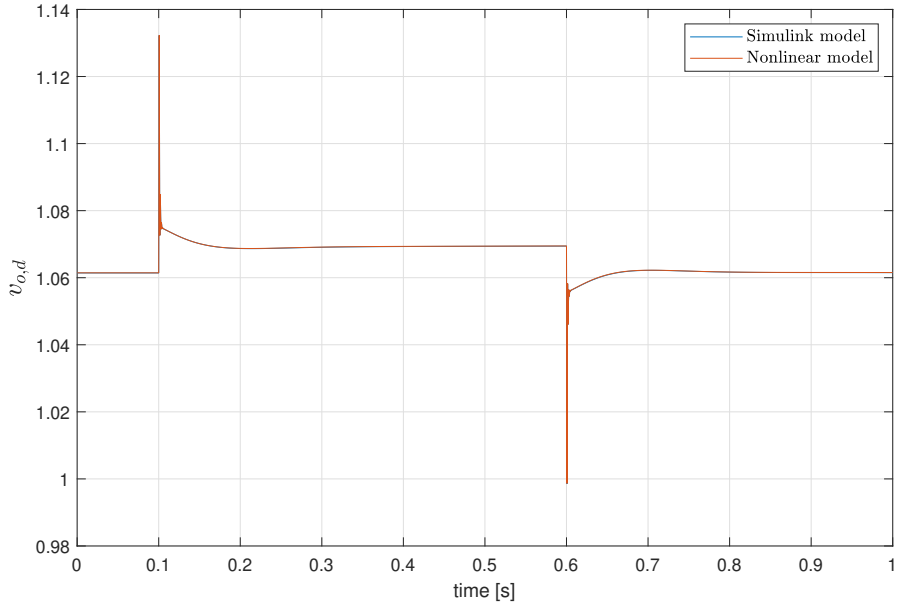

Figure 4.3: d-axis voltage step response of Simulink model and nonlinear model. $l_g = 0.2$ and $r_g = 0.1$.

The comparison between the simple Simulink model and the nonlinear model shows that

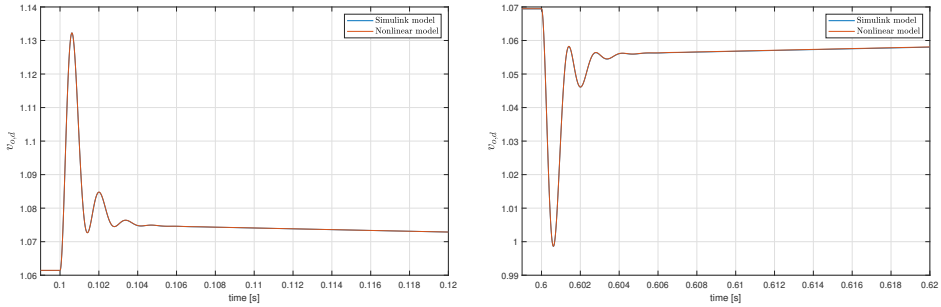

(a) Step reponse of 0.1 pu

(b) Step response of -0.1 pu

Figure 4.4: d-axis voltage transient step response of nonlinear model and linearized model. $l_g = 0.2$ and $r_g = 0.1$.

the nonlinear model in appendix A.2 is an accurate representation of the VSC.

4.2 Verification of Linear Model

The linear model was verified against the nonlinear model to see how different grid parameters and inputs affect the linearity of the model.

4.2.1 Step Response of linear model

The linear model was verified with the grid parameters in table 4.1, the same parameters as for the verification of the nonlinear model. Parameters were kept constant during the verification except for the grid impedance l_g and r_g. To verify the linearization, the step response of $i_{cv,d}$ and $v_{o,d}$ were plotted. The model was verified with an X/R ratio of 20 with the grid inductance $l_g = 0.2$ and $r_g = 0.01$. Further, the grid impedance was changed to see how this affects the linearity of the model.

The nonlinear model was linearized with the input values in table 4.2. All the inputs were constant during the verification except the reference value for the d-axis current $i^*_{cv,d}$. Different values were tested to see how changing the linearization point affected the accuracy of the linear model.

Parameter	pu value
$i^*_{cv,d}$	-1 to 1
$i^*_{cv,q}$	-1 to 1
$\hat{v}$	1
ω_g	1

Table 4.2: Input values for linearization of nonlinear model

X/R ratio of 20

The nonlinear model was linearized around $i^*_{cv,d} = 0.5$ pu, with the grid inductance $l_g = 0.2$. In figure 4.5 the step response of the linear model and the nonlinear model can be seen. $i^*_{cv,d}$ was changed from 0.5 pu to 0.6 pu at $t = 0.1s$. The linear model closely follows the nonlinear model. There is a similar overshoot in the d-axis current and the settling time of both models is the same. The d-axis current response of the system is fairly linear in nature. Figures 4.6a and 4.6b shows the transient response of the step-response. It can be seen that the response of the linear model closely follows the nonlinear model during the transient period.

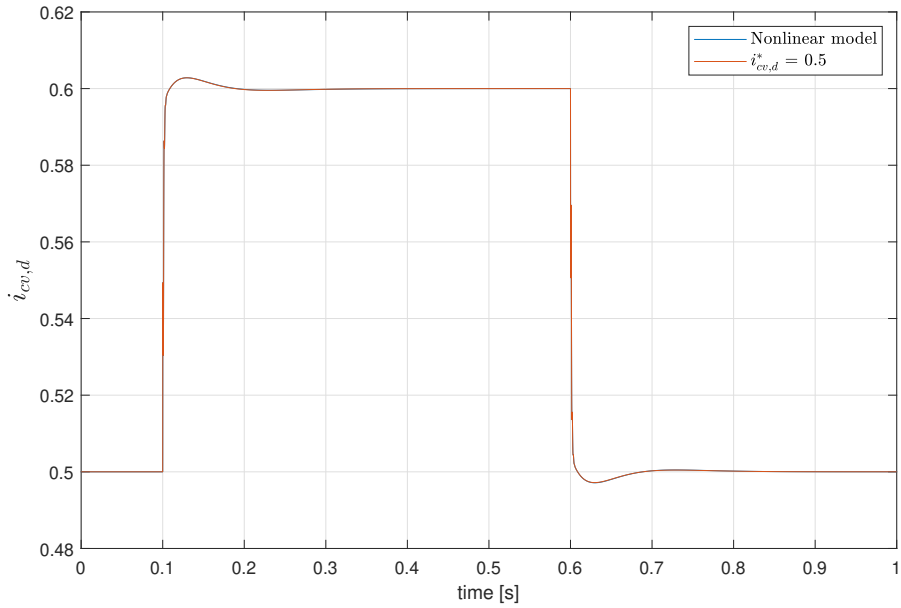

Figure 4.5: d-axis current step response of nonlinear model and linearized model. $l_g = 0.2$ and $r_g = 0.01$.

In figure 4.7 a comparison of different linearization points of $i_{cv,d}$ have been made. It can be seen that there are very small differences between the different linearization points with the grid impedance at $l_g = 0.2$ and $r_g = 0.01$. There is a small difference in the early dynamics of the step response, but there is no steady-state offset as can be seen at 0.5 seconds in the plot.

The d-axis voltage response of a step input change in the d-axis current was simulated at multiple linearization points of $i_{cv,d}$. In figure 4.8 the step response is plotted. It can be seen that the voltage is more susceptible to different linearization points than the current seen in figure 4.7. This shows the importance of a correct linearization point for accurate voltage control by the VSC.

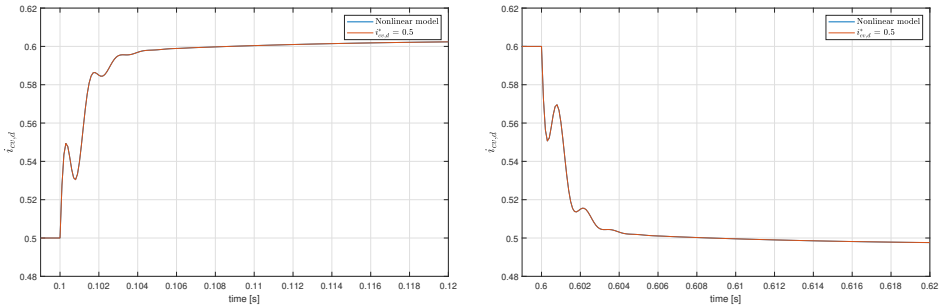

(a) Step reponse of 0.1 pu **(b)** Step response of -0.1 pu

Figure 4.6: d-axis current transient step response of nonlinear model and linearized model. $l_g = 0.2$ and $r_g = 0.01$.

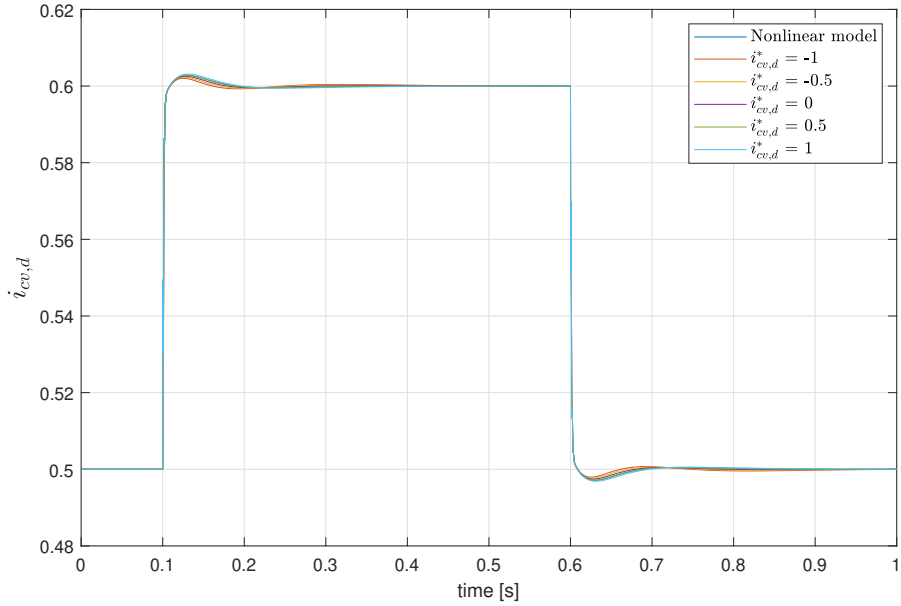

Figure 4.7: d-axis voltage step response at different linearization points. $l_g = 0.2$ and $r_g = 0.01$.

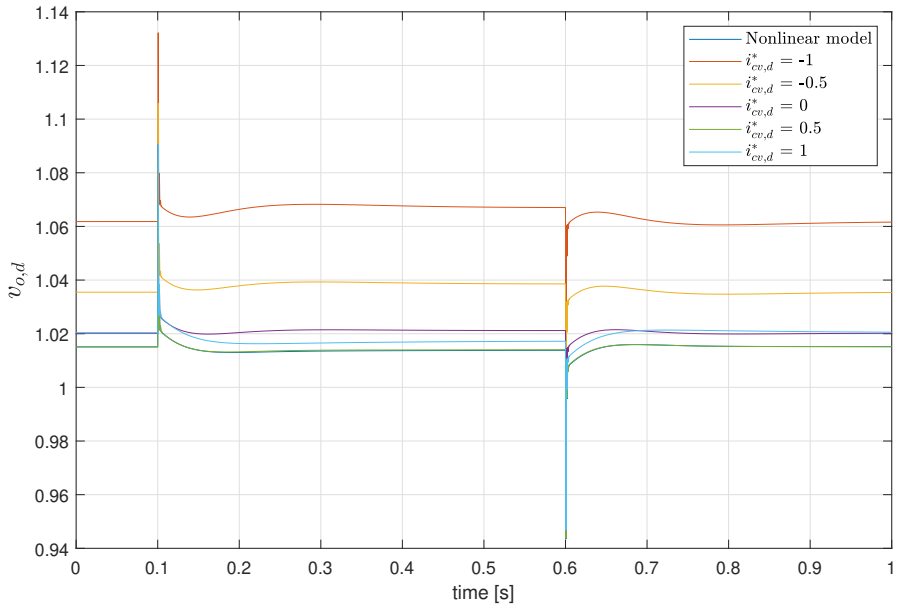

Figure 4.8: d-axis voltage step response at different linearization points. $l_g = 0.2$ and $r_g = 0.01$.

Grid Parameters Effect on Model

The grid parameters in a real distribution grid can have widely different values depending on the type of grid (overhead or underground cables), the age of the grid and the location of the measurements. As above, the system was linearized around different values of $i_{cv,d}$ and tested with a step response of the d-axis current reference $i^*_{cv,d}$ from 0.5 pu to 0.6 pu at $t = 0.1s$. In figure 4.9 the step response of the system with $l_g = 0.2$ and $r_g = 0.1$ was simulated. By comparing the figure to figure 4.7 it can be seen that the linearity of the current response is largely unaffected, but the dynamics of the response is slower for the higher value of grid resistance. The step response of $v_{o,d}$ with the same grid impedance parameters is shown in figure 4.10. By comparing it to figure 4.8 it can be seen that the voltage amplitude is higher for the same d-axis current, but the system shows a similar nonlinearity.

Two simulations with large values in the grid impedance were tested to verify that the nonlinearity is largely affected by the grid inductance, and not the grid resistance. In figures 4.11 and 4.12 the grid impedance was set to $l_g = 0.5$ and $r_g = 0.1$, and $l_g = 0.2$ and $r_g = 0.5$ respectively. It can be seen that the grid with a large inductance is less linear than the one with a high resistance. As explained in section 2.5.2 it can be seen that the amplitude of the voltage is more affected by a d-axis current in a high-resistance grid.

The VSC model is almost linear with respect to a change in the current reference. This can be explained by the current controller being mostly linear, assuming that the decoupling

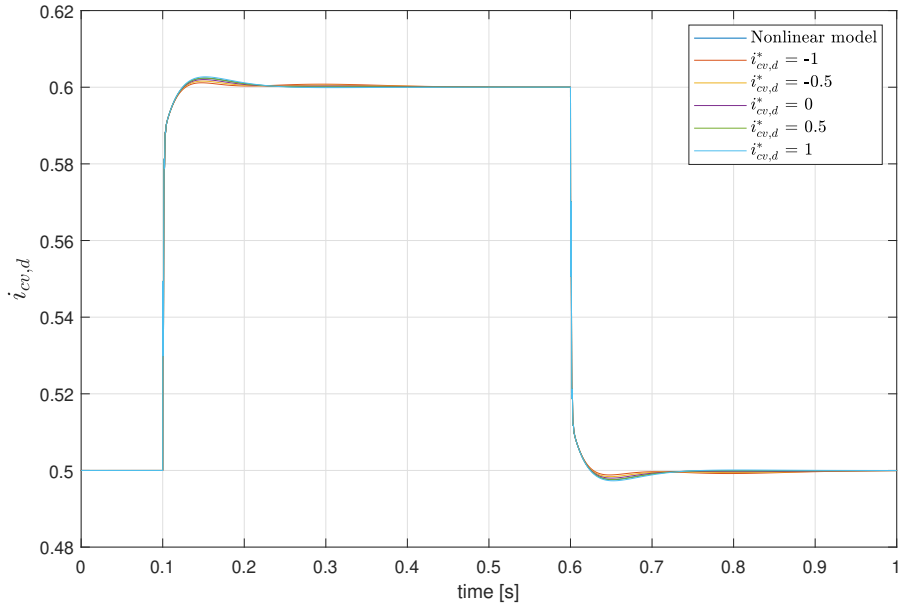

Figure 4.9: d-axis current step response at different linearization points. $l_g = 0.2$ and $r_g = 0.1$.

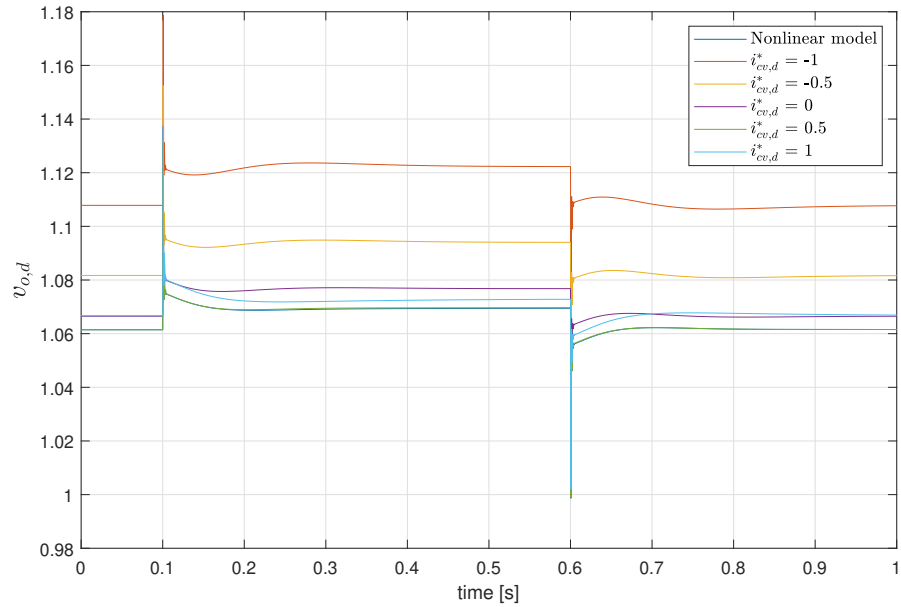

Figure 4.10: d-axis voltage step response at different linearization points. $l_g = 0.2$ and $r_g = 0.1$.

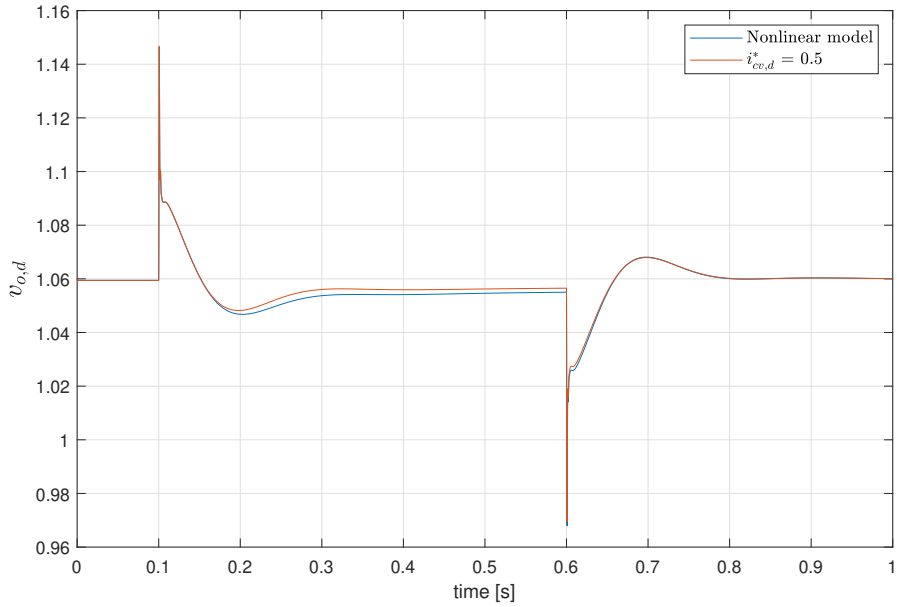

Figure 4.11: d-axis voltage step response linearized around 0.5 $i_{cv,d}$. $l_g = 0.5$ and $r_g = 0.1$.

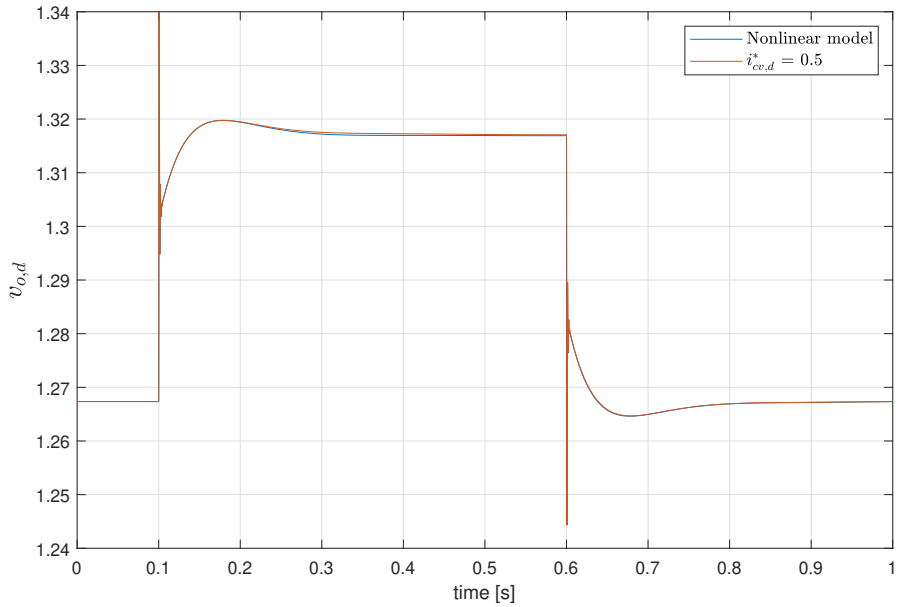

Figure 4.12: d-axis voltage step response linearized around 0.5 $i_{cv,d}$. $l_g = 0.2$ and $r_g = 0.5$.

link and feedforward in figure 3.1 works as intended. The main nonlinearity comes from the PLL, which for steady-state analysis is considered *locked*, and does not change.

4.2.2 Frequency Response

The frequency responses of the voltage amplitude $\hat{v_{o,f}}$ at different linearization points are looked at to see if there are any differences in how the voltage is affected for different frequencies of injected current. The grid parameters have been kept constant when looking at the frequency response. For the steady-state response, different grid characteristics have been tested, this can be seen in section 4.2.3.

In figure 4.13, the frequency response of the voltage amplitude $\hat{v}_{o,f}$ is reviewed for the d-axis current input $i^*_{cv,d}$. It can be seen that injecting d-axis current at different linearization points yields a different amplitude response of the voltage at low frequencies. At higher frequencies, this difference goes away, and the amplitude goes down.

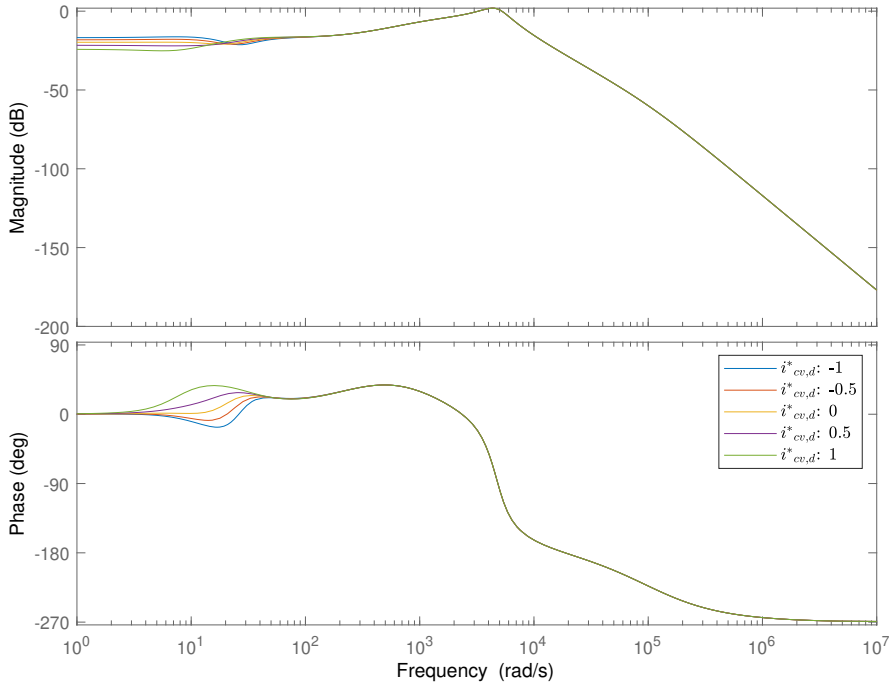

Figure 4.13: Frequency respone of $\frac{v_{o,f}}{i^*_{cv,d}}$ for different linearization points of $i^*_{cv,d}$. $l_g = 0.2$ and $r_g = 0.1$.

In figure 4.14, the frequency response of the voltage amplitude when injecting q-axis current for different linearization points of the q-axis current $i^*_{cv,d}$ can be seen. For the grid

parameters $l_g = 0.2$ and $r_g = 0.1$, there are very small differences in the response around all linearization points of $i^*_{cv,d}$.

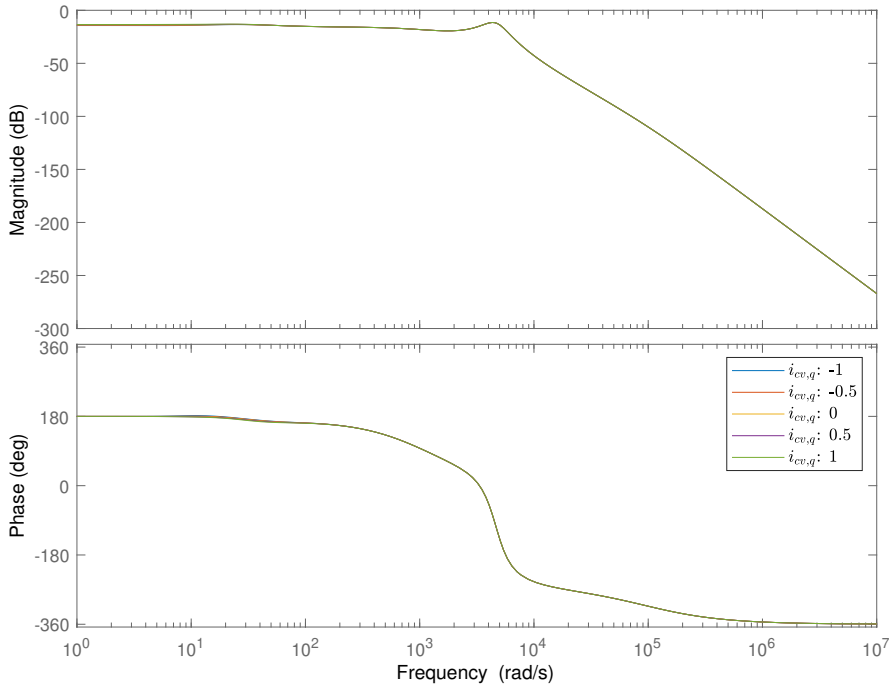

Figure 4.14: Frequency respone of $\frac{v_{o,f}}{i^*_{cv,q}}$ for different linearization points of $i^*_{cv,d}$. $l_g = 0.2$ and $r_g = 0.1$.

4.2.3 Steady-state Response

The steady-state response of the model was reviewed by injecting d- and q-axis currents at different grid parameters. This was done to review the effect of the grid parameters on the sensitivity of the voltage amplitude. The linearization point was selected as previously by table 4.2. The d-axis current $i_{cv,d}$ and q-axis current $i_{cv,d}$ are proportional and negatively proportional to the active and reactive power respectively. This together with the expected impact of current injection is explained in section 2.5.2. The red lines in figures 4.15–4.18 are to illustrate the upper and lower limits for the voltage amplitude set by FoL.

Voltage Response due to d-axis Current Injection

The steady-state response of the voltage amplitude when injecting d-axis current is shown in figures 4.15 and 4.16. The first simulation was done with a varying grid resistance r_g

from 0.1 to 0.5 pu and a constant grid inductance $l_g = 0.2$ In figure 4.15, the impact of grid resistance on the voltage amplitude when injecting d-axis current is shown. The voltage amplitude increases with increasing grid resistance. For very low values of the grid resistance, injecting d-axis current stops affecting the output voltage. For strong grids with a high X/R ratio, injecting active power has little effect on the voltage quality.

The impact of injecting d-axis current in a grid with changing grid inductance l_g from 0.1 to 0.5 pu and a constant grid resistance $r_g = 0.1$ is simulated in figure 4.16. As the grid resistance is set to $r_g = 0.1$, there is an inherent effect of injecting active power as shown in figure 4.15. Figure 4.16 shows that the voltage amplitude is less affected by a changing grid inductance. The voltage is negatively affected by injecting d-axis current. By comparing figures 4.15 and 4.16 it can be seen that the voltage amplitude in a grid with high inductance is negatively impacted by injection of d-axis current, for both a positive or negative injection. There is an inherent increase in voltage amplitude with an injection of d-axis current due to the resistance, but the voltage is lower for the corresponding high inductance grid.

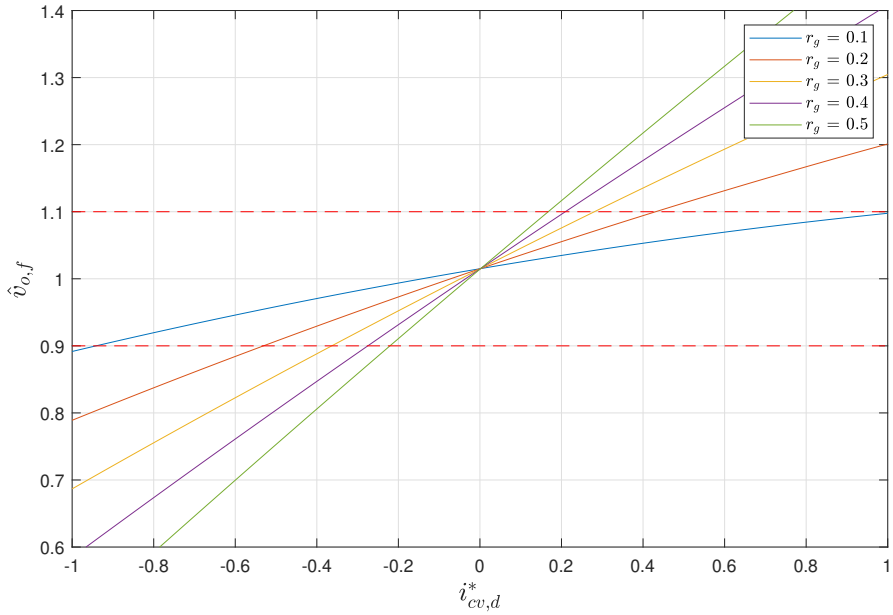

Figure 4.15: Steady-state response for change in $i^*_{cv,d}$ with $l_g = 0.2$ and r_g from 0.1 to 0.5.

Voltage Response due to q-axis Current Injection

The steady-state response of the voltage amplitude when injecting q-axis current is shown in figures 4.17 and 4.18. As explained in section 3.1.3, the reactive power injected into the grid is inversely proportional to the q-axis current $i_{cv,q}$. It is therefore expected that an increase in injected q-axis current leads to a decrease in grid voltage. The first simu-

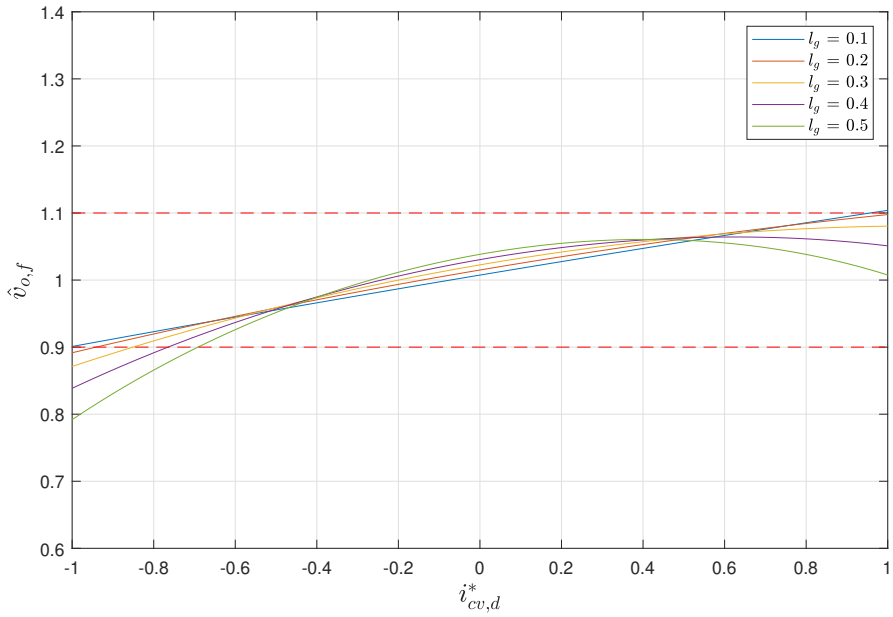

Figure 4.16: Steady-state response for change in $i^*_{cv,d}$ with l_g from 0.1 to 0.5 and $r_g = 0.1$.

lation was done with a varying grid resistance r_g from 0.1 to 0.5 pu and a constant grid inductance $l_g = 0.2$. In figure 4.17, the impact of grid resistance on the voltage amplitude when injecting q-axis current is shown. It can be seen that the injecting q-axis current negatively affects the voltage amplitude. This is expected as explained above. Similarly to d-axis current and grid inductance, increasing the grid resistance negatively affects the grid voltage amplitude. The voltage amplitude is higher for all points of q-axis current injection when the grid resistance is lower.

The impact of injecting q-axis current in a grid with changing grid inductance l_g of 0.1 to 0.5 pu and a constant grid resistance $r_g = 0.1$ is simulated in figure 4.18. The response is similar to d-axis current injection and inductance change. A higher amplitude of q-axis current results in a lower voltage amplitude when the resistance increases.

As figures 4.15–4.18 illustrates, the grid impedance has a large impact on the viability of a BESS. For a strong grid with low impedance, the voltage variations are lower, and the effect of a BESS will be negligible. For a grid with high impedance, both active and reactive power can lift the voltage in the grid efficiently.

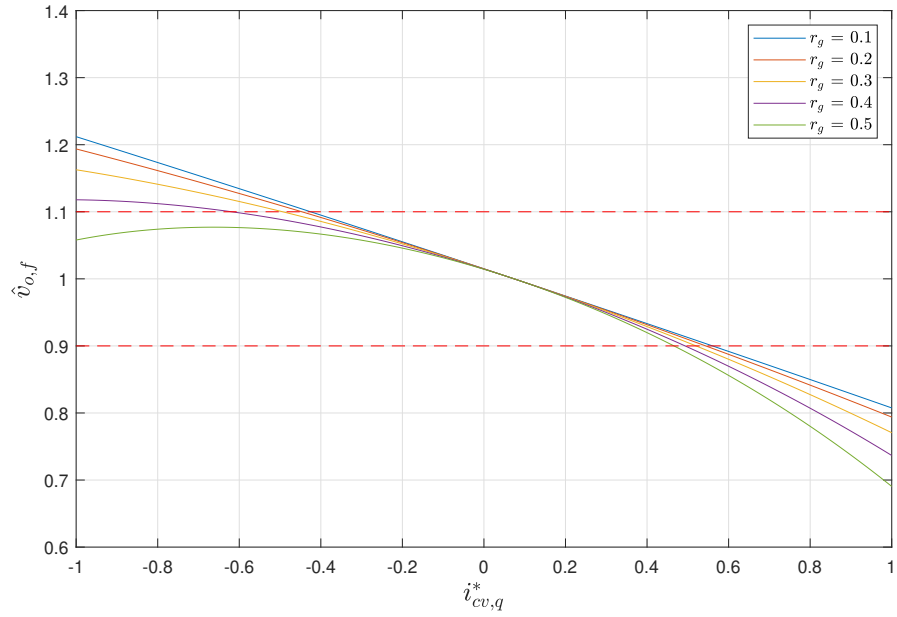

Figure 4.17: Steady-state response for change in $i^*_{cv,q}$ with $l_g = 0.2$

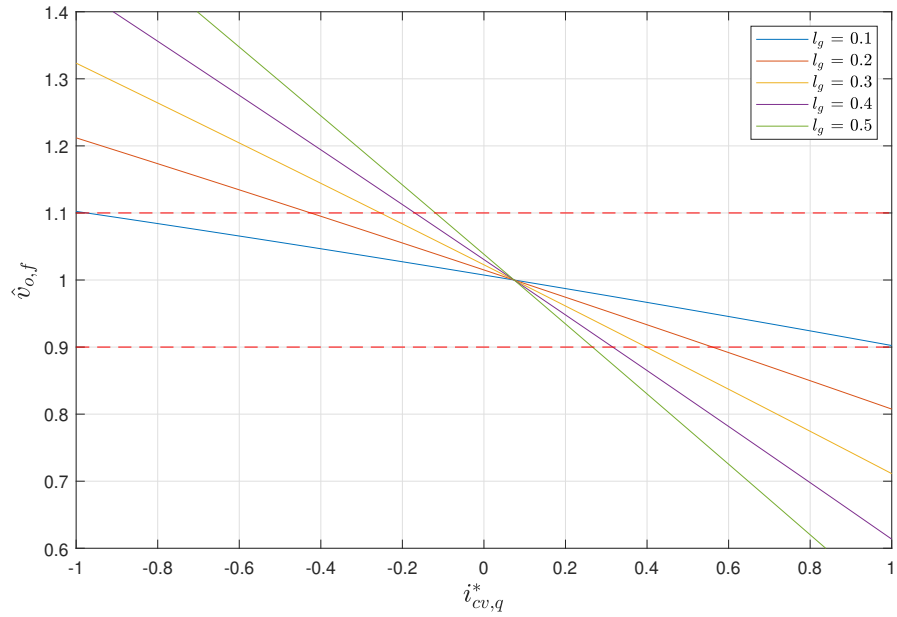

Figure 4.18: Steady-state response for change in $i^*_{cv,q}$ with $r_g = 0.1$

5

Control Strategy

This chapter presents the control strategy used in the thesis. The chosen control strategy model predictive control (MPC) is presented, with the different parameters for it. A formulation of the control objective is given. Two different MPC strategies are presented, a linear and an adaptive MPC. Their working principle, advantages and disadvantages are presented.

5.1 Model Predictive Control

MPC has become one of the most popular advanced control algorithms used today. For difficult multivariable control problems, it has become an important control technique. It is a method that allows controlling multiple-input, multiple-output (MIMO) processes while satisfying constraints on the input, output and state variables. By using an explicitly formulated dynamic model of the system, the current and future measurements of the system can be predicted and optimized. By formulating the optimization problem in different ways, it is possible to optimize the system for the wanted purpose, e.g. energy constraints, reference tracking or economic incentives.

MPC offers multiple advantages as a controller. It captures the dynamic and static dependencies between input, output, state and disturbance variables, while at the same time considering constraints in the system when deciding future control inputs. The control inputs are coordinated with the specified optimization equation, causing them to be calculated with the optimum set point in mind. With an accurate model, it is possible for early warnings of future potential problems. Using an inaccurate model may create a worse controller for the system, instead of a better one[71]. Therefore the success of an MPC (or any other model-based approach) is dependent on the accuracy of the model being used.

An MPC works by solving an optimization problem. At every time step of the controller, a finite horizon open-loop optimization problem is solved. The initial values of the problem

are the current states of the system plant. By doing this an optimal sequence of manipulated variables can be calculated and used as the input for the plant in the next time step[72].

5.1.1 MPC Variants

Two different MPCs are implemented. A linear and an adaptive MPC. These have different strengths and weaknesses. The formulation for the optimization problem is the same for both controllers, the difference is how the plant model is calculated. The linear MPC uses a plant model calculated before run time using the steady-state solution for zero current references and the Thevenin voltage as input. The adaptive MPC continuously updates the plant model using the current operating point of the plant.

Linear MPC

The linear MPC uses the plant model defined in equation (5.14) linearized around a constant operating point decided before run-time. This makes it ideal for a system where the operating point does not vary much. It has the smallest computational complexity since the linearization is only done once. This makes it ideal for linear plants or systems that only operate around the linearization point.

Adaptive MPC

The adaptive MPC is modified by continuously updating the linearization point around the current operating point of the system. Figure 5.1 shows the principal of the adaptive MPC. By continuously updating the plant model, the accuracy of the model is increased. It captures changes in the model that can occur due to changing operating conditions of the grid throughout the day. Slower long-lasting disturbances and shorter disturbances can be accurately captured by linearizing the system at every operating point. A difference compared to the linear MPC is that the adaptive MPC does not necessarily linearize around a steady-state point. If the model is updated during a disturbance, the calculated model is not necessarily linearized at an equilibrium point. This can cause strange results as shown chapter 6.

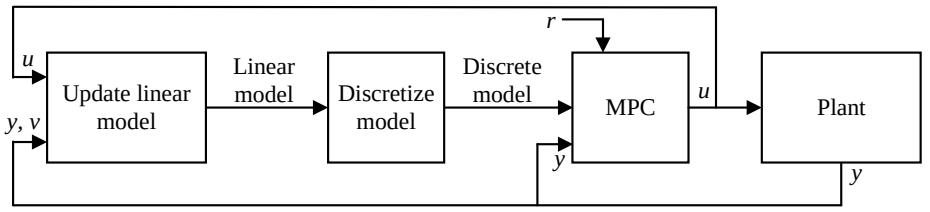

Figure 5.1: Adaptive MPC model.

5.1.2 Optimization Problem

An optimization problem consists of three main components. The *objective function* (also called cost function), the *decision variables* (also called manipulated variables) and the *constraints*. The objective function is a scalar function that describes the characteristics of the system that we want to maximize or minimize. The decision variables are the variables that can be manipulated to obtain the optimal solution for the objective function. These can have many forms such as vectors, integers or binary. In this thesis, they are vectors of real variables. The constraints consist of *equality constraints* and *inequality constraints*. They define equality, upper or lower limit functions that must be adhered to during the optimization[72]. The general form of an optimization problem, The nonlinear program (NLP) is defined as

$$\min_{\boldsymbol{z}\in\mathbb{R}^n} f(\boldsymbol{z}) \tag{5.1a}$$

subject to

$$c_i(\boldsymbol{z}) = 0, \quad i \in \mathcal{E} \tag{5.1b}$$

$$c_i(\boldsymbol{z}) \geq 0, \quad i \in \mathcal{I} \tag{5.1c}$$

where $\boldsymbol{z}$ is a vector of decision variables of n dimensions. The function f takes this as input and projects it onto the real axis. The equality constraints are defined by c_i on the disjunct sets $\mathcal{E}$ for the equality constraints and $\mathcal{I}$ for the inequality constraints. For this master thesis, the optimization problem is defined as a quadratic program (QP) problem. This is a subset of equation (5.1) where the objective function is quadratic and the constraints are linear. It is defined as

$$\min_{\boldsymbol{z}\in\mathbb{R}^n} \frac{1}{2}\boldsymbol{z}^\intercal H \boldsymbol{z}^\intercal + c^\intercal \boldsymbol{z} \tag{5.2a}$$

subject to

$$c_i(\boldsymbol{z}) = a_i^\intercal \boldsymbol{z} - b_i = 0, \quad i \in \mathcal{E} \tag{5.2b}$$

$$c_i(\boldsymbol{z}) = a_i^\intercal \boldsymbol{z} - b_i \geq 0, \quad i \in \mathcal{I} \tag{5.2c}$$

where the constraints are all linear, resulting in a convex feasible set. The objective function may be convex or nonconvex depending on the quadratic function and the constraints. If H is a positive semidefinite matrix, the QP equation (5.2) is a convex problem.

Convexity

Convexity is a concept that is of importance when solving an optimization problem. Convexity applies to both sets and functions. The following definition of convexity is from [73]: A set $S \in \mathbb{R}^n$ is a convex set if for any straight line segment connecting two points in S, stays entirely inside S. The definition for a convex set is that it is convex if its domain S is convex and for any two points x and y in S, the following property is satisfied

$$f(\alpha x + (1-\alpha)y) \leq \alpha f(x) + (1-\alpha) f(y), \text{ for all } \alpha \in [0,1]. \tag{5.3}$$

Quadadratic functions on the form equation (5.2a) are convex if H is a symmetric positive semidefinite matrix and $c \in \mathbb{R}^n$. a function f is said to be *concave* if $-f$ is convex. This lead to the conclusion that if both the objective function and the feasible region of the optimization problem are convex, then any local solution is a global solution. The general QP-problem in section 5.1.3 is a convex optimization problem if these three assumptions are satisfied.

- The objective function is convex.
- The equality constraints are linear.
- The inequality constraints are concave.

The advantage of utilizing this QP-formulation instead of a nonlinear formulation is this inherent characteristic of the linear model. It allows us to quickly find a global solution to the problem. A nonlinear optimization problem can be non-convex, which means that a local solution does not necessarily mean a global solution. The success of a nonlinear optimization algorithm depends largely on the initial guess for the solution[74].

5.1.3 Formulation of the Optimization Problem

The optimization problems used in this thesis are discussed in chapter 6. The controller can have two distinct operating modes. Either reference tracking, where the objective is to closely follow a specific voltage, or energy optimization where the objective is to minimize the amount of power that the BESS injects or draws from the grid. The objective function used in this thesis is formulated from MATLAB's MPC toolbox[75]. The linear and adaptive MPC use the same QP optimization problem formulation and constraints.

QP Optimization Problem

The QP formulation for the linear and adaptive MPC used in this thesis is from MATLAB's optimization problem documentation[76]. The objective function is defined as

$$\begin{aligned} J(\boldsymbol{z}_k) = \sum_{i=0}^{p-1} \big\{ &\left[\boldsymbol{e}_y^\intercal(k+i)\boldsymbol{Q}\boldsymbol{e}_y(k+i)\right] + \left[\boldsymbol{e}_u^\intercal(k+i)\boldsymbol{R}_u\boldsymbol{e}_u(k+i)\right] \\ &+ \left[\boldsymbol{\Delta u}^\intercal(k+i)\boldsymbol{R}_{\Delta u}\boldsymbol{\Delta u}(k+i)\right] \big\} + \rho_\varepsilon \varepsilon_k^2 \end{aligned} \tag{5.4}$$

where $\boldsymbol{z}_k$ is the QP decision variable. $\boldsymbol{Q}$, $\boldsymbol{R}_u$ and $\boldsymbol{R}_{\Delta u}$ are weighting matrices discussed in section 5.1.3. p is the prediction horizon, k is the current time-step and i is the current prediction step of the prediction horizon. ρ_ε is constraint penalty weight and ε_k is the slack variable. These are discussed in section 5.1.3. $\boldsymbol{e}_y$ is the output error, $\boldsymbol{e}_u$ is the deviation from the target input and $\boldsymbol{\Delta u}$ is the rate of change of the input variables. These are given by

$$\boldsymbol{e}_y(i+k) = \boldsymbol{r}(k+i+1) - \boldsymbol{y}(k+i+1) \tag{5.5}$$
$$\boldsymbol{e}_u(i+k) = \boldsymbol{u}_{target}(k+i) - \boldsymbol{u}(k+1) \tag{5.6}$$
$$\boldsymbol{\Delta u}(k+i) = \boldsymbol{u}(k+i) - \boldsymbol{u}(k+i-1) \tag{5.7}$$

where $\boldsymbol{r}$ is the reference vector and $\boldsymbol{u}_{target}$ is the target value for the input vector u equation (3.22). The output vector $\boldsymbol{y}$ is given by section 3.3.3. $\boldsymbol{r}$ and $\boldsymbol{u_{target}}$ are defined as

$$\boldsymbol{r} = \begin{bmatrix} r_1 & r_2 & \dots & r_{18} \end{bmatrix}^\intercal \tag{5.8a}$$
$$\boldsymbol{u}_{target} = \begin{bmatrix} 0 & 0 \end{bmatrix}^\intercal . \tag{5.8b}$$

QP Variables

The variables used for the QP-formulation in equation (5.4) are the same as the plant model variables in equations (3.22) and (3.23).The model uses four input variables, where only $i^*_{cv,d}$ and $i^*_{cv,q}$ are directly controllable by the VSC. $\hat{v}_g$ and ω_g are measured input variables that are not directly controllable. They are dependent on the supply voltage of the grid. For the implementation of the MPC, these are defined as

$$\begin{aligned} \boldsymbol{u} &= \begin{bmatrix} i^*_{cv,d} & i^*_{cv,q} \end{bmatrix}^\intercal \\ \boldsymbol{v} &= \begin{bmatrix} \hat{v}_g & \omega_g \end{bmatrix}^\intercal \end{aligned} \tag{5.9}$$

where $\boldsymbol{u}$ are manipulated variables that the MPC can adjust during operation. $\boldsymbol{v}$ are the measured disturbance variables and are not controllable.

QP Weighting

The output weighting matrice $\boldsymbol{Q}$ (n_y-by-n_y) allow the output variables to be weighted according to their importance. Reference tracking and energy optimization are simulated in chapter 6. The input and input rate weighting matrices $\boldsymbol{R}_u$ and $\boldsymbol{R}_{\Delta u}$ (n_u-by-n_u) allows the input variables to be weighted according to their importance. They suppress large input values and sudden changes to them. In this thesis these are kept constant, as suppressing input values are done by weighting either the current output or power output variables in the output weighting matrix. The weighting matrices are defined as

$$\boldsymbol{Q} = \begin{bmatrix} q_1 & 0 & 0 \\ 0 & \ddots & 0 \\ 0 & 0 & q_{18} \end{bmatrix} \tag{5.10a}$$

$$\boldsymbol{R}_u = \begin{bmatrix} 0.001 & 0 \\ 0 & 0.001 \end{bmatrix} \tag{5.10b}$$

$$\boldsymbol{R}_{\Delta u} = \begin{bmatrix} 1 & 0 \\ 0 & 1 \end{bmatrix} \tag{5.10c}$$

where the diagonal of the matrices defines the weighting of the corresponding variable. It is possible to adjust these over the duration of the prediction horizon, but for this thesis they have been kept constant.

QP Constraints

Model constraints for output, input and input rate variables are defined in the optimization problem. These are both physical constraints set by the rating of the VSC as well as self-defined constraints to achieve the desired results of the controller. An important aspect of implementing an MPC is the concept of *feasibility*. An optimization problem is *infeasible* if the optimization problem is not able to find a set of free variables (manipulated inputs) of the optimization problem such that all constraints are fulfilled. This can happen due to being close to constraints or after a large disturbance of the system. It is important that no feasible solution does not lead to the MPC not terminating and failing to continually update the manipulated inputs[77]. The Matlab MPC toolbox will use the most recent successful solution for the manipulated inputs if no feasible solution is found[75].

To ensure a feasible solution to the optimization problem, soft constraints are used in the controller by introducing the penalty weights ρ_ε in equation (5.4). If the variables are outside the bound of the constraint, the slack variable increases and in turn the objective function becomes larger. The optimization problem is still feasible and the controller terminates with a solution. The constraints in the MPC are implemented as

$$y_{j,min}(i) - \varepsilon_k V^y_{j,min}(i) \leq y_j(k+i) \leq y_{j,max}(i) + \varepsilon_k V^y_{j,max}(i) \tag{5.11}$$

$$u_{j,min}(i) - \varepsilon_k V^u_{j,min}(i) \leq u_j(k+i-1) \leq u_{j,max}(i) + \varepsilon_k V^u_{j,max}(i) \tag{5.12}$$

$$\Delta u_{j,min}(i) - \varepsilon_k V^{\Delta u}_{j,min}(i) \leq \Delta u_j(k+i-1) \leq \Delta u_{j,max}(i) + \varepsilon_k V^{\Delta u}_{j,max}(i) \tag{5.13}$$

where i is the current prediction step of the prediction horizon and j is the current variable of the input or output vector equations (3.22) and (3.23). $y_{j,min}(i)$, $y_{j,max}(i)$, $u_{j,min}(I)$, $u_{j,max}(i)$, $\Delta u_{j,min}(i)$ and $\Delta u_{j,max}(i)$ are the lower and upper bounds of the constraints, listed in table 5.1. The table only lists constrained variables, unconstrainted variables are left out. V are the penalty weights used for softening constraints, corresponding to ρ_ε in equation (5.4).

Constraint	Minimum	Maximum	Source of constraint
$p_{o,f}$	-1.1 pu	1.1 pu	Limit on max active power in VSC
$q_{o,f}$	-1.1 pu	1.1 pu	Limit on max reactive power in VSC
$\hat{v}_{o,f}$	0.92 pu	1.08 pu	Voltage regulation requirements
$\hat{i}_{cv,f}$	-1.1 pu	1.1 pu	Limit on max current in VSC
$i^*_{cv,d}$	-1 pu	1 pu	Limit reference current below max level.
$i^*_{cv,q}$	-1 pu	1 pu	Limit reference current below max level
$\Delta i^*_{cv,d}$	-1 pu	1 pu	Limit changes in reference current
$\Delta i^*_{cv,q}$	-1 pu	1 pu	Limit changes in reference current

Table 5.1: Output inequality constraints

Plant Model and Nominal Operating Point

The MPC uses a discrete small signal model equation (3.29) derived in section 3.4.1 to predict future behaviour of the system. The MPC uses the measured variables and disturbance variables defined in equation (5.9). The plant model expression is modified from equation (3.30) by theMPC toolbox[75] and defined as

$$\begin{aligned} \Delta \boldsymbol{x}[k+1] &= \boldsymbol{A}\Delta \boldsymbol{x}[k] + \boldsymbol{B}_u \Delta \boldsymbol{u}[k] \boldsymbol{B}_v \Delta \boldsymbol{v}[k] \\ \Delta \boldsymbol{y}[k] &= \boldsymbol{C}\Delta \boldsymbol{x}[k] + \boldsymbol{D}\Delta \boldsymbol{u}[k] \end{aligned} \tag{5.14}$$

where $\boldsymbol{B}_u$ and $\boldsymbol{B}_v$ are the new input matrices. These are calculated from the input matrix B in appendix A.3. The continuous small-signal is derived using the nonlinear model in appendix A.2 linearized using equation (3.28). This is then discretized with equation (3.30). As explained in section 5.1.1, the linear and adaptive MPC calculates the linear model in two different ways. The linear MPC calculates it before runtime using an equilibrium point. The adaptive MPC continuously updates the linear model during runtime at the current operating point at each time step for the MPC.

5.1.4 Prediction Horizon and Time Step

The time step T_s of an MPC decides how often the controller solves the optimization problem in section 5.1.3. For the adaptive MPC, the controller also calculates a new linear model. The prediction horizon p decides how far into the future the controller predicts at every time step. The calculated manipulated variables are a result of these two parameters.

The plant is simulated at a time step of 10 microseconds because of the quick dynamics of the power system. The switching frequency of the VSC is set to 10kHz. This frequency dictates the time step that the inner loop controller (and thus the simulated model) needs to operate at. The MPC can operate at a slower time-step to reduce the computational complexity. One recommended practice is to set the time-step T_s to 10% to 25% of the desired closed-loop response time T[75]. The desired close loop response is dependent

on the application of the MPC. For short-term voltage variations, the response time must be faster than for long-term voltage variations. As the MPC only update the manipulated variables at each time step, the system is only able to respond to disturbances when the controller runs.

Two different time steps were simulated in chapter 6, a faster MPC with a time step of 1 millisecond and a slower MPC with a time step of 50 milliseconds. The typical difference between the response of these two step times is illustrated in figure 5.2. As the figure shows, the quicker MPC is able to respond faster to disturbances. Further differences and advantages are discussed in chapter 7.

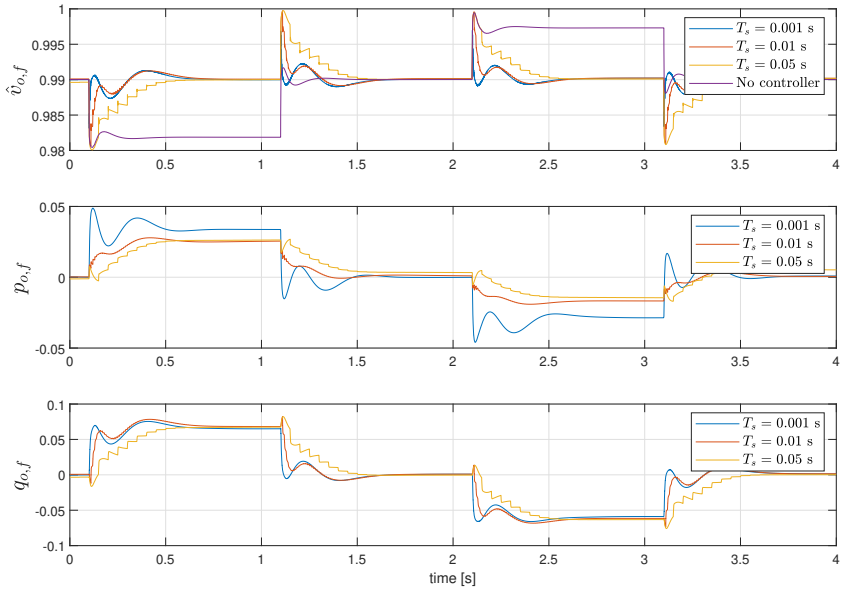

Figure 5.2: Response of MPC controller for different time steps T_s. Prediction horizon $p = 1$.

One tip for choosing the prediction horizon is to use the desired response time T and the chosen step time T_s to choose the prediction horizon p. Choosing $T = pT_s$ can work as a good initial value for the prediction horizon. If the time step is chosen as 10% of the desired response time, this results in a prediction horizon of 10. Another way to choose the prediction horizon is to use the response time of the inner loop current controllers. The prediction horizon is chosen long enough for a step-response of the inner loop current controllers from the current reference to reach steady-state. Figures 4.5 and 4.10 shows that the step response is dependent on the grid parameters, and the system reaches steady-state about 0.1 to 0.2 seconds after the change in input. This results in a prediction horizon of 0.2 seconds. For the controller with a time step of 50 milliseconds, the prediction horizon is $p = 4$. For the controller with a time-step of 1 millisecond, this results in a prediction horizon of $p = 200$, which is prohibitively long. Therefore the prediction horizon for the faster MPC is chosen according to the desired step response time. In figure 5.3

the differences between the prediction horizon for the faster controller are illustrated. It can be seen that the shorter prediction horizon results in a slower response time, but the prediction horizon above 5 starts giving diminishing returns. The prediction horizon for this controller is chosen as 10. For the slower MPC with a time step of 50 milliseconds, it can be seen in figure 5.4 that a prediction horizon above 5 does not change the response. Therefore the prediction horizon is chosen as 5 for the slower controller.

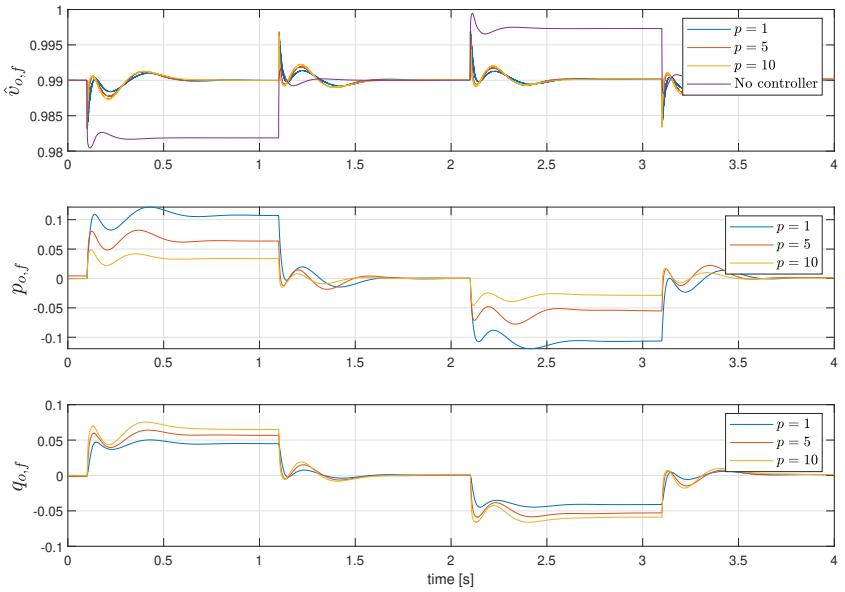

Figure 5.3: Response of MPC controller for different prediction horizons. Time step $T_s = 1$ millisecond.

For any implementation in real-time, the prediction horizon and time-step of the MPC need to be looked further into. The controller must be able to solve the optimization problem within the chosen time step, The control loop must also be faster than the system dynamics. This is not within the scope of the thesis and has not been reviewed further.

5.1.5 Control Parameters

The weighting matrices in equation (5.10) are used, with $\boldsymbol{R}_u$ and $\boldsymbol{R}_{\triangle u}$ chosen as equations (5.10b) and (5.10c). The output weighting matrix $\boldsymbol{Q}$ is chosen as equation (5.10a), with the weights q_1 to q_{14} equal to zero. The weights q_{15} to q_{18} are chosen depending on the used control strategy in chapter 6 according to

$$\boldsymbol{Q}_{15-18} = \begin{bmatrix} q_{15} & q_{16} & q_{17} & q_{18} \end{bmatrix}. \tag{5.15}$$

The reference target matrix r in equation (5.8a) is used with the references r_1 to r_{14} equal to zero. These are set to zero because the weights on the corresponding output are zero.

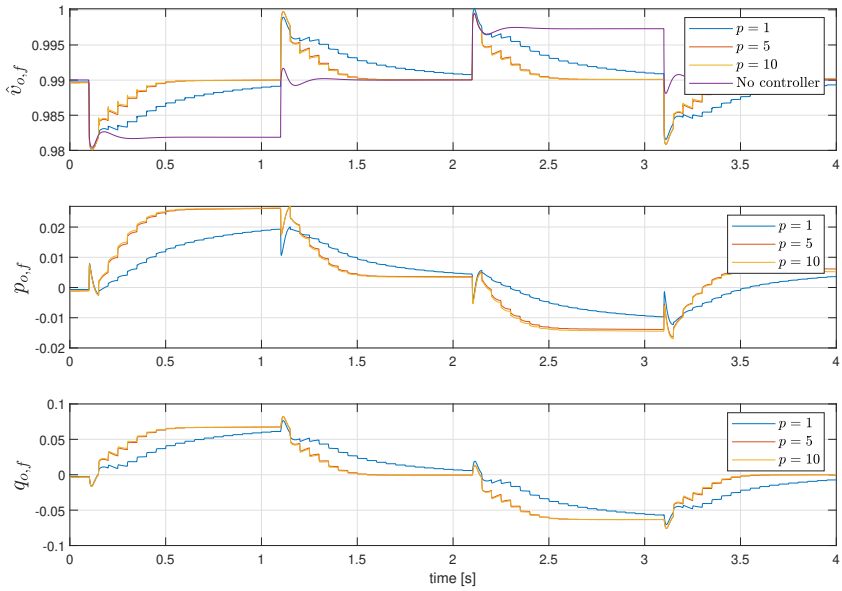

Figure 5.4: Response of MPC controller for different prediction horizons. Time step $T_s = 50$ milliseconds.

This results in an optimization problem that ignore outputs y_1 to y_{14} in the solution. The reference values r_{15} to r_{18} are chosen depending on the used control strategy according to

$$\boldsymbol{r}_{14-18} = \begin{bmatrix} r_{15} & r_{16} & r_{17} & r_{18} \end{bmatrix} \tag{5.16}$$

where the exact values are set for each test case of the simulation in chapter 6.

6

Simulation and Results

This chapter presents the simulation setup and results from three test cases. Test case 1 presents the results from reference tracking. Test case 2 presents the results from energy optimization. Test case 3 presents the results from combining test cases 1 and 2 into a combined reference tracking and energy optimization. The parameters used in the simulations are listed.

6.1 Simulation Setup

The VSC and grid model was simulated using the Simulink model from section 3.5. The AC-side of the VSC is connected in parallel at node 9 in the grid model as shown in figure A.1.2. At each node, a constant impedance is set up to simulate a load demand. Between each node, there is a line impedance simulating the distance between the nodes. Before node one, the secondary side of a transformer is connected. It transforms 22kV down to 400V. A voltage source is connected to the 22kV primary side of the transformer. The voltage source has an internal impedance simulating the grid behind it. Two different line impedances and voltage source impedances were used, simulating a strong and a weak grid. All grid parameters are listed in appendix A.4.

The Thevenin equivalent of the grid is calculated using the voltage source, transformer, line impedances and load impedances. The Thevenin equivalent is used in the linear model before run time, and updated at run time for the adaptive MPC.

Three different test cases were simulated and reviewed:

- Test case 1: Output reference tracking.
- Test case 2: Energy optimization.
- Test case 3: Combined reference tracking and energy optimization.

All three test cases were simulated in a weak grid, while test case 1 was also simulated in a strong grid. The simulation parameters are listed in tables A.4.1–A.4.4. Parameters specific for the strong grid are listed in tables A.4.5–A.4.7 and the specific parameters for the weak grid are listed in tables A.4.8–A.4.10. The simulations ran for 5 seconds, where the first 0.9 seconds and last 0.1 seconds are cut out in the plots. This is done for the model and MPC to reach steady-state before adding disturbances. All simulations are done with a sample time of 10 microseconds.

The figures are divided into three plots. The upper plot shows the voltage amplitude at the POI for the adaptive and linear MPC. The open loop system with no controller reacting to disturbances is also shown for reference. The middle plot shows the active power injected into the grid for the adaptive and linear MPC. The bottom plot shows the reactive power injected into the grid for the adaptive and linear MPC. A positive value indicates power flowing from the VSC into the grid. All values are presented in the *dq*-axis with pu values referred to the per unit system of the VSC.

6.2 Test case 1: Output Reference Tracking

The first test case is to see how well the controller is able to maintain a constant voltage after a sudden load change close to the BESS. This test case is to verify that the controller is able to maintain a stable voltage. This is not the most realistic application for a BESS as it needs to use more power to maintain a constant voltage. In most scenarios, a voltage within the thresholds set by FoL is satisfactory.

The weighting matrix is shown in equation (6.1). The penalty weights for using active or reactive power are not used, the only weight is on the voltage amplitude. The weights on input and input rates are the values set in equations (5.10b) and (5.10c).

$$\boldsymbol{Q}_{15-18} = \begin{bmatrix} 0 & 0 & 10 & 0 \end{bmatrix} \tag{6.1}$$

6.2.1 Strong Grid

The calculated Thevenin impedance of the grid (before any load change) is $z_{th} = 0.027 + j0.106$. The calculated Thevenin voltage is $v_{th} = 0.99$. The reference value of the voltage in equation (6.2) was set according to the steady-state value solved using *fsolve* in Matlab before run time. The corresponding Thevenin equivalents for the strong grid were used with zero current references as input. The linearized MPC is linearized at a current reference of zero and the Thevenin voltage.

$$\boldsymbol{r}_{14-18} = \begin{bmatrix} 0 & 0 & 0.99 & 0 \end{bmatrix} \tag{6.2}$$

The results of the MPC using voltage reference tracking in the strong grid are shown in figures 6.1 and 6.2 for $T_s = 1$ and $T_s = 50$ milliseconds respectively. In figure 6.1 it can be seen that the voltage dip in the strong grid is below 0.01 pu for a change in the load demand of 5kW. And similarly, the voltage swell is below 0.01 pu for a negative load

demand of 5kW. This means that there must be a large load demand for the voltage levels to go below any requirements set by FoL, as the strong grid is insensitive to load changes.

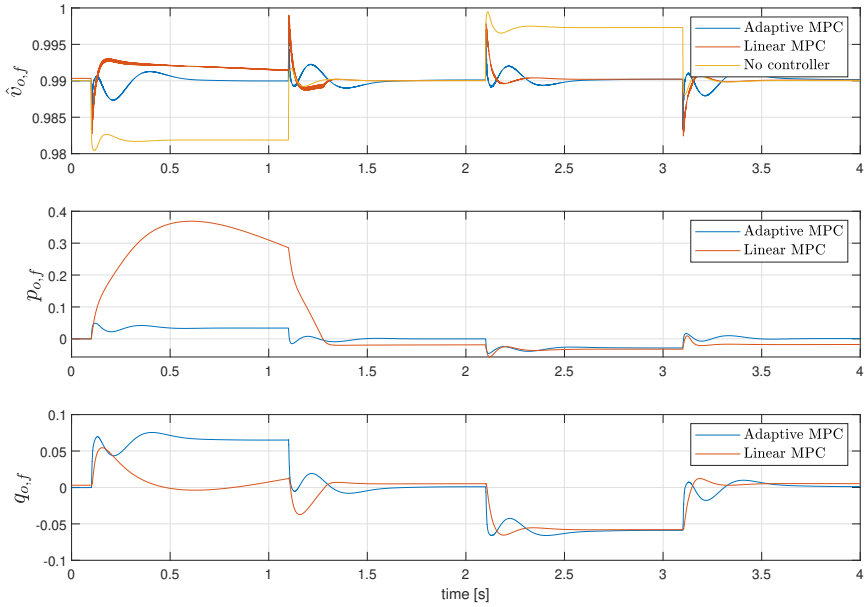

Figure 6.1: Voltage reference tracking with $T_s = 1$ millisecond in a strong grid.

6.2.2 Weak Grid

The calculated Thevenin impedance of the grid (before any load change) is $z_{th} = 0.213 + j0.196$. The calculated Thevenin voltage is $v_{th} = 0.924$. The reference value of the voltage in equation (6.3) was set according to the steady-state value solved using *fsolve* in Matlab. The corresponding Thevenin equivalents for the weak grid were used with zero current references as input. The linearized MPC is linearized at a current reference of zero and the Thevenin voltage.

$$\boldsymbol{r}_{14-18} = \begin{bmatrix} 0 & 0 & 0.937 & 0 \end{bmatrix} \tag{6.3}$$

The results of the MPC using voltage reference tracking in the weak grid are shown in figures 6.3 and 6.4 for $T_s = 1$ and $T_s = 50$ milliseconds respectively. It can be seen that the voltage dip is significantly higher than for the strong grid in figures 6.1 and 6.2. The voltage dips as low as 0.87 pu for a load change of 5kW at node 9. The weak grid is more sensitive to a change in the load than the strong grid in figure 6.2

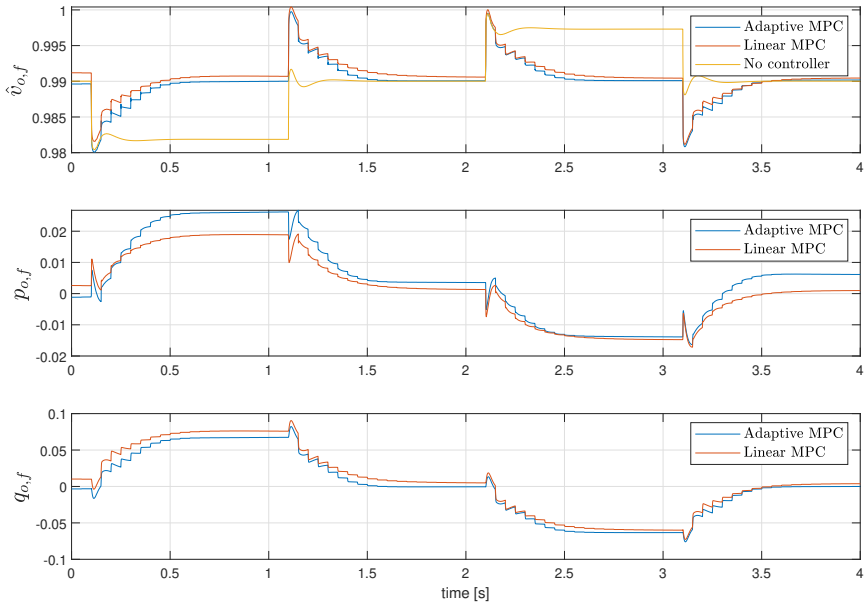

Figure 6.2: Voltage reference tracking with $T_s = 50$ milliseconds in a strong grid.

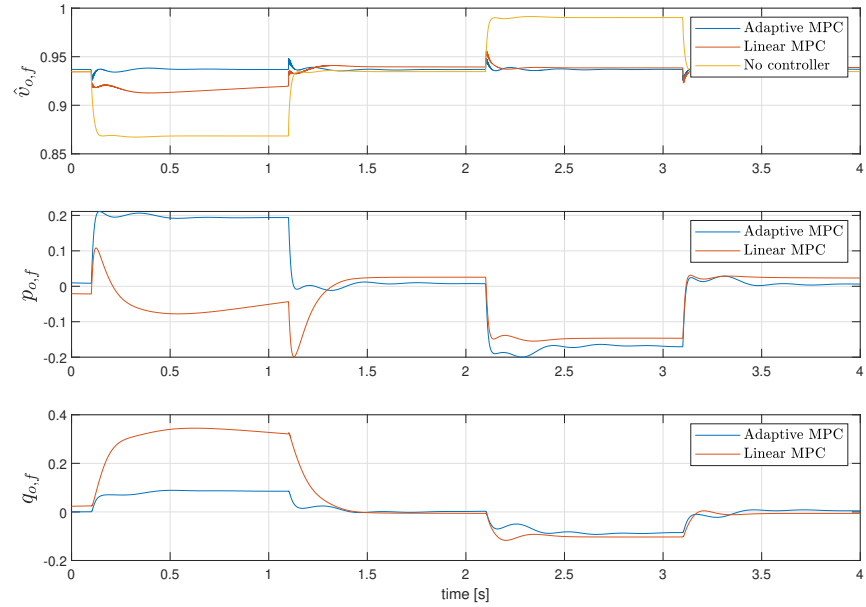

Figure 6.3: Voltage reference tracking with $T_s = 1$ millisecond in a weak grid.

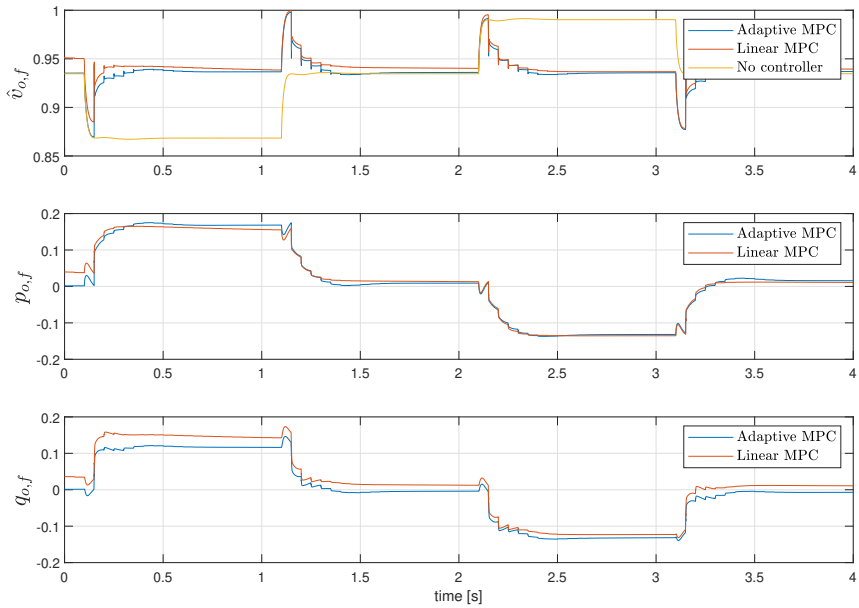

Figure 6.4: Voltage reference tracking with $T_s = 50$ milliseconds in a weak grid.

6.3 Test case 2: Energy Optimization

The second test case is to see how to optimally minimize the power output from the BESS. Three different scenarios explained in section 2.5.2 are simulated: Reactive power control, active power control and combined power control. In all three scenarios, the voltage requirements set by FoL in table 2.2 should be maintained. As these requirements are set as thresholds, a satisfactory result is that the voltage levels are kept within these. Energy optimization without any form of voltage control except for constraints on the minimum and maximum level can be used where there is no exact voltage level required. In theory, the controller will always try to not inject or draw power from the grid unless the limits are violated. Drawbacks to this are discussed in section 7.2.2

Test case 2 is simulated using the weak grid, as the strong grid is not affected to a large degree by power injection. This is explained in section 2.5.2 and discussed more in section 7.2.2. The parameters for the grid in appendix A.4 were used. The calculated Thevenin impedance of the grid (before any load change) is $z_{th} = 0.213 + j0.196$. The calculated Thevenin voltage is $v_{th} = 0.924$. The linearized MPC is linearized at a current reference of zero and the Thevenin voltage.

The weighting matrix $\boldsymbol{Q}_{15-18}$ changes for the control method and is given in each section. The reference target $\boldsymbol{r}_{14-18}$ is given as

$$\boldsymbol{r}_{14-18} = \begin{bmatrix} 0 & 0 & 0 & 0 \end{bmatrix}. \tag{6.4}$$

The objective of the MPC is energy optimization. This gives a reference target for active and reactive power as zero. There is no weight on the voltage control, meaning that the voltage reference is ignored and set to zero.

6.3.1 Reactive Power Control

For reactive power control, the weight of active power injection is set high to penalize active power. The d-axis current reference $i^*_{cv,d}$ is not changed, to not restrict feasible solutions. The weighting matrix $\boldsymbol{Q}_{15-18}$ is defined as

$$\boldsymbol{Q}_{15-18} = \begin{bmatrix} 100 & 1 & 0 & 0 \end{bmatrix}. \tag{6.5}$$

The simulations for the fast controller using a time step of 1 millisecond are shown in figure 6.5. The simulations using the controller with a time step of 50 milliseconds are shown in figure 6.6.

In figure 6.5, there are large instabilities with pure reactive power control for the adaptive MPC. A Simulation with larger weights on the input rates $R_{\Delta u}$ have been simulated to see the influence this has on the controller. In figure 6.7 the weights on $\Delta i_{cv,q}$ have been set to 5 and 10. This results in a more stable controller.

With a stable controller, the reactive power control is able to keep the voltage in the grid above the constraint of 0.92 in table 5.1. The slower controller in figure 6.6 shows characteristics of the same instability as the faster controller.

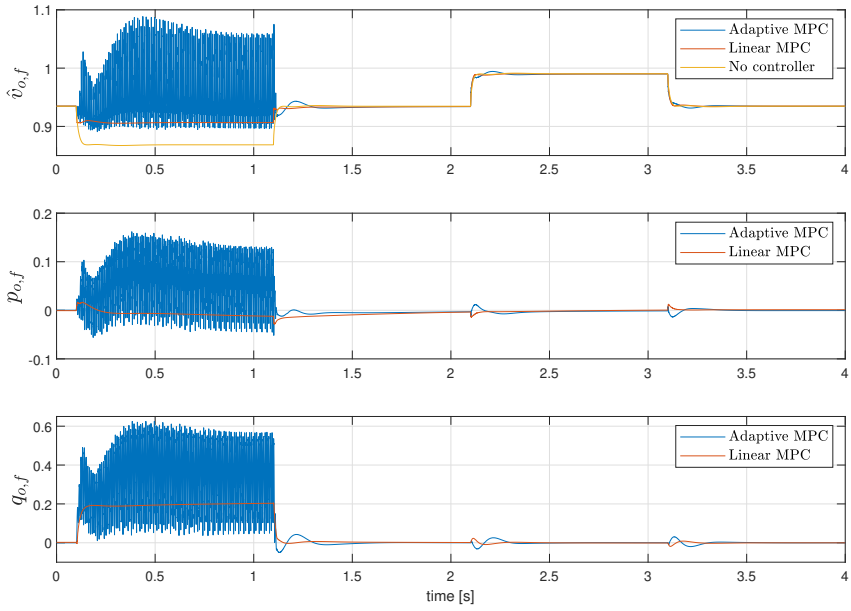

Figure 6.5: Reactive power control with $T_s = 1$ millisecond in a weak grid.

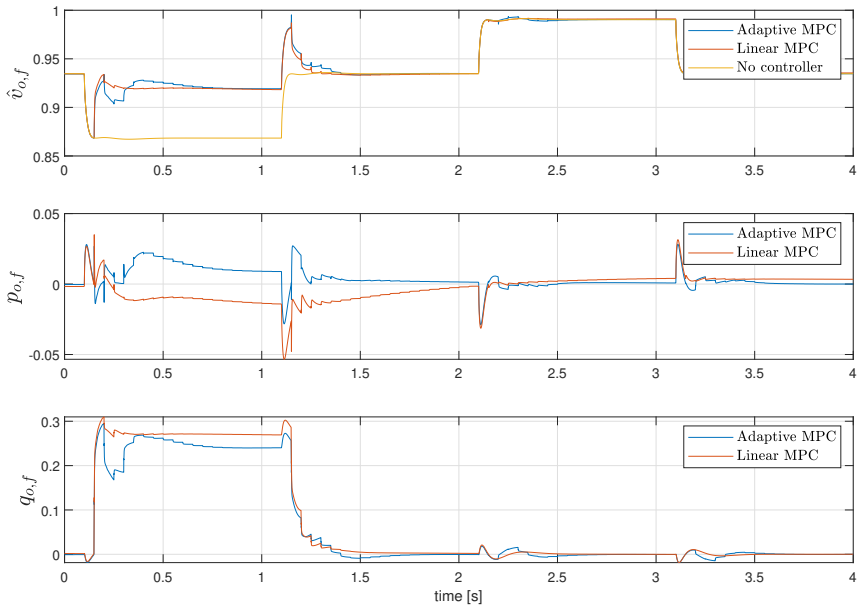

Figure 6.6: Reactive power control with $T_s = 50$ milliseconds in a weak grid.

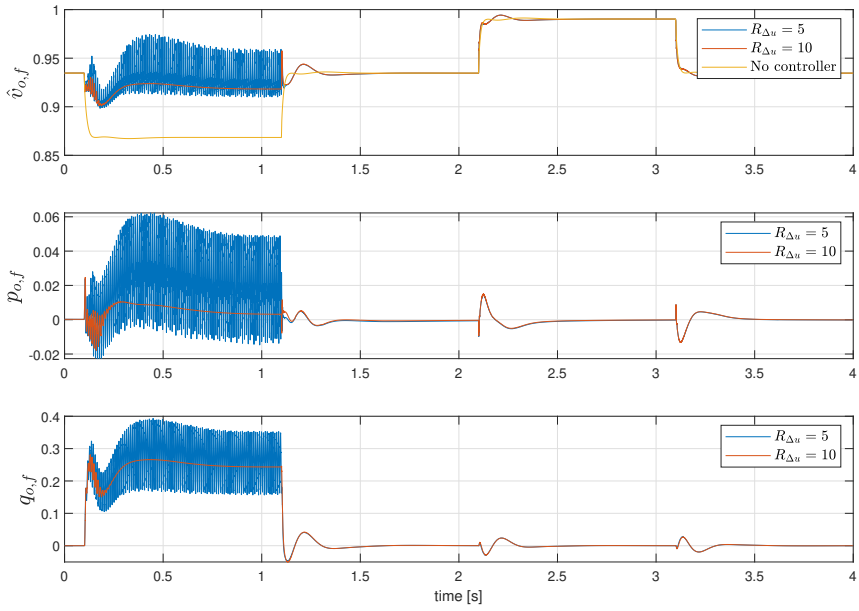

Figure 6.7: Reactive power control with adaptive MPC with $T_s = 1$ millisecond in a weak grid with penalty weights on $\Delta i^*_{cv,q}$

6.3.2 Active Power Control

For active power control, the weight on reactive power is set high, to penalize reactive power. The constraint on the q-axis current reference $i^*_{cv,q}$ is not changed, to not restrict feasible solutions. The weighting matrix $\boldsymbol{Q}_{15-18}$ is defined as

$$\boldsymbol{Q}_{15-18} = \begin{bmatrix} 1 & 100 & 0 & 0 \end{bmatrix}. \tag{6.6}$$

The simulations for the fast controller using a time step of 1 millisecond are shown in figure 6.8. The simulations using the controller with a time step of 50 milliseconds are shown in figure 6.9. The adaptive MPC with active power control is able to keep the voltage above the minimum constraints in table 5.1. The model is more stable than the reactive power control and quickly stabilizes the voltage level.

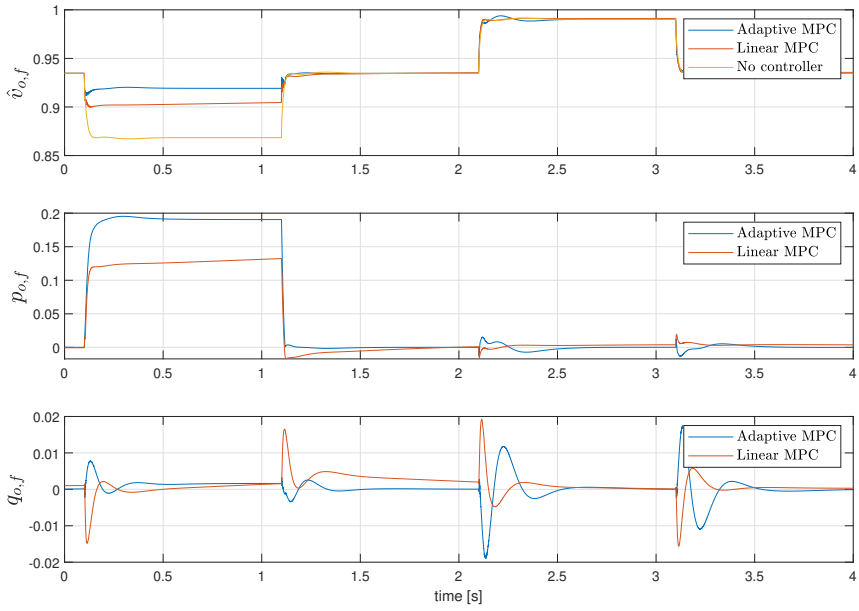

Figure 6.8: Active power control with $T_s = 1$ millisecond in a weak grid.

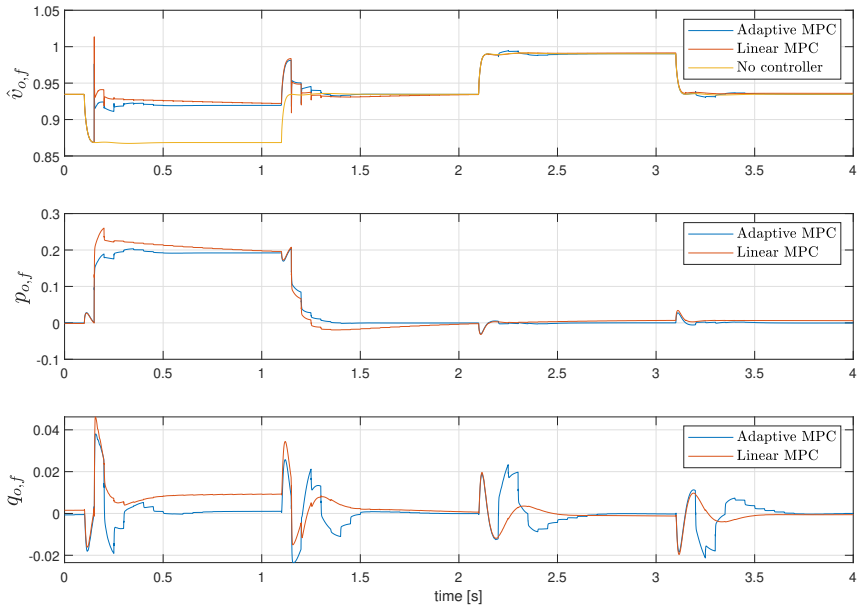

Figure 6.9: Active power control with $T_s = 50$ milliseconds in a weak grid.

6.3.3 Combined Power Control

For combined power control, the weights on active and reactive power can be set in multiple ways. here the weighting matrix $\boldsymbol{Q}_{15-18}$ is defined as

$$\boldsymbol{Q}_{15-18} = \begin{bmatrix} 1 & .2 & 0 & 0 \end{bmatrix} \tag{6.7}$$

where it can be seen that the active power is penalized 5 times more than the reactive power. The reactive power is penalized less because of the advantage using reactive power has, as discussed in section 2.5.2.

The simulations for the fast controller using a time step of 1 millisecond are shown in figure 6.10. The simulations using the controller with a time step of 50 milliseconds are shown in figure 6.11. Both controllers are able to prioritze reactive power injection in the grid, where the adaptive MPC only uses about 0.06 pu active power compared to 0.2 pu reactive power.

The adaptive MPC with combined power control is more oscillating than with active power control, but reaches steady-state at the minimum voltage constraints in table 5.1.

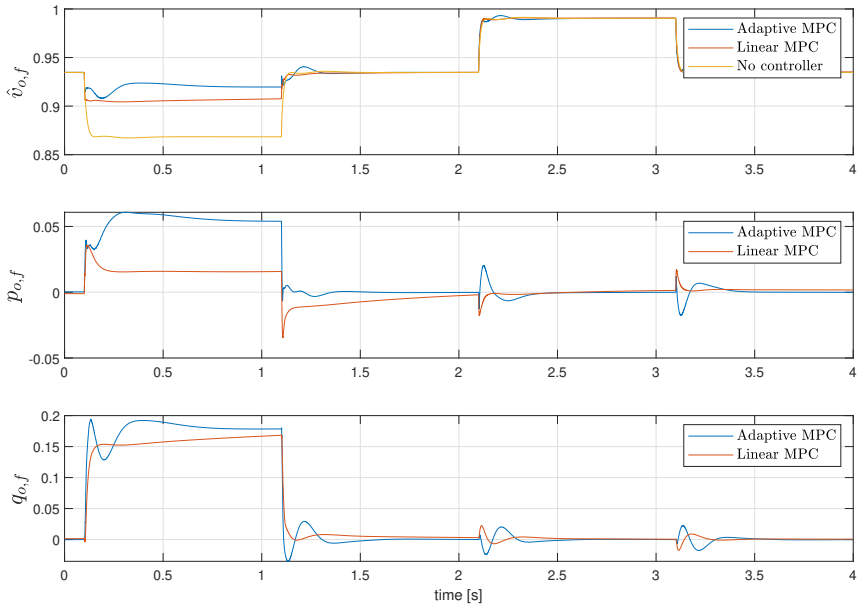

Figure 6.10: Combined power control with $T_s = 1$ millisecond in a weak grid.

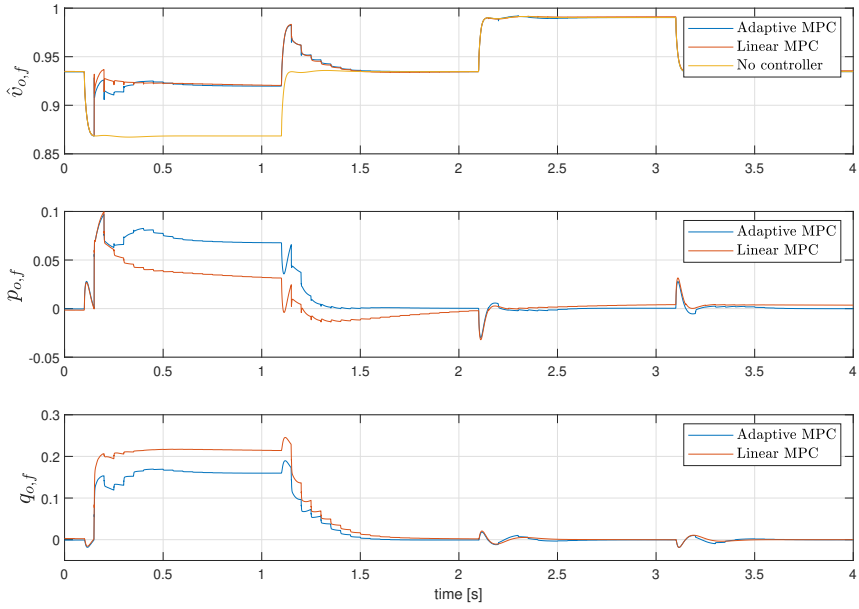

Figure 6.11: Combined power control with $T_s = 50$ milliseconds in a weak grid.

6.4 Test case 3: Combined Reference Tracking and Energy Optimization

In test cases one and two there was either voltage control or energy optimization. In test case three these two are combined to investigate if this gives better control of the voltage levels while still injecting power optimally. As in test case two, a satisfactory result is voltage levels within the requirements set by FoL[27]

Test case 3 is simulated using two different weak grids, as the strong grid is not affected to a large degree by power injection. Two grids with different line resistances are used to simulate the distance between nodes. They are simulated to see if the ratio of injected active power changes when there is a lower X/R ratio, and higher total impedance in the grid.

The parameters for the weak grid in appendix A.4 were used. The calculated Thevenin impedance of the grid (before any load change) is $z_{th} = 0.213 + j0.196$. The calculated Thevenin voltage is $v_{th} = 0.924$. The reference value of the voltage in equation (6.9) was set according to the steady-state value solved using *fsolve* in Matlab before run time. The linearized MPC is linearized at a current reference of zero and the Thevenin voltage. The weighting matrix was set as in equation (6.8).

A second resistive weak grid with a higher resistance in the line impedance was also simulated. The line impedance of the grid is listed in table A.4.11. The calculated Thevenin equivalents are $z_{th} = 0.353 + j0.175$ and $v_{th} = 0.883$. The reference targets and weighting penalties are set the same as the for the weak grid in equation (6.9) and equation (6.8). The voltage reference is set above the calculated steady-state voltage of 0.89 because this is lower than the constraints given by the MPC.

The weighting matrix $\boldsymbol{Q}_{15-18}$ and reference target $\boldsymbol{r}_{14-18}$ is given as

$$\boldsymbol{Q}_{15-18} = \begin{bmatrix} 1 & .2 & 50 & 0 \end{bmatrix} \tag{6.8}$$

$$\boldsymbol{r}_{14-18} = \begin{bmatrix} 0 & 0 & 0.937 & 0 \end{bmatrix}. \tag{6.9}$$

The weight on the voltage is set high because the voltage only operates on the pu values of 0.9 to 1.1, while the power measurements work from -1 to 1. A voltage deviation of 0.01 pu is penalized equally to an active power output of 0.5 pu. Lowering the voltage weight leads to a high deviation from the reference target.

The simulations for the fast controller in the weak grid using a time step of 1 millisecond are shown in figure 6.12. The simulations using the controller in the weak with a time step of 50 milliseconds are shown in figure 6.13.

The simulations for the controller in the resistive weak grid using a time step of 1 millisecond are shown in figure 6.14. The simulations of the controller with a time step of 50 milliseconds in the resistive weak grid are shown in figure 6.15.

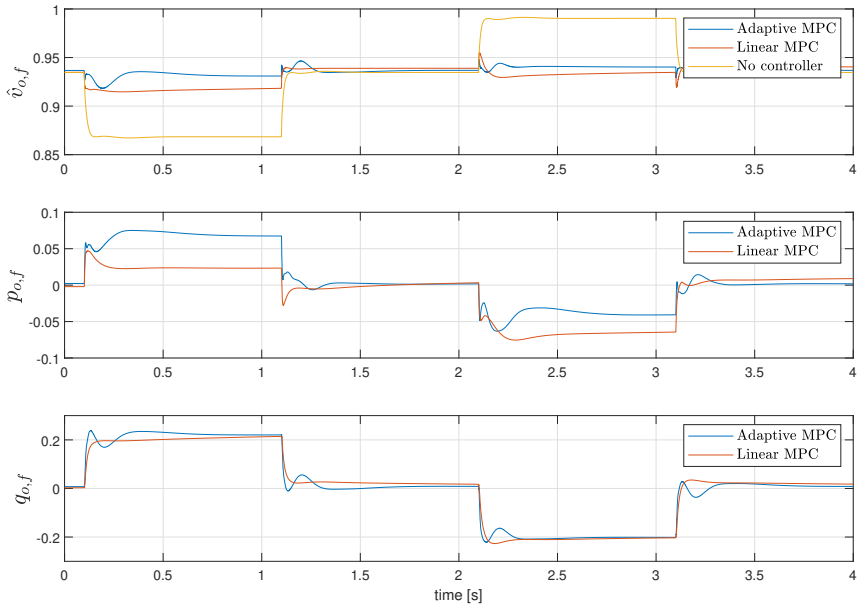

Figure 6.12: Combined power and voltage control with $T_s = 1$ millisecond in a weak grid.

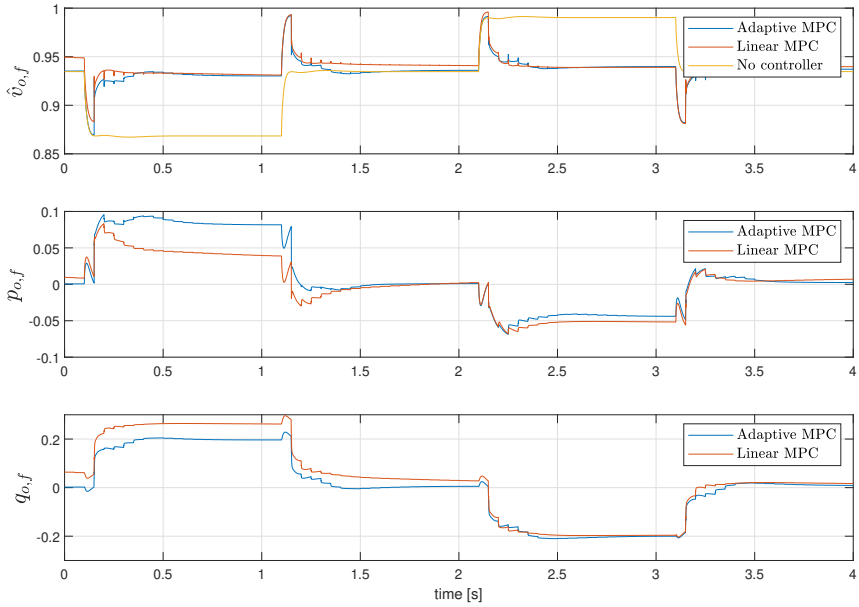

Figure 6.13: Combined power and voltage control with $T_s = 50$ milliseconds in a weak grid.

It can be seen that the voltage drop is higher in the resistive weak grid than for the weak grid in figure 6.12. With the same load demand, the increased resistance increases the voltage drop along the lines. The response from the MPC is similar to the weak grid, with only higher amplitudes of the power injected.

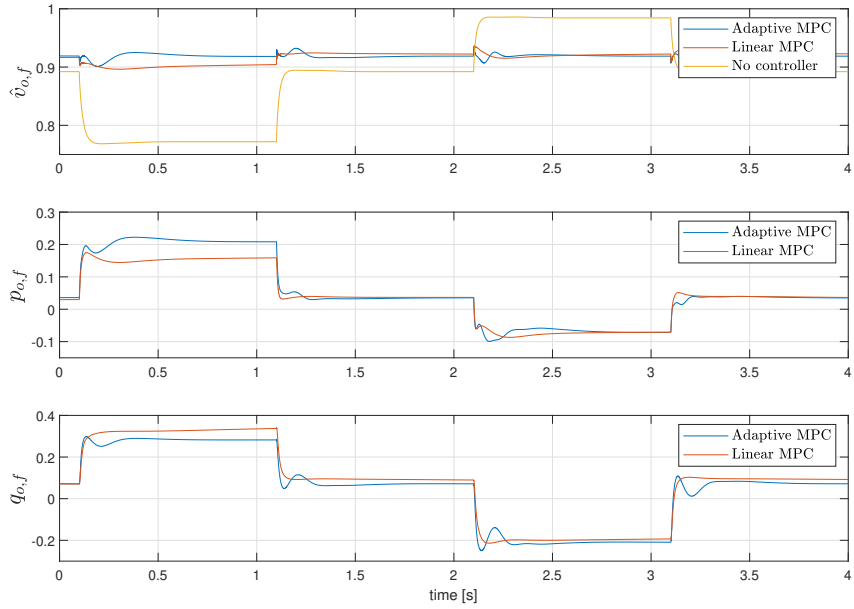

Figure 6.14: Combined power and voltage control with $T_s = 1$ millisecond in a resistive weak grid

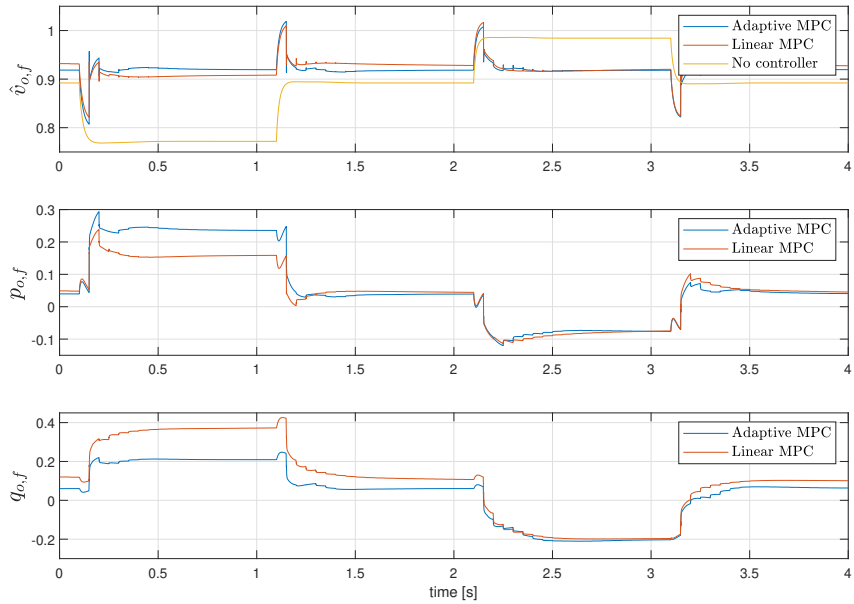

Figure 6.15: Combined power and voltage control with $T_s = 50$ milliseconds in a resistive weak grid.

7

Discussion

This chapter presents a discussion around the modelling and the results of the simulations. A discussion of the challenges related to model design is presented. A general discussion around the simulation results from the test cases is presented, as well as discussions for each test case.

7.1 Design of VSC and MPC

Modelling the VSC in figure 3.1 using a nonlinear state space representation allows for accurate analysis of the model. The model was linearized to verify its operation around an equilibrium point, and the response of the model was investigated in chapter 4. Doing this allows challenging grid parameters or edge cases to be discovered and dealt with. The linear model shows stability in all realistic grid parameters, and the model is therefore easy to work with.

The MPC designed in chapter 5 gives wide freedom in the control objective. Depending on the application for the VSC, the objective function of the MPC can be changed. This is done without changing the foundational MPC implementation of the model or constraints.

A challenge in implementing a MPC using a state space representation of the VSC is the nonlinear modelling. Any change in the VSC layout must be modelled, and the MPC must be redesigned. In section 7.2, an implementation of droop control is discussed. This would require a remodelling of the VSC and the MPC.

7.2 Simulations

The results of all three test cases had some similarities that can be discussed together. These similarities relate to the linearization of the model and the time step used in the

MPC. There are also some response similarities between the simulations that will be discussed here. These topics will not be discussed in depth in the sections for each test case.

A model characteristic seen in all MPC implementations using $T_s = 50$ milliseconds is that a voltage change influences the power injection from the VSC. This characteristic is shown in figure 3.2. An example of this with the MPC is seen in figure 6.13 where there is an increase in the active power injected into the grid when the voltage drops. There is a similar injection of reactive power from the VSC, but in the negative direction. This property of the model is not caused by the MPC, but is an inherent dynamic of the model used. During large voltage disturbances, there is an initial change in the *dq*-axis currents from the VSC. This occurs when there is no change in the *dq*-current reference during the voltage change. In figure 6.12 it can be seen that this characteristic is not seen in the faster MPC with $T_s = 1$ millisecond. This dynamic goes away when the current references are changed, and the injected power then starts following the values from the current references. The active power is proportional to the d-axis current and the reactive power is negatively proportional to the q-axis current.

The linear MPC is generally not able to follow the reference target as well as the adaptive MPC. As shown in figure 4.8, the linear model has an offset in the *d*-axis voltage when linearized away from the operating point. The same offset in the linear MPC can be seen in figures 6.1, 6.3, 6.8 and 6.10. As shown in figures 6.1 and 6.3, the linear MPC is not able to follow a reference target without an offset. Figures 6.8 and 6.10 shows that the linear MPC is also unable to properly adhere to the voltage constraint set in table 5.1. Figure 6.8 shows that the adaptive MPC controls the voltage to a value of 0.92 pu, while the linear MPC dips below and does not correct itself. The linear MPC perform worse during a disturbance that creates a dip in the voltage, compared to an increase in the voltage. Figure 6.4 shows that the steady-state offset is larger when the VSC injects power into the grid, and smaller when it draws power from it. At 0.1 seconds the voltage drops and the controller is not able to maintain the reference target of 0.94. When the voltage rises at 2.1 seconds, the linear MPC is able to follow the reference target closer.

The adaptive MPC is able to follow the voltage reference target closely. The steady-state voltage is similar for the controllers using $T_s = 1$ millisecond or $T_s = 50$ milliseconds. Comparing the steady-state values in figures 6.3 and 6.4 it can be seen that there is a difference in the transient of the voltage response, but the steady-state voltage is the same.

The adaptive MPC with a $T_s = 1$ millisecond can display some unwanted dynamics during the transient periods of the disturbance. Figure 6.12 show how the voltage amplitude starts dipping due to the disturbance, making the controller respond. The voltage levels rises, but start going down again. This characteristic of having one cycle of oscillations during a disturbance can also be seen in figures 6.1 and 6.10. It is noted that this dynamic is not as prevalent when the reactive power injected into the grid is limited, as in figure 6.8. The oscillations also have less amplitude when the reactive power injection oscillates less. This is shown in figure 6.3. This dynamic in the adaptive MPC can be explained in section 5.1.1. The operating point where the model is linearized around is not necessarily an equilibrium point, creating some dynamics in the linear model that do not exist in the physical model. The slower adaptive MPC does not display these dynamic characteristics. As seen in

figure 6.2, the adaptive MPC does not oscillate, but slowly increases the power injection to the grid until the voltage reaches the reference target.

Figures 6.12 and 6.13 shows the difference between using a time step of 1 millisecond and 50 milliseconds in the MPC. The output calculated by the MPC is not affected until the MPC runs. This creates a delay in the response time, which can be seen in the plots. For the faster adaptive MPC in figure 6.12, the voltage amplitude dips shortly, before back up to the reference target. The slower MPC in figure 6.13 does not respond until after the voltage has dipped to around 0.87 pu. This means that the requirement set by FoL is violated. This violation will happen for all disturbances that cause the voltage to drop below 0.9 pu. With the model implemented in this thesis, this is unavoidable for disturbances that lead to voltage dips faster than the sample time of the MPC. The MPC needs to calculate new manipulated variables faster than the incoming disturbances to stay inside the thresholds set by the constraints. For an implementation of the slower MPC this should be looked into. One method that can be implemented is droop control for voltage regulation presented in section 3.3.2. This would allow the inner loop controller to regulate the voltage and have the MPC calculate the optimal ratio of active and reactive power injection.

Comparing the results using the fast and slow MPC in figures 6.12 and 6.13, it can be seen that the voltage characteristics are a direct cause of the injected power. A smooth power injection from the fast controller results in a smooth voltage amplitude. A more staggered power injection from the slower controller results in a voltage amplitude that has small dips at each control interval. These dips are not wanted, and must be looked further into for an implementation of the slower MPC. Possible ways of resolving the dips are through low pass filtering of the current references of the VSC. This does not affect the response time, but can help with smoothing out the current references.

In figures 6.3 and 6.4 it can be seen that the voltage dip in the weak grid is around 0.07 pu for a load demand of 5kW. The voltage swell is around 0.06 pu for a negative load demand of 5kW. This means that for the simulated weak grid, a 5kW load change results in a voltage change that is 30-35% of the upper and lower voltage level. This is a significant part of the allowable area of the electrical grid.

7.2.1 Test case 1: Output Reference Tracking

Test case 1 was performed to validate that the linear and adaptive MPC operated as intended. Controlling the VSC to follow a specific reference value for the voltage amplitude is not necessarily the most useful real-world application. It is however a good way of validating the performance of the controller.

Strong Grid

As discussed in section 2.3, the voltage is relatively insensitive to load changes in a strong grid. Comparing the strong grid in figures 6.2 and 6.3 to the weak grid in figures 6.3 and 6.4, the voltage change is six to seven times lower in the strong grid than in the weak grid with a load change of 5kW.

Figure 6.1 shows the MPC solving the optimization problem every 1 millisecond. Both the adaptive and linear MPC quickly responds to the voltage disturbance. It can be seen that the adaptive MPC has a quicker response, but experiences one more cycle of oscillations compared to the linear MPC. The response from the linear MPC is quick, with a more desired response in the voltage amplitude. The power injection of the linear and adaptive MPC are quite different. This is expected as there are no weights penalizing these outputs, and the disturbance moves the linear model away from its linearization point. The response of both models is similar to positive and negative load demands. This means that the VSC is able to also absorb power from the grid into the battery during charging.

Figure 6.2 shows the simulation of the MPC solving the optimization problem every 50 milliseconds. The slower controller is not as aggressive with the power injection compared to the quicker controller in figure 6.1. This leads to a more gradual approach to the voltage reference target. The response of the adaptive MPC is no longer oscillating due to the linearization point updating at inconvenient times as discussed in section 5.1.1.

Weak Grid

Figure 6.1 shows the MPC with a time step of 1 millisecond. It can be seen that the adaptive MPC has a similar response in the weak grid as in the strong grid in figure 6.1. The linear MPC has a large offset during the load demand. It goes below the lower limit of 0.92 set for the voltage amplitude in table 5.1. During the negative load period, it responds similarly to the strong grid.

Figure 6.4 shows the MPC simulated with a time step of 50 milliseconds. In the weak grid, both the linear and the adaptive MPC dips below the requirement set by FoL of 0.9 pu voltage. With the disturbance profile given as it is, this is unavoidable with this time step, as the controllers do not respond in time. Both the adaptive and linear MPCs respond similarly and have similar solutions to the optimization problem as can be seen by the power injections.

Both the faster and slower MPC using the adaptive method are successful in following the voltage reference. As explained in the introduction of this case, voltage tracking is not the most useful application for a BESS. However, these simulations show that voltage tracking can be used to lift the voltage above the minimum constraint set in the MPC. Thus allowing the VSC to operate above the limit and not at it.

7.2.2 Test case 2: Energy Optimization

Controlling the VSC using energy optimization is done to minimize the usage of the BESS. The VSC will only start power flowing in or out of the grid if the voltage levels are outside the constraints set in table 5.1. Reactive and active power control was simulated to validate the performance of single output control.

Reactive Power Control

Figure 6.5 shows the simulation using the MPC with a time step of 1 millisecond. The results show that the adaptive model is not able to find a stable solution during the initial

load demand only injecting reactive power. Increasing the prediction horizon p to longer than 10 did not change the results of the simulation. The linear MPC does not have this instability.

The instability in the adaptive MPC can be improved by limiting the rate of change for the q-axis current. By increasing the weight on $\Delta i_{cv,q}$ it is closer to stable. The reason for this instability is unclear, but possibly has to do with the oscillating nature of injecting reactive power into the grid as discussed in the general discussion.

Active Power Control

Figure 6.8 shows the simulation using the MPC with a time step of 1 millisecond. The reactive power injection is kept to a minimum, except for some deviations during the transient of the disturbance. The adaptive MPC is able to quickly respond to the voltage disturbance and only dips below the voltage constraint of 0.92 pu for a short moment. The linearized MPC has an offset from the constraint of nearly 0.2 pu, and is below the constraint during the entire period the lead demand is 5kW. This offset is potentially caused by a difference in the operating point and the linearization point. Both the faster and slower adaptive MPC in figures 6.8 and 6.9 has oscillating reactive power injection during the disturbance. The q-axis current reference in the VSC is not restricted during active power control. This means that the MPC will try to optimize its usage with the given penalty weights in equation (6.5). Given the scenario that no reactive power should be drawn from the VSC, the current reference must be set to zero. It is not enough to put large penalty weights on the reactive power output.

Combined Power Control

Figures 6.10 and 6.11 shows the results of combing active and reactive power to keep the voltage within the constraints of the MPC. The weighting matrix for the power injection is shown in equation (6.7), where the penalty for using active power is 5 times larger than the penalty for using reactive power. The exact penalty weights chosen must be considered before the implementation of a controller. these will depend on grid parameters, energy storage capacity and VSC rating. In figure 6.10 the fast MPC is shown. It can be seen that the adaptive MPC is able to stay above the minimum constraint given for the voltage amplitude of 0.92 pu. It is able to do this by injecting less active power than active power control shown in figure 6.8 and instead injecting reactive power. The linear combined power controller displays the same problems as discussed previously, it stays below the minimum constraints due to its linearization point. At 2.1 seconds in the simulation, the voltage rises due to the decrease in load demand. The controllers do not inject any power into the grid, as there is no violation of the constraints.

The lack of power injection whenever the voltage stays within the constraints of the MPC shown in table 5.1 is an inherent characteristic of the energy optimization method. The voltage will go up and down freely without any response from the VSC as long as the voltage stays within the requirements. If the constraints are set equal to the FoL requirements at 0.9 pu to 1.1 pu for the voltage levels, the controller will not not respond if the voltage is at 0.9 pu. This can create a problem if another disturbance occurs and the voltage drops

below 0.9 pu. The controller can not respond in time and the voltage levels are below the requirements set for a significant period before stabilizing at 0.9 pu. There is no margin of error where the controller can catch up if there is a disturbance without going below the constraints. The option simulated here, is to set the constraints at a more strict value compared to the requirements in FoL. The MPC has a minimum voltage constraint of 0.92. This allows the controller to have a margin of error whenever a disturbance occurs. This margin of error can be adjusted according to grid parameters or local demands. Weak grids, or locations where sudden large loads can occur need a smaller range of constraints in the voltage. This can make the BESS work more, lowering the life span and requiring a larger energy storage capacity.

7.2.3 Test case 3: Combined Reference Tracking and Energy Optimization

Weak Grid

Figures 6.12 and 6.13 shows simulation in the weak grid using a combination of reference tracking and energy optimization. By combining these it is possible to avoid staying at the constraints at all times during a disturbance that would normally move the voltage outside the constraints.

By comparing the combined reference and energy optimization in figure 6.12 to energy optimization in figure 6.10, some differences can be seen. The energy optimization method stays at the minimum constraint of 0.92 pu voltage. The combined method follows the reference of 0.937 pu given in equation (6.9). It is able to follow this reference by injecting a similar ratio of power into the grid. The absolute values of the powers injected are higher for test case 3, as is expected when increasing the voltage to a higher value. This shows that the calculated optimal ratio of active and reactive power injected into the grid is the same for both test case 3 in section 7.2.3 and test case 2 with combined power control in section 7.2.2. As long as the weights on power output have the same ratio for both methods, the only difference is the voltage level the system stays at.

Comparing the difference between test case 3 in figure 6.13 and test case 1 for the weak grid in figure 6.4 the advantage of penalizing the power output can be seen. Both are able to maintain the same voltage amplitude after the disturbance, but the combined controller does this while using less active power injection. Test case 1 injects 0.18 pu active power and 0.11 pu reactive power. Test case 3 is able to only inject 0.08 pu active power and 0.2 pu reactive power to maintain the same voltage level.

These two comparisons show the advantage of using a combination of both methods. It gives you the best of both worlds, while not having any drawbacks in the implementation. If no reference tracking is necessary it is possible to lower the penalty weight for the voltage. And similar for the power injection weights.

As mentioned in section 3.6, it is possible to continuously estimate Thevenin equivalents of the grid, thereby calculating where the steady-state of the grid is without any injection of power from the BESS. This allows the MPC to minimize the usage of the BESS to moments when the voltage is outside this equivalent.

Resistive Weak Grid

The resistive weak grid in figure 6.14 shows that the voltage dip without any response from a controller is large. The voltage dips from 0.89 pu to around 0.77 pu with a load change of 5kW. The adaptive MPC for both the fast and slower controller in figures 6.14 and 6.15 are able to keep the voltage above the constraint of 0.92 pu at steady-state. They are not able to keep the voltage at the reference value of 0.937 given in equation (6.9). This has to do with not penalizing the voltage enough compared to the active and reactive power. There is also no integral action in the MPC that could minimize this error over time.

Similar to the previous implementations of the linear MPC, there is an offset in the steady-state value, It is not able to keep the voltage above the voltage constraint of 0.92 pu.

Comparing the weak grid MPC in figure 6.12 and in the resistive weak grid in figure 6.14, it can be seen that the adaptive MPC injects three times the amount of active power into the resistive weak grid compared to the weak grid. While the active power injection is only increased by 1.5 times. This shows how the resistive grid requires more active power injected to maintain the voltage levels, even when the MPC penalizes active power more than reactive power.

8

Conclusion and Future Work

This chapter presents the conclusion of this thesis. A conclusion for the modelling and simulation of the voltage source converter (VSC) using model predictive control (MPC) is presented. Lastly, some possible topics for future work based on the knowledge gained in this thesis are discussed.

8.1 Conclusion

The 2L-VSC utilized in a BESS provide good opportunities for voltage support in the distribution grid. By modelling a state space representation of the VSC, more advanced control algorithms can be implemented. The MPC presented is able to optimally calculate the ratio of injected active and reactive to the grid during a disturbance in the voltage.

The adaptive MPC shows promising results with a time step of 1 millisecond, but has characteristics of instability or an oscillating voltage during the transient period of the response. The slower adaptive MPC with a time step of 50 milliseconds do not show these instability characteristics and is able to find an optimal power injection by the VSC. The slower response time of the controller makes it unsuitable for faster disturbance rejection applications.

The linear MPC has good transient responses when operating close to the linearization point, but has larger steady-state offsets away from the linearization points. The control characteristics are also not as predictable away from the linearization point compared to the adaptive MPC, which makes it unreliable.

The MPC with an objective function of voltage tracking is able to follow a voltage reference. It does this without solving for the optimal power injection, making it less ideal for voltage support with a BESS. The objective function of energy optimization using combined control of the reactive and active power is successful in calculating the optimal power injection. The disadvantage of the controller is that it does not increase the voltage

above the constraints set by the MPC. This can create problems during a disturbance when the voltage is already close to the lower limit.

The proposed MPC model with combined voltage tracking and energy optimization is able to both follow a voltage reference and calculate the optimal power injection to do so. The MPC successfully uses the grid parameters to inject the optimal power into the grid for voltage support. This proposed method achieves the best results of the three methods proposed in this thesis. By choosing appropriate MPC parameters, it is able to do both voltage tracking and energy optimization using the same MPC.

8.2 Future Work

The knowledge gained during this thesis has presented possible topics that are worth researching further. These are related to the model and real-time implementation of the controllers. Here are some suggestions for future work that can be looked into.

Develop Thevenin Estimation

The accuracy of the model is dependent on the estimated Thevenin equivalents of the grid. These can be continuously estimated using methods such as least squares fitting methods[66, 68] or through optimization methods[69, 70]. An implementation of voltage support requires continuous estimation of the Thevenin equivalents.

Real-time Computational Complexity

The time steps used in this thesis show that a faster controller can respond to disturbances faster than a slower controller. Investigate a realistic time step for the MPC to operate at. The application of the MPC heavily depends on the minimum sampling time the controller can solve the optimization problem implemented in this thesis.

Controller Between MPC and Inner Loop Current Controller

For the longer time step MPC, the response time of the controller is lacking. An inner controller VSC that can detect changes in the voltage and respond to quick-acting disturbances can improve this. The MPC can have a supervisory role in deciding the voltage reference and active-to-reactive power ratio injected, while an inner controller detects sudden voltage changes. This will require a remodelling of the inner loop current controller model of the VSC. The discussed droop control in section 3.3.2 is a good starting point when choosing a voltage support controller.

Predict Future Demand

Incorporate future prediction of the load demand in the parameters of the MPC. Change penalty weights and reference targets for the VSC depending on the predicted future load demand. This can allow for optimal charging of the battery during periods with low load demand.

Multiple BESS

Investigate how multiple BESS located in the same distribution grid affect each other and the stability of the voltage.

Bibliography

[1] (2022, 10) Share of energy consumption from renewable sources in europe (8th eap). https://www.eea.europa.eu/ims/share-of-energy-consumption-from. (Accessed on 06-05-2023).

[2] B. K. Sovacool, J. Kester, L. Noel, and G. Zarazua de Rubens, "Actors, business models, and innovation activity systems for vehicle-to-grid (v2g) technology: A comprehensive review," *Renewable and Sustainable Energy Reviews*, vol. 131, p. 109963, 2020. [Online]. Available: https://www.sciencedirect.com/science/article/pii/S1364032120302549

[3] H. Bråthen. (2023, 03) Fire av fem nye biler i 2022 var elbiler. https://www.ssb.no/transport-og-reiseliv/landtransport/statistikk/bilparken/artikler/fire-av-fem-nye-biler-i-2022-var-elbiler. (Accessed on 06-05-2023).

[4] K. Sand, K. Berg, A. Hammer, and K. Ingebrigtsen. (2020, 11) Veileder for kost/nytte-vurderinger ved integrasjon av batteri i distribusjonsnettet. (Accessed on 21-03-2023). [Online]. Available: https://lede.no/getfile.php/1335589-1612786176/Lede/Dokumenter/Rapport_Veileder%20for%20kostnytte-vurderinger%20ved%20integrasjon%20av%20batteri%20i%20distribusjonsnettet.pdf

[5] B. Bayer, P. Matschoss, H. Thomas, and A. Marian, "The german experience with integrating photovoltaic systems into the low-voltage grids," *Renewable Energy*, vol. 119, pp. 129–141, 2018. [Online]. Available: https://www.sciencedirect.com/science/article/pii/S0960148117311461

[6] ENTSO-E. Static synchronous compensator (statcom) - entso-e. https://www.entsoe.eu/Technopedia/techsheets/static-synchronous-compensator-statcom. (Accessed on 26-06-2023).

[7] D. S. Nikam and V. N. Kalkhambkar, "Statcom and multilevel vsc topology: A review," in *2018 International Conference on Current Trends towards Converging Technologies (ICCTCT)*, 2018, pp. 1–7.

[8] A. Bharadwaj Ch. and S. Maiti, "Modular multilevel statcom with energy storage," in *2016 11th International Conference on Industrial and Information Systems (ICIIS)*, 2016, pp. 730–735.

[9] C. Zhao, P. B. Andersen, C. Træholt, and S. Hashemi, "Grid-connected battery energy storage system: a review on application and integration," *Renewable and Sustainable Energy Reviews*, vol. 182, p. 113400, 2023. [Online]. Available: https://www.sciencedirect.com/science/article/pii/S1364032123002575

[10] Y.-K. Wu and K.-T. Tang, "Frequency support by bess – review and analysis," *Energy Procedia*, vol. 156, pp. 187–191, 2019, 5th International Conference on Power and Energy Systems Engineering (CPESE 2018). [Online]. Available: https://www.sciencedirect.com/science/article/pii/S1876610218310865

[11] L. Xavier, W. Amorim, A. Cupertino, V. Mendes, W. Boaventura, and H. Pereira, "Power converters for battery energy storage systems connected to medium voltage systems: a comprehensive review," *BMC Energy*, vol. 1, 07 2019.

[12] E. Reihani, S. Sepasi, L. R. Roose, and M. Matsuura, "Energy management at the distribution grid using a battery energy storage system (bess)," *International Journal of Electrical Power & Energy Systems*, vol. 77, pp. 337–344, 2016. [Online]. Available: https://www.sciencedirect.com/science/article/pii/S014206151500455X

[13] J.-T. Liao, Y.-S. Chuang, H.-T. Yang, and M.-S. Tsai, "Bess-sizing optimization for solar pv system integration in distribution grid," *IFAC-PapersOnLine*, vol. 51, no. 28, pp. 85–90, 2018, 10th IFAC Symposium on Control of Power and Energy Systems CPES 2018. [Online]. Available: https://www.sciencedirect.com/science/article/pii/S2405896318334013

[14] A. Hammer, K. Ingebrigtsen, K. Berg, R. Nyhavn, and Y. Skålnes. (2020, 07) Prosjektnotat integer. (Accessed on 21-03-2023). [Online]. Available: https://lede.no/getfile.php/1333271-1612788277/Nett/Filer/Prosjekter/Forskning/Tensio%20TN%20-%20Prosjektnotat%20IntegER.pdf

[15] J. Klemets. Bass - electrochemical battery for voltage support in distribution grid - sintef. https://www.sintef.no/en/projects/2021/bass-electrochemical-battery-for-voltage\-support-in-distribution-grid/. (Accessed on 06/05/2023).

[16] V. Wøllo, "Modelling of voltage source converter in battery energy storage system for voltage support in the distribution grid," NTNU, Tech. Rep., 2022.

[17] Smart grid laboratory - sintef. https://www.sintef.no/en/all-laboratories/smartgridlaboratory/. (Accessed on 06-05-2023).

[18] E. Norge. Kraftproduksjon. https://energifaktanorge.no/norsk-energiforsyning/kraftforsyningen/. (Accessed on 27-06-2023).

[19] SSB. Elektrisitet. https://www.ssb.no/energi-og-industri/energi/statistikk/elektrisitet. (Accessed on 27-06-2023).

[20] NVE. (2023, 02) Hvor kommer strømmen fra? (Accessed on 20-03-2023). [Online]. Available: https://www.nve.no/energi/energisystem/kraftproduksjon/hvor-kommer-stroemmen-fra/

[21] Energifakta Norge. (2019, 04) Strømnettet. (Acessed on 06-03-2023). [Online]. Available: https://energifaktanorge.no/norsk-energiforsyning/kraftnett/

[22] SINTEF ENERGY. Planlegginbsgok for kraftnett (planbok). https://www.ren.no/tjenester/planbok. (Accessed on 06-05-2023).

[23] R. E. Torres-Olguin, I. Madshaven, E. B. Mehammer, and J. Klemets, "Prinsipper for kostnadssammenligning av tradisjonell nettinvestering og batterisystem," SINTEF Energy, Tech. Rep., 2022.

[24] NVE. (2018, 07) Veileder til leveringskvalitetsforskriften. https://publikasjoner.nve.no/veileder/2018/veileder2018_07.pdf. (Accessed on 16-05-2023).

[25] M. Jan, Z. Lubosny, J. W. Bialek, and J. R. Bumby, *Power System Dynamics: Stability and Control*. John Wiley & Sons Inc, 2020.

[26] E. F. Fuchs and M. A. Masoum, *Power Quality in Power Systems, Electrical Machines, and Power-Electronic Drives*. ELSEVIER, 2023.

[27] Olje- og energidepartementet. (2020, January) Forskrift om leveringskvalitet i kraftsystemet. [Online]. Available: https://lovdata.no/dokument/SF/forskrift/2004-11-30-1557

[28] (2018) Omfang av henvendelser om leveringskvalitet. https://publikasjoner.nve.no/rapport/2018/rapport2018_39.pdf. (Accessed on 18-05-2023).

[29] NERC. (2017, 12) Integrating inverter-based resources into low short circuit strength systems. https://www.nerc.com/comm/RSTC_Reliability_Guidelines/Item_4a._Integrating_%20_Inverter-Based_Resources_into_Low_Short_Circuit_Strength_Systems_-_2017-11-08-FINAL.pdf. (Accessed on 13-04-2023).

[30] P. Kundur, *Power System Stability and Control*. McGraw-Hill, 1994.

[31] A. Gavrilovic, "Ac/dc system strength as indicated by short circuit ratios," *International Conference on AC and DC Power Transmission*, pp. 27–32, 1991.

[32] B. Vilmann, P. Randewijk, H. Jóhannsson, J. Hjerrild, and A. Khalil, "Frequency and voltage compliance capabilities of grid-forming wind turbines in offshore wind farms in weak ac grids," *Electronics*, vol. 12, p. 1114, 02 2023.

[33] H. Bindner and F. Risø, *Power Control for Wind Turbines in Weak Grids: Concepts Development*, ser. Risø-R. Forskningscenter Risø, 1999. [Online]. Available: https://books.google.no/books?id=Y5UdzwEACAAJ

[34] CIGRE, "Connection of wind farms to weak ac networks," CIGRE, Technical Report 671, 2016.

[35] ——, "Guide for planning dc links terminating at ac locations having low short-circuit capacities. part 1. ac/dc interaction phenomena." CIGRE, Technical Report 68, 1992.

[36] A. Etxegarai, P. Eguia, E. Torres, and E. Fernandez, "Impact of wind power in isolated power systems," *Mediterranean Electrotechnical Conference*, pp. 63–66, 03 2012.

[37] R. Fu, L. Li, X. Wang, and X. Lv, "Critical scr for the stability of vsc connected to weak grid," in *2020 IEEE Power & Energy Society General Meeting (PESGM)*, 2020, pp. 1–5.

[38] G. S. Chawda and A. G. Shaik, "Power quality mitigation in weak ac grid with low x/r ratios using distribution static compensator controlled by lmf algorithm," in *2020 IEEE Region 10 Symposium (TENSYMP)*, 2020, pp. 44–47.

[39] G. Jayasinghe and B. Bahrani, "Stability-enhancing measures for weak grids study - milestone 2 report," Monash University, Tech. Rep., 2021.

[40] P. Kundur, J. Paserba, V. Ajjarapu, G. Andersson, A. Bose, C. Canizares, N. Hatziargyriou, D. Hill, A. Stankovic, C. Taylor, T. Van Cutsem, and V. Vittal, "Definition and classification of power system stability ieee/cigre joint task force on stability terms and definitions," *IEEE Transactions on Power Systems*, vol. 19, no. 3, pp. 1387–1401, 2004.

[41] N. Hatziargyriou, J. Milanovic, C. Rahmann, V. Ajjarapu, C. Canizares, I. Erlich, D. Hill, I. Hiskens, I. Kamwa, B. Pal, P. Pourbeik, J. Sanchez-Gasca, A. Stankovic, T. Van Cutsem, V. Vittal, and C. Vournas, "Definition and classification of power system stability – revisited & extended," *IEEE Transactions on Power Systems*, vol. 36, no. 4, pp. 3271–3281, 2021.

[42] H. Abdi, B. Mohammadi-ivatloo, S. Javadi, A. R. Khodaei, and E. Dehnavi, *Chapter 7 - Energy Storage Systems*, G. Gharehpetian and S. M. Mousavi Agah, Eds. Butterworth-Heinemann, 2017. [Online]. Available: https://www.sciencedirect.com/science/article/pii/B9780128042083000078

[43] (2020, 09) Classification of energy storage technologies: an overview. https://etn.news / energy-storage / classification-of-energy-storage-technologies-an-overview. (Accessed on 06-06-2023).

[44] Z. Yang, J. Zhang, M. C. W. Kintner-Meyer, X. Lu, D. Choi, J. P. Lemmon, and J. Liu, "Electrochemical energy storage for green grid," *Chemical Reviews*, vol. 111, no. 5, pp. 3577–3613, 2011, pMID: 21375330. [Online]. Available: https://doi.org/10.1021/cr100290v

[45] I. Madshaven, E. B. Mehammer, and J. Klemets, "Batteri som nettjeneste," SINTEF Energy, Tech. Rep., 2022.

[46] Lithium-ion battery pack prices rise for first time to an average of $151/kwh — bloombergnef. https : / / about . bnef . com / blog /

lithium-ion-battery-pack-prices-rise-for-first-time-to-an-average-of-151-kwh/. (Accessed on 04-05-2023).

[47] Asian Development Bank. (2018, 12) Handbook on battery energy storage system. http://dx.doi.org/10.22617/TCS189791-2. (Accessed on 04-05-2023).

[48] M. M. Kabir and D. E. Demirocak, "Degradation mechanisms in li-ion batteries: a state-of-the-art review," *International Journal of Energy Research*, vol. 41, no. 14, pp. 1963–1986, 2017. [Online]. Available: https://onlinelibrary.wiley.com/doi/abs/10.1002/er.3762

[49] F. A. Viawan, "Voltage control and voltage stability of power distribution systems in the presence of distributed generation," Ph.D. dissertation, CHALMERS UNIVERSITY OF TECHNOLOGY, 2008.

[50] T. Yunusov, D. Frame, W. Holderbaum, and B. Potter, "The impact of location and type on the performance of low-voltage network connected battery energy storage systems," *Applied Energy*, vol. 165, pp. 202–213, 2016. [Online]. Available: https://www.sciencedirect.com/science/article/pii/S0306261915016189

[51] S. Khunkitti, P. Boonluk, and A. Siritaratiwat, "Optimal location and sizing of bess for performance improvement of distribution systems with high dg penetration," *International Transactions on Electrical Energy Systems*, vol. 2022, pp. 1–16, 06 2022.

[52] L. Gyugyi, "Power electronics in electric utilities: static var compensators," *Proceedings of the IEEE*, vol. 76, no. 4, pp. 483–494, 1988.

[53] S. M. Alizadeh, C. Ozansoy, and T. Alpcan, "The impact of x/r ratio on voltage stability in a distribution network penetrated by wind farms," in *2016 Australasian Universities Power Engineering Conference (AUPEC)*, 2016, pp. 1–6.

[54] S. Matthew, S. Wara Tita, I. Adejumobi, E. Ajisegiri, and A. Olanipekun, "Power system's voltage stability improvement using static var compensator," *International Journal of Emerging Technology and Advanced Engineering*, vol. 4, pp. 494–501, 01 2014.

[55] I. Ranaweera and O.-M. Midtgard, "Centralized control of energy storages for voltage support in low-voltage distribution grids," in *2016 IEEE 16th International Conference on Environment and Electrical Engineering (EEEIC)*, 2016, pp. 1–6.

[56] H. Zhao, Q. Wu, J. Wang, Z. Liu, M. Shahidehpour, and Y. Xue, "Combined active and reactive power control of wind farms based on model predictive control," *IEEE Transactions on Energy Conversion*, vol. 32, no. 3, pp. 1177–1187, 2017.

[57] K. Sharifabadi, L. Harnefors, H.-P. Nee, S. Norrga, and R. Teodorescu, *Design, Control, and Application of Modular Multilevel Converters for HVDC Transmission Systems*. John Wiley & Sons Ltd, 2016.

[58] A. Yazdani and R. Iravani, *Voltage-Sourced Converters in Power Systems: Modeling, Control, and Applications*. John Wiley & Sons Ltd, 2010.

[59] O. Mo, M. Hernes, and K. Ljøkelsøy, "Active damping of oscillations in lc-filter for line connected, current controlled, pwm voltage source converters," SINTEF Energy, Tech. Rep., 2003.

[60] H. Saadat, *Power System Analysis*. PSA Publishing, 2010.

[61] Droop control - matlab & simulink. https://se.mathworks.com/discovery/droop-control.html. (Accessed on 28-06-2023).

[62] R. Moslemi and J. Mohammadpour, "Accurate reactive power control of autonomous microgrids using an adaptive virtual inductance loop," *Electric Power Systems Research*, vol. 129, pp. 142–149, 2015. [Online]. Available: https://www.sciencedirect.com/science/article/pii/S0378779615002308

[63] A. Villa, F. Belloni, R. Chiumeo, and C. Gandolfi, "Conventional and reverse droop control in islanded microgrid: Simulation and experimental test," in *2016 International Symposium on Power Electronics, Electrical Drives, Automation and Motion (SPEEDAM)*, 2016, pp. 288–294.

[64] H. K. Khalil, *Nonlinear Systems*. PEARSON, 2014.

[65] C.-T. Chen, *Linear System Theory and Design*, 3rd ed. Oxford University Press, Inc, 1999.

[66] T. Premgamone, E. Ortjohann, J. Kortenbruck, D. Holtschulte, A. Schmelter, and S. D. Varada, "Thévenin equivalent impedance estimation for power electronic devices in smart grids," in *2022 International Symposium on Power Electronics, Electrical Drives, Automation and Motion (SPEEDAM)*, 2022, pp. 192–199.

[67] C. K. Alexander and M. N. O. sadiku, *Fundamentals of Electric Circuits*, 4th ed. McGraw-Hill, 2009.

[68] S.-J. S. Tsai and K.-H. Wong, "On-line estimation of thevenin equivalent with varying system states," in *2008 IEEE Power and Energy Society General Meeting - Conversion and Delivery of Electrical Energy in the 21st Century*, 2008, pp. 1–7.

[69] H.-Y. Su and T.-Y. Liu, "Robust thevenin equivalent parameter estimation for voltage stability assessment," *IEEE Transactions on Power Systems*, vol. 33, no. 4, pp. 4637–4639, 2018.

[70] S. Shen, D. Lin, H. Wang, P. Hu, K. Jiang, D. Lin, and B. He, "An adaptive protection scheme for distribution systems with dgs based on optimized thevenin equivalent parameters estimation," *IEEE Transactions on Power Delivery*, vol. 32, no. 1, pp. 411–419, 2017.

[71] D. E. Seborg, D. A. Mellichamp, and T. F. Edgar, *Process Dynamics and Control*, 3rd ed., ser. Wylie Series in Chemical Engineering. John Wiley & Sons, 2011. [Online]. Available: http://www.worldcat.org/isbn/9780470646106

[72] B. Foss and T. A. N. Heirung, *Merging Optimization and Control*. NTNU, 03 2016.

[73] J. Nocedal and S. J. Wright, *Numerical Optimization*. Springer Science+Business Media, LLC, 2006.

[74] T. A. Johansen, "Introduction to nonlinear model predictive control and moving horizon estimation - chapter 1," in *Introduction to Nonlinear Model Predictive Control and Moving Horizon Estimation*, 2011.

[75] (2023, 05) Model predictive control toolbox. https://se.mathworks.com/help/mpc/. (Accessed on 20-05-2023).

[76] (2023, 05) Optimization problem - matlab & simulink. https://se.mathworks.com/help/mpc/ug/optimization-problem.html. (Accessed on 20-05-2023).

[77] M. Hovd. (2004, 03) A brief introduction to model predictive control. https://www.itk.ntnu.no/fag/TTK4135/Pensum/MPCkompendium%20HOvd.pdf. (Accessed on 29-05-2023).

Appendix

A Modelling

A.1 Simulink Model

The Simulink model used consist of the grid model in figure A.1.1, the connectinon of the BESS at node 9 in figure A.1.2, the BESS model in figure A.1.3 and the linear and adaptive MPC in figure A.1.4. The Simulink model of the VSC developed at Sintef is not shown.

The simplified Grid model with the Thevenin equivalents is shown in figure A.1.5.

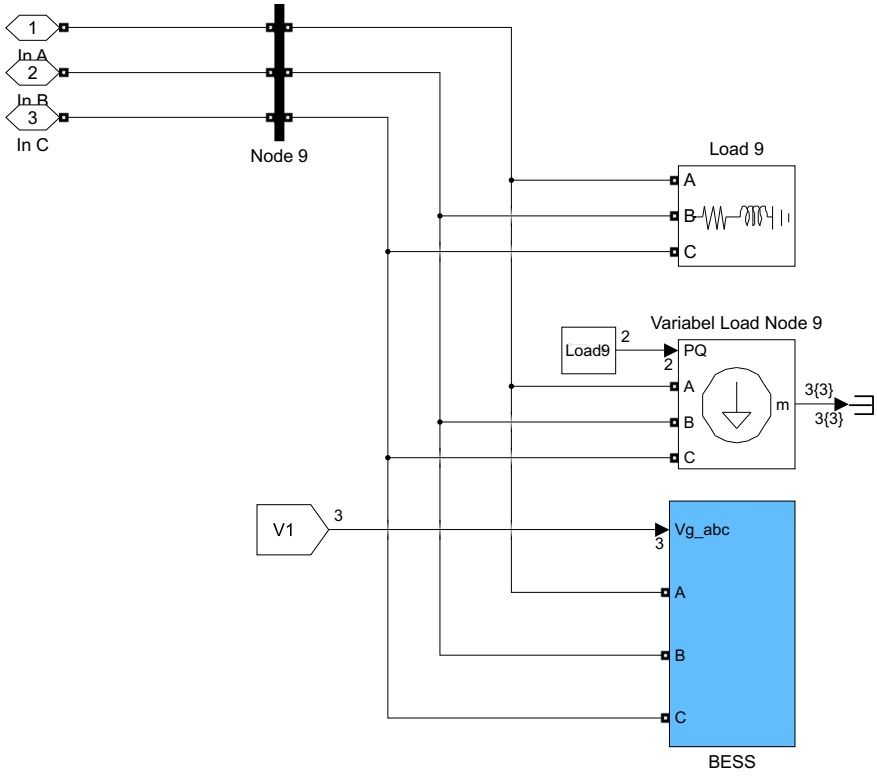

Figure A.1.2: Simulink model. BESS connection at node 9.

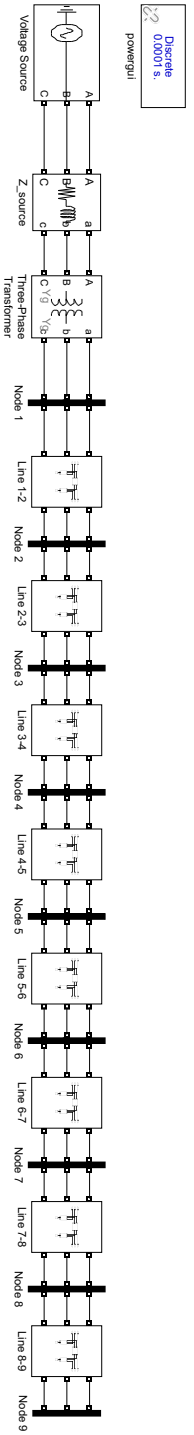

Figure A.1.1: Simulink model. Grid model.

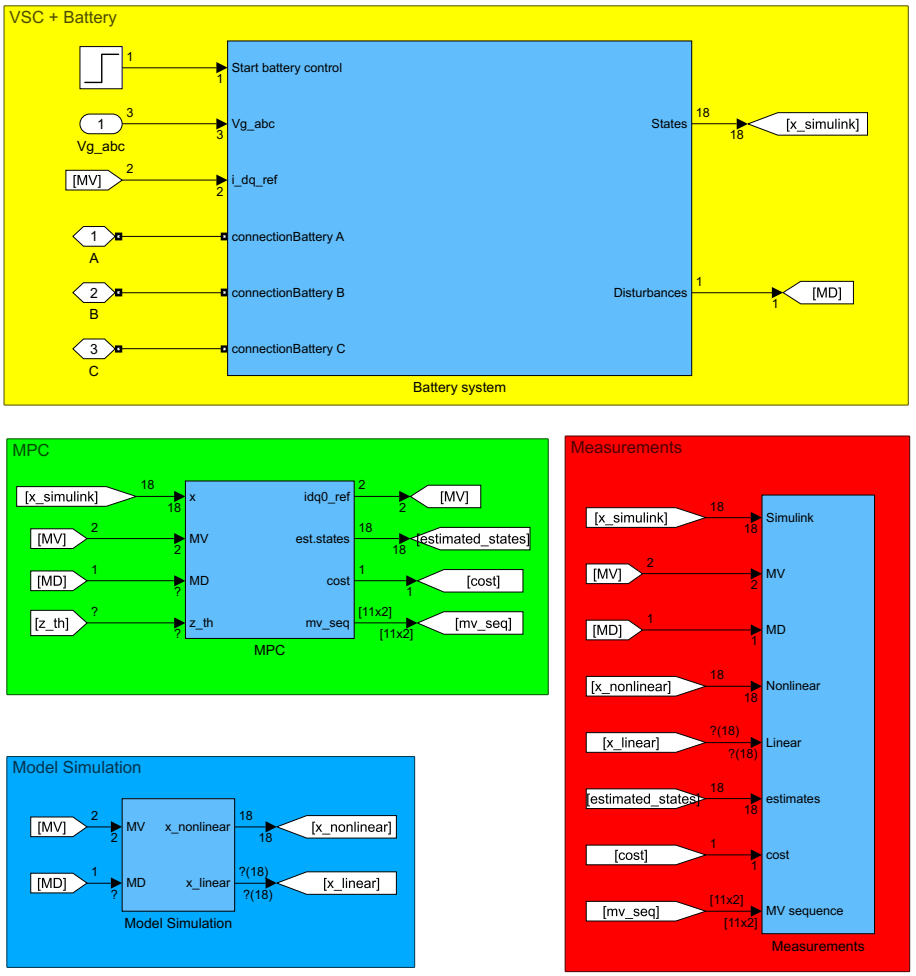

Figure A.1.3: Simulink model. BESS inputs and outputs.

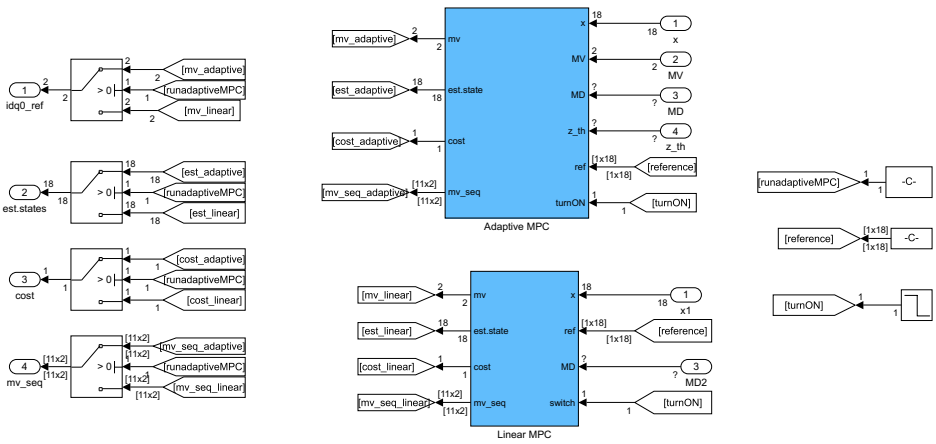

Figure A.1.4: Simulink model. MPC inputs and outputs

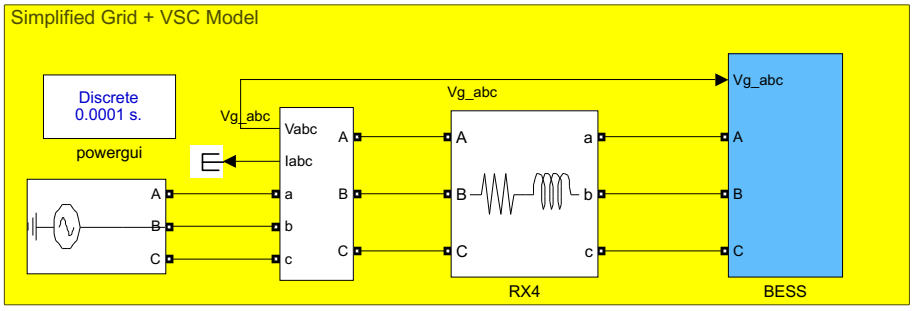

Figure A.1.5: Simulink model. Simplified grid model.

A.2 Nonlinear Differential Equations

Complete VSC model with all differential equations describing the dynamics of the grid-connected VSC.

$$\frac{d}{dt}v_{o,d} = \frac{\omega_b}{c_f}i_{cv,d} - \frac{\omega_b}{c_f}i_{o,d} + \omega_g\omega_b v_{o,q} \tag{A.2.1}$$

$$\frac{d}{dt}v_{o,q} = \frac{\omega_b}{c_f}i_{cv,q} - \frac{\omega_b}{c_f}i_{o,q} - \omega_g\omega_b v_{o,d} \tag{A.2.2}$$

$$\begin{aligned}\frac{d}{dt}i_{cv,d} = {} & \frac{\omega_b k_{p,c}}{l_f}i^*_{cv,d} - \frac{\omega_b k_{p,c}}{l_f}i_{cv,d} - \frac{\omega_b r_f}{l_f}i_{cv,d} + \frac{\omega_b k_{i,c}}{l_f}\gamma_d - \frac{\omega_b k_{ad}}{l_f}v_{o,d} \\ & + \frac{\omega_b k_{ad}}{l_f}\varphi_d - \omega_b k_{i,pll}\epsilon_{pll}i_{cv,q} - \omega_b k_{p,pll}\arctan\left(\frac{v_{pll,q}}{v_{pll,d}}\right)i_{cv,q}\end{aligned} \tag{A.2.3}$$

$$\frac{d}{dt}i_{cv,q} = \frac{\omega_b k_{p,c}}{l_f}i^*_{cv,q} - \frac{\omega_b k_{p,c}}{l_f}i_{cv,q} - \frac{\omega_b r_f}{l_f}i_{cv,q} + \frac{\omega_b k_{i,c}}{l_f}\gamma_q - \frac{\omega_b k_{ad}}{l_f}v_{o,q} \tag{A.2.4}$$

$$+\frac{\omega_b k_{ad}}{l_f}\varphi_q+\omega_b k_{i,pll}\epsilon_{pll}i_{cv,d}+\omega_b k_{p,pll}\arctan\left(\frac{v_{pll,q}}{v_{pll,d}}\right)i_{cv,d}$$

$$\frac{d}{dt}\gamma_d = i^*cv,d-i_{cv,d} \tag{A.2.5}$$

$$\frac{d}{dt}\gamma_q = i^*cv,q-i_{cv,q} \tag{A.2.6}$$

$$\frac{d}{dt}i_{o,d} = \frac{\omega_b}{l_g}v_{o,d}-\frac{\omega_b r_g}{l_g}i_{o,d}+\omega_g\omega_b i_{o,q}-\frac{\omega_b\cos(\delta\theta_{pll})}{l_g}\hat{v}_g \tag{A.2.7}$$

$$\frac{d}{dt}i_{o,q} = \frac{\omega_b}{l_g}v_{o,q}-\frac{\omega_b r_g}{l_g}i_{o,q}-\omega_g\omega_b i_{o,d}+\frac{\omega_b\sin(\delta\theta_{pll})}{l_g}\hat{v}_g \tag{A.2.8}$$

$$\frac{d}{dt}\varphi_d = \omega_{ad}v_{o,d}-\omega_{ad}\varphi_d \tag{A.2.9}$$

$$\frac{d}{dt}\varphi_q = \omega_{ad}v_{o,q}-\omega_{ad}\varphi_q \tag{A.2.10}$$

$$\frac{d}{dt}v_{pll,d} = \omega_{lp,pll}vo,d-\omega_{lp,pll}v_{pll,d} \tag{A.2.11}$$

$$\frac{d}{dt}v_{pll,q} = \omega_{lp,pll}v_{o,q}-\omega_{lp,pll}v_{pll,q} \tag{A.2.12}$$

$$\frac{d}{dt}\varepsilon_{pll} = \arctan\left(\frac{v_{pll,q}}{v_{pll,d}}\right) \tag{A.2.13}$$

$$\frac{d}{dt}\delta\theta_{pll} = \omega_b k_{p,pll}\arctan\left(\frac{v_{pll,q}}{v_{pll,d}}\right)+\omega_b k_{i,pll}\epsilon_{pll} \tag{A.2.14}$$

$$\frac{d}{dt}p_{o,f} = \omega_{lp,m}(p_o-p_{o,f}) \tag{A.2.15}$$

$$\frac{d}{dt}q_{o,f} = \omega_{lp,m}(q_o-q_{o,f}) \tag{A.2.16}$$

$$\frac{d}{dt}\hat{v}_{o,f} = \omega_{lp,m}(\hat{v}_o-\hat{v}_{o,f}) \tag{A.2.17}$$

$$\frac{d}{dt}\hat{i}_{cv,f} = \omega_{lp,m}(\hat{i}_cv-\hat{i}_{cv,f}) \tag{A.2.18}$$

A.3 System Matrices

The system matrices for the linear model derived from the nonlinear model in appendix A.2 are presented here. These system matrices are used in the linear and adaptive MPC implementation. Some values that can be assumed to be zero in steady state, such as $v_{pll,q}$ are also included for model accuracy during transient periods. These values are also included in the implemented linear model.

$$
A = \begin{bmatrix}
0 & \omega_b\omega_g & \frac{\omega_b}{c_f} & 0 & 0 & 0 & -\frac{\omega_b}{c_f} & 0 & 0 & 0 & 0 & 0 & 0 & 0 & 0 & 0 & 0 & 0 \\
-\omega_b\omega_g & 0 & 0 & \frac{\omega_b}{c_f} & 0 & 0 & 0 & -\frac{\omega_b}{c_f} & 0 & 0 & 0 & 0 & 0 & 0 & 0 & 0 & 0 & 0 \\
-\omega_b\frac{k_{ad}}{l_f} & 0 & -\omega_b\frac{k_{p,c}+r_f}{l_f} & -\omega_b k_{p,pll}\arctan\left(\frac{v_{pll,d}}{v_{pll,q}}\right) - \omega_b\epsilon_{pll}k_{i,pll} & \frac{\omega_b k_{i,c}}{l_f} & 0 & 0 & 0 & \frac{\omega_b k_{ad}}{l_f} & 0 & \omega_b k_{p,pll}\frac{i_{cv,q}v_{pll,q}}{v_{pll,d}^2+v_{pll,q}^2} & -\omega_b k_{p,pll}\frac{i_{cv,q}v_{pll,d}}{v_{pll,d}^2+v_{pll,q}^2} & -\omega_b k_{i,pll}i_{cv,q} & 0 & 0 & 0 & 0 & 0 \\
0 & -\frac{\omega_b k_{ad}}{l_f} & \omega_b k_{p,pll}\arctan\left(\frac{v_{pll,d}}{v_{pll,q}}\right) + \omega_b\epsilon_{pll}k_{i,pll} & \frac{\omega_b k_{i,c}}{l_f} & -\omega_b\frac{k_{p,c}+r_f}{l_f} & 0 & \omega_b\frac{k_{i,c}}{l_f} & 0 & 0 & \omega_b\frac{k_{ad}}{l_f} & -\omega_b k_{p,pll}\frac{i_{cv,q}v_{pll,q}}{v_{pll,d}^2+v_{pll,q}^2} & \omega_b k_{p,pll}\frac{i_{cv,q}v_{pll,d}}{v_{pll,d}^2+v_{pll,q}^2} & \omega_b k_{i,pll}i_{cv,d} & 0 & 0 & 0 & 0 & 0 \\
0 & 0 & -1 & 0 & 0 & 0 & 0 & 0 & 0 & 0 & 0 & 0 & 0 & 0 & 0 & 0 & 0 & 0 \\
0 & 0 & 0 & -1 & 0 & 0 & 0 & 0 & 0 & 0 & 0 & 0 & 0 & 0 & 0 & 0 & 0 & 0 \\
\frac{\omega_b}{l_g} & 0 & 0 & 0 & 0 & 0 & -\omega_b\frac{r_g}{l_g} & \omega_b\omega_{g,0} & 0 & 0 & 0 & 0 & 0 & \omega_b\frac{\sin\delta\theta_{pll,0}}{l_g}\hat{v}_{g,0} & 0 & 0 & 0 & 0 \\
0 & \frac{\omega_b}{l_g} & 0 & 0 & 0 & 0 & -\omega_b\omega_{g,0} & -\omega_b\frac{r_g}{l_g} & 0 & 0 & 0 & 0 & 0 & \omega_b\frac{\cos\delta\theta_{pll,0}}{l_g}\hat{v}_{g,0} & 0 & 0 & 0 & 0 \\
\omega_{ad} & 0 & 0 & 0 & 0 & 0 & 0 & 0 & -\omega_{ad} & 0 & 0 & 0 & 0 & 0 & 0 & 0 & 0 & 0 \\
0 & \omega_{ad} & 0 & 0 & 0 & 0 & 0 & 0 & 0 & -\omega_{ad} & 0 & 0 & 0 & 0 & 0 & 0 & 0 & 0 \\
\omega_{lp,pll} & 0 & 0 & 0 & 0 & 0 & 0 & 0 & 0 & 0 & -\omega_{lp,pll} & 0 & 0 & 0 & 0 & 0 & 0 & 0 \\
0 & \omega_{lp,pll} & 0 & 0 & 0 & 0 & 0 & 0 & 0 & 0 & 0 & -\omega_{lp,pll} & 0 & 0 & 0 & 0 & 0 & 0 \\
0 & 0 & 0 & 0 & 0 & 0 & 0 & 0 & 0 & 0 & -\frac{v_{pll,q}}{v_{pll,d}^2+v_{pll,q}^2} & \frac{v_{pll,d}}{v_{pll,d}^2+v_{pll,q}^2} & 0 & 0 & 0 & 0 & 0 & 0 \\
0 & 0 & 0 & 0 & 0 & 0 & 0 & 0 & 0 & 0 & -\omega_b k_{p,pll}\frac{v_{pll,q}}{v_{pll,d}^2+v_{pll,q}^2} & \omega_b k_{p,pll}\frac{v_{pll,d}}{v_{pll,d}^2+v_{pll,q}^2} & 0 & 0 & 0 & 0 & 0 & \\
\omega_{lp,m}i_{cv,d} & \omega_{lp,m}i_{cv,q} & \omega_{lp,m}v_{o,d} & \omega_{lp,m}v_{o,q} & 0 & 0 & 0 & 0 & 0 & 0 & 0 & 0 & 0 & 0 & -\omega_{lp,m} & 0 & 0 & 0 \\
-\omega_{lp,m}i_{cv,q} & \omega_{lp,m}i_{cv,d} & \omega_{lp,m}v_{o,q} & -\omega_{lp,m}v_{o,d} & 0 & 0 & 0 & 0 & 0 & 0 & 0 & 0 & 0 & 0 & 0 & -\omega_{lp,m} & 0 & 0 \\
\frac{\omega_{lp,m}v_{o,d}}{\sqrt{v_{o,d}^2+v_{o,q}^2}} & \frac{\omega_{lp,m}v_{o,q}}{\sqrt{v_{o,d}^2+v_{o,q}^2}} & 0 & 0 & 0 & 0 & 0 & 0 & 0 & 0 & 0 & 0 & 0 & 0 & 0 & 0 & -\omega_{lp,m} & 0 \\
0 & 0 & \frac{\omega_{lp,m}i_{cv,d}}{\sqrt{i_{cv,d}^2+i_{cv,q}^2}} & \frac{\omega_{lp,m}i_{cv,q}}{\sqrt{i_{cv,d}^2+i_{cv,q}^2}} & 0 & 0 & 0 & 0 & 0 & 0 & 0 & 0 & 0 & 0 & 0 & 0 & 0 & -\omega_{lp,m}
\end{bmatrix}
$$

$$
B = \begin{bmatrix}
0 & 0 & 0 & \omega_b v_{o,0}^q \\
0 & 0 & 0 & -\omega_b v_{o,0}^d \\
\omega_b \frac{k_{p,c}}{l_f} & 0 & 0 & 0 \\
0 & \omega_b \frac{k_{p,c}}{l_f} & 0 & 0 \\
1 & 0 & 0 & 0 \\
0 & 1 & 0 & 0 \\
0 & 0 & -\omega_b \frac{\cos \delta\theta_{pll,0}}{l_g} & \omega_b i_{o,0}^q \\
0 & 0 & \omega_b \frac{\sin \delta\theta_{pll,0}}{l_g} & \omega_b i_{o,0}^d \\
0 & 0 & 0 & 0 \\
0 & 0 & 0 & 0 \\
0 & 0 & 0 & 0 \\
0 & 0 & 0 & 0 \\
0 & 0 & 0 & 0 \\
0 & 0 & 0 & 0 \\
0 & 0 & 0 & 0 \\
0 & 0 & 0 & 0 \\
0 & 0 & 0 & 0 \\
0 & 0 & 0 & 0
\end{bmatrix}
$$

$$C = \begin{bmatrix}
1 & 0 & 0 & 0 & 0 & 0 & 0 & 0 & 0 & 0 & 0 & 0 & 0 & 0 & 0 & 0 & 0 & 0 \\
0 & 1 & 0 & 0 & 0 & 0 & 0 & 0 & 0 & 0 & 0 & 0 & 0 & 0 & 0 & 0 & 0 & 0 \\
0 & 0 & 1 & 0 & 0 & 0 & 0 & 0 & 0 & 0 & 0 & 0 & 0 & 0 & 0 & 0 & 0 & 0 \\
0 & 0 & 0 & 1 & 0 & 0 & 0 & 0 & 0 & 0 & 0 & 0 & 0 & 0 & 0 & 0 & 0 & 0 \\
0 & 0 & 0 & 0 & 1 & 0 & 0 & 0 & 0 & 0 & 0 & 0 & 0 & 0 & 0 & 0 & 0 & 0 \\
0 & 0 & 0 & 0 & 0 & 1 & 0 & 0 & 0 & 0 & 0 & 0 & 0 & 0 & 0 & 0 & 0 & 0 \\
0 & 0 & 0 & 0 & 0 & 0 & 1 & 0 & 0 & 0 & 0 & 0 & 0 & 0 & 0 & 0 & 0 & 0 \\
0 & 0 & 0 & 0 & 0 & 0 & 0 & 1 & 0 & 0 & 0 & 0 & 0 & 0 & 0 & 0 & 0 & 0 \\
0 & 0 & 0 & 0 & 0 & 0 & 0 & 0 & 1 & 0 & 0 & 0 & 0 & 0 & 0 & 0 & 0 & 0 \\
0 & 0 & 0 & 0 & 0 & 0 & 0 & 0 & 0 & 1 & 0 & 0 & 0 & 0 & 0 & 0 & 0 & 0 \\
0 & 0 & 0 & 0 & 0 & 0 & 0 & 0 & 0 & 0 & 1 & 0 & 0 & 0 & 0 & 0 & 0 & 0 \\
0 & 0 & 0 & 0 & 0 & 0 & 0 & 0 & 0 & 0 & 0 & 1 & 0 & 0 & 0 & 0 & 0 & 0 \\
0 & 0 & 0 & 0 & 0 & 0 & 0 & 0 & 0 & 0 & 0 & 0 & 1 & 0 & 0 & 0 & 0 & 0 \\
0 & 0 & 0 & 0 & 0 & 0 & 0 & 0 & 0 & 0 & 0 & 0 & 0 & 1 & 0 & 0 & 0 & 0 \\
0 & 0 & 0 & 0 & 0 & 0 & 0 & 0 & 0 & 0 & 0 & 0 & 0 & 0 & 1 & 0 & 0 & 0 \\
0 & 0 & 0 & 0 & 0 & 0 & 0 & 0 & 0 & 0 & 0 & 0 & 0 & 0 & 0 & 1 & 0 & 0 \\
0 & 0 & 0 & 0 & 0 & 0 & 0 & 0 & 0 & 0 & 0 & 0 & 0 & 0 & 0 & 0 & 1 & 0 \\
0 & 0 & 0 & 0 & 0 & 0 & 0 & 0 & 0 & 0 & 0 & 0 & 0 & 0 & 0 & 0 & 0 & 1
\end{bmatrix}$$

A.4 Simulation Parameters

The grid, VSC and battery parameters are listed in this section. Most parameters are kept equal throughout the simulation. The line impedances, constant node impedances and voltage source changes depend on the grid strength simulated. The parameters used in the grid are:

- VSC: Table A.4.1.
- Inner loop current controller: Table A.4.2.
- Transformer: Table A.4.3.
- Varying load at node 9: Table A.4.4.
- Voltage source, strong grid: Table A.4.5.
- Node impedances, strong grid: Table A.4.6.
- Line impedances, strong grid: Table A.4.7.
- Voltage source, weak grid: Table A.4.8
- Node impedances, weak grid: Table A.4.9.
- Line impedances, weak grid: Table A.4.10.
- Line impedances, resistive weak grid: Table A.4.11.

Parameter	Value	parameter	Value
P_{rated}	20kW	V_{batt}	784V
V_{rated}	400V	r_{batt}	0.005 pu
I_{rated}	28.9A		
f_{rated}	50		

Table A.4.1: Voltage source converter parameters.

Parameter	pu value	Parameter	pu value
l_f	0.08	kp_{pll}	0.0531
r_f	0.003	ki_{pll}	0.2947
c_f	0.074	$\omega_{lp,pll}$	50
kp_c	0.8488	k_{ad}	1
ki_c	10	ω_{ad}	50
		ω_b	100 π

Table A.4.2: Inner loop current controller parameters.

Parameter	pu value	parameter	pu value
t_{rated}	100kW	r_{prim}	0.005 pu
V_{prim}	22kV	x_{prim}	0.025 pu
f_{rated}	400v	r_{sec}	0.005 pu
t_{ratio}	55	x_{sec}	0.025 pu

Table A.4.3: Transformer parameters.

Time	Active power	Time	Reactive Power
0 s	0 kW	0 s	0 VAR
0.1 s	5 kW	0.1 s	150 VAR
1.1 s	0 kW	1.1 s	0 VAR
2.1 s	-5 kW	2.1 s	-150 VAR
3.1 s	0 kW	3.1 s	0 VAR

Table A.4.4: Load demand for changing load at node 9.

Strong Grid

Parameter	pu value
V_{rated}	22kV
P_{sc}	1 MW
X/R ratio	10
f_{rated}	50

Table A.4.5: Voltage source parameters in the strong grid.

Node	Active power	Node	Reactive Power
P_1	5 kW	Q_1	150 VAR
P_2	3 kW	Q_2	90 VAR
P_3	1 kW	Q_3	30 VAR
P_4	2 kW	Q_4	60 VAR
P_5	1 kW	Q_5	30 VAR
P_6	5 kW	Q_6	150 VAR
P_7	2 kW	Q_7	60 VAR
P_8	1 kW	Q_8	30 VAR
P_9	2 kW	Q_9	60 VAR

Table A.4.6: Nominal power of nodes in the strong grid. Impedance is calculated from $V_n = 400$ and power.

Parameter	pu value	Parameter	pu value
r_{1-2}	0.0001	x_{1-2}	0.0006
r_{2-3}	0.0085	x_{2-3}	0.0554
r_{3-4}	0.0011	x_{3-4}	0.0072
r_{4-5}	0.0006	x_{4-5}	0.0013
r_{5-6}	0.0014	x_{5-6}	0.0033
r_{6-7}	0.0016	x_{6-7}	0.0037
r_{7-8}	0.0013	x_{7-8}	0.0030
r_{8-9}	0.0018	x_{8-9}	0.0042

Table A.4.7: Line resistance and reactance in the strong grid.

Weak Grid

Parameter	pu value
V_{rated}	22kV
P_{sc}	100 kW
X/R ratio	5
f_{rated}	50

Table A.4.8: Voltage source parameters in the weak grid.

Node	Active power	Node	Reactive Power
P_1	1 kW	Q_1	30 VAR
P_2	2 kW	Q_2	60 VAR
P_3	1 kW	Q_3	30 VAR
P_4	0.5 kW	Q_4	15 VAR
P_5	2 kW	Q_5	60 VAR
P_6	0.5 kW	Q_6	15 VAR
P_7	1 kW	Q_7	30 VAR
P_8	2 kW	Q_8	60 VAR
P_9	1 kW	Q_9	30 VAR

Table A.4.9: Nominal power of nodes in the weak grid. Impedance is calculated from $V_n = 400$ and power.

Parameter	pu value	Parameter	pu value
r_{1-2}	0.0009	x_{1-2}	0.0001
r_{2-3}	0.0846	x_{2-3}	0.0111
r_{3-4}	0.0109	x_{3-4}	0.0014
r_{4-5}	0.0056	x_{4-5}	0.0003
r_{5-6}	0.0141	x_{5-6}	0.0007
r_{6-7}	0.0156	x_{6-7}	0.0007
r_{7-8}	0.0129	x_{7-8}	0.0006
r_{8-9}	0.0179	x_{8-9}	0.0008

Table A.4.10: Line resistance and reactance in the weak grid.

Parameter	pu value	Parameter	pu value
r_{1-2}	0.0018	x_{1-2}	0.0001
r_{2-3}	0.1692	x_{2-3}	0.0111
r_{3-4}	0.0219	x_{3-4}	0.0014
r_{4-5}	0.0111	x_{4-5}	0.0003
r_{5-6}	0.0281	x_{5-6}	0.0007
r_{6-7}	0.0312	x_{6-7}	0.0007
r_{7-8}	0.0257	x_{7-8}	0.0006
r_{8-9}	0.0357	x_{8-9}	0.0008

Table A.4.11: Line resistance and reactance in the resistive weak grid.

A.5 Clarke and Park Transformation Matrices

$$\begin{bmatrix} x_\alpha \\ x_\beta \end{bmatrix} = K \begin{bmatrix} \frac{2}{3} & -\frac{1}{3} & -\frac{1}{3} \\ 0 & \frac{1}{\sqrt{3}} & -\frac{1}{\sqrt{3}} \end{bmatrix} \begin{bmatrix} x_a \\ x_b \\ x_c \end{bmatrix} \tag{A.5.1}$$

$$\begin{bmatrix} x_a \\ x_b \\ x_c \end{bmatrix} = \frac{1}{K} \begin{bmatrix} 1 & 0 \\ -\frac{1}{2} & \frac{\sqrt{3}}{2} \\ -\frac{1}{2} & \frac{\sqrt{3}}{2} \end{bmatrix} \begin{bmatrix} x_\alpha \\ x_\beta \end{bmatrix} \tag{A.5.2}$$

$$\begin{bmatrix} x_d \\ x_q \end{bmatrix} = \begin{bmatrix} \cos\omega t & \sin\omega t \\ -\sin\omega t & \cos\omega t \end{bmatrix} \begin{bmatrix} x_\alpha \\ x_\beta \end{bmatrix} \tag{A.5.3}$$

$$\begin{bmatrix} x_\alpha \\ x_\beta \end{bmatrix} = \begin{bmatrix} \cos\omega t & -\sin\omega t \\ \sin\omega t & \cos\omega t \end{bmatrix} \begin{bmatrix} x_d \\ x_q \end{bmatrix} \tag{A.5.4}$$

A.6 Power Calculations

In a synchronous reference frame the apparent power $\boldsymbol{s}$ can be expressed as

$$\boldsymbol{s} = p + jq = \boldsymbol{v}\boldsymbol{i}^* = v_d i_d + v_q i_q + j(-v_d i_q + v_q i_d) \tag{A.6.1}$$

where it can be seen that the active p and reactive q power are

$$p = v_d i_d + v_q i_q \tag{A.6.2}$$

$$q = -v_d i_q + v_q i_d. \tag{A.6.3}$$

By aligning the dq-frame on the real axis, such that the voltage vector is real-valued

$$\boldsymbol{v} = v_d + j v_q = v_d \tag{A.6.4}$$

the active and reactive power becomes

$$p = v_d i_d \tag{A.6.5}$$

$$q = -v_d i_q. \tag{A.6.6}$$

B Terms

B.1 Explanation of Battery Terms

A brief explanation of battery terms discussed in the thesis:

- **SoC:** The current level of charge in a battery relative to the maximum energy capacity. It is typically expressed as a percentage.
- **SoH:** The maximum available energy capacity of the battery, which typically decreases during the lifetime of the battery due to degradation.
- **DoD:** The current level of discharge in a battery relative to the maximum energy capacity. It is typically expressed as a percentage.
- **C-rate:** The maximum charging/discharging current permitted compared to the nominal current.

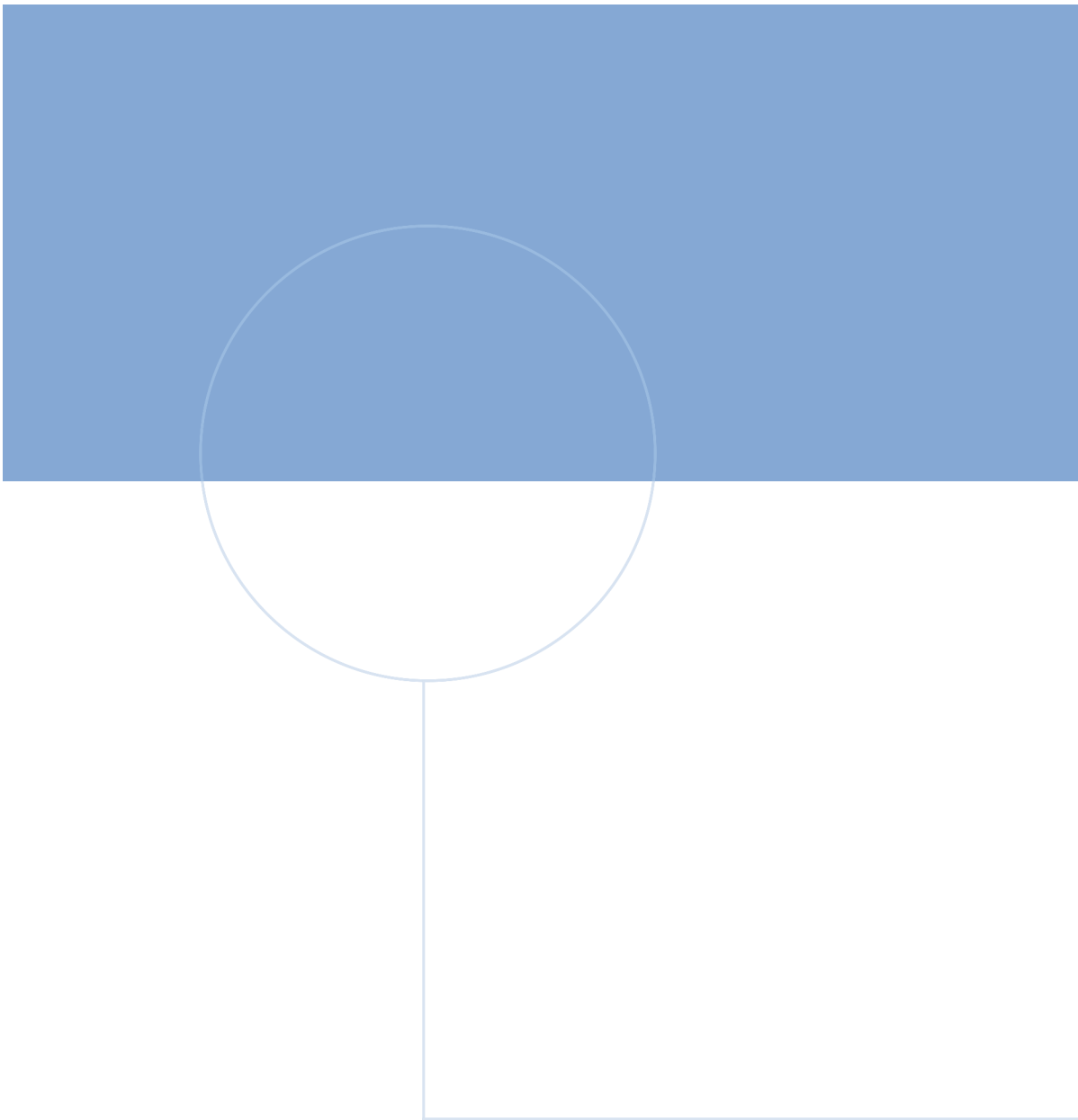

NTNU

Norwegian University of
Science and Technology